Controlling plasmon-enhanced luminescence

Ph.D. Thesis Utrecht University, April 2007
ISBN 978-90-77209-15-8

A digital version of this thesis can be downloaded from www.amolf.nl

Controlling plasmon-enhanced luminescence

Controle van door plasmonen verhoogde luminescentie

(met een samenvatting in het Nederlands)

Proefschrift

ter verkrijging van de graad van doctor aan de Universiteit Utrecht
op gezag van de rector magnificus, prof. dr. W. H. Gispen,
ingevolge het besluit van het college voor promoties
in het openbaar te verdedigen
op woensdag 25 april 2007 des middags te 12.45 uur

door

Hans Mertens

geboren op 25 januari 1978 te Weert

Promotor: Prof. Dr. A. Polman

The work described in this thesis was part of the research program of the 'Stichting voor Fundamenteel Onderzoek der Materie' (FOM), which is financially supported by the 'Nederlandse organisatie voor Wetenschappelijk Onderzoek' (NWO). This work was also supported by the NanoNed technology program of the Dutch Ministry of Economic affairs, and by the Multidisciplinary University Research Initiative (MURI, USA) on Plasmonics.

Contents

1 General introduction **11**
1.1 Plasmon-enhanced luminescence 12
1.2 Contents of this thesis 14

I Fabrication of Ag nanostructures **17**

2 Ag nanostructures made by electron-beam lithography **19**
2.1 Introduction 20
2.2 Fabrication 20
2.2.1 Substrate cleaning and spin coating 20
2.2.2 Electron-beam lithography and development 21
2.2.3 Metal evaporation and lift-off 22
2.3 Characterization by scanning electron microscopy 22
2.4 Conclusions 23

3 Infrared plasmons in two-dimensional Ag nanoparticle arrays in Si **25**
3.1 Introduction 26
3.2 Experimental 26
3.3 Results 28
3.4 Discussion 28
3.5 Conclusions 31

4 Depth-resolved nanostructure and refractive index of borosilicate glass doped with Ag nanocrystals **33**
4.1 Introduction 34
4.2 Experimental 34
4.3 Results 35
4.3.1 Ag depth profile 35
4.3.2 Ag^0 depth profile 36
4.3.3 Refractive index depth profile 38
4.3.4 Discussion 40

4.4 Conclusions 42

II Plasmon-enhanced Si quantum dot luminescence 43

5 Spectral tunability 45
5.1 Introduction 46
5.2 Experimental 46
5.3 Results 50
5.4 Conclusions 52

6 Polarization selectivity 53
6.1 Introduction 54
6.2 Experimental 55
6.3 Results 55
6.3.1 Extinction measurements 55
6.3.2 Photoluminescence measurements 57
6.4 Conclusions 61

7 Electroluminescence 63
7.1 Introduction 64
7.2 Experimental 64
7.2.1 Device structure 64
7.2.2 Optoelectronic characterization 65
7.3 Results and discussion 67
7.4 Conclusions 70

III Erbium ions coupled to Ag or Si nanostructures 71

8 Plasmon-enhanced erbium luminescence 73
8.1 Introduction 74
8.2 Sample fabrication 75
8.3 Optical characterization 76
8.3.1 Spectral characteristics 77
8.3.2 Polarization characteristics 79
8.4 Conclusions 80

9 Absence of the enhanced intra-4f transition cross section at 1.5 μm of Er^{3+} in Si-rich oxide 81
9.1 Introduction 82
9.2 Experimental 82
9.3 Results 83
9.4 Conclusions 87

IV Modeling of plasmon-enhanced luminescence 89

10 Exact electrodynamical theory versus an improved Gersten and Nitzan model 91
10.1 Introduction . . . 92
10.2 Methods . . . 93
10.3 Decay rate modifications versus emitter-sphere separation . . . 95
10.4 Quantum efficiency enhancement versus sphere diameter . . . 97
10.4.1 Optimum size for quantum efficiency enhancement . . . 97
10.4.2 Higher-order mode contributions to the emission enhancement . . . 101
10.5 Gersten and Nitzan model versus exact electrodynamical theory 104
10.5.1 Emission pattern . . . 105
10.5.2 Emission enhancement . . . 106
10.5.3 Spectral trends in emission enhancement . . . 110
10.5.4 Higher-order mode contributions to the emission enhancement . . . 111
10.6 Conclusions . . . 112
10.7 Appendix: Expressions for the decay rates of an atom in the presence of a sphere according to the exact electrodynamical theory . . . 114

11 Radiative decay rate enhancements in the vicinity of two-dimensional arrays of anisotropic metal nanoparticles 117
11.1 Introduction . . . 118
11.2 Method . . . 118
11.3 Results . . . 119
11.4 Discussion . . . 123
11.4.1 Optimal array geometry . . . 123
11.4.2 Comparison to experimental results . . . 124
11.4.3 Radiative decay rate enhancement near a tip . . . 125
11.5 Conclusions . . . 126

12 Spectral separation of radiative and dark plasmon modes in anisotropic metal nanoparticles 127
12.1 Introduction . . . 128
12.2 Method . . . 128
12.3 Results . . . 128
12.4 Conclusions . . . 133

References 135

Summary 143

Samenvatting **147**

Dankwoord/Acknowledgments **151**

Curriculum vitae **153**

List of publications **155**

Chapter 1

General introduction

Metal nanoparticles can be used to manipulate light at nanoscale dimensions [1–3]. The opportunities that metal nanoparticles provide are based on plasmons, i.e., collective oscillations of the conduction electrons [4]. These excitations are resonant in the optical regime, at frequencies that can be tuned by engineering the nanoparticle size and shape. The resonant behavior originates from the fact that the conduction electrons are confined within the nanoparticle. As a consequence of this confinement, an electromagnetically induced displacement of the conduction electrons sets up a surface polarization (see Fig. 1.1). Due to the associated restoring force, the conduction electrons are harmonically bound to the nanoparticle, and the oscillator strength of the conduction electrons is compressed into a relatively narrow spectral band, leaving the nanoparticles transparant in the far-infrared, but strongly polarizable at the plasmon resonance frequency[†].

On resonance, the strong polarizability of the nanoparticle effectively draws the energy supplied by an incident electromagnetic wave into the particle. This effect results in a field enhancement concentrated in a nanoscale volume. The energy that is captured by the plasmons is partly dissipated in the metal and partly reradiated. The relative strength of these two processes depends on the metal that is used and on the nanoparticle geometry. Silver (Ag) and gold (Au) are the metals with the smallest Ohmic losses at optical frequencies, and therefore they show the strongest resonant behavior. For Ag and Au nanoparticles with diameters of a few tens of nanometers, dissipation dominates the plasmon decay, whereas reradiation becomes important for larger sizes. By engineering the nanoparticle geometry (i.e., size as well as shape), it is thus possible to control how the captured electromagnetic energy is further

[†]Plasmons in metal nanoparticles are often referred to as *surface plasmons*, because of the essential influence of surface polarization on the resonant behavior [4]. In addition, plasmons in metal nanoparticles can be considered as *plasmon polaritons*, because of the intrinsic coupling with the electromagnetic field outside the nanoparticle [4].

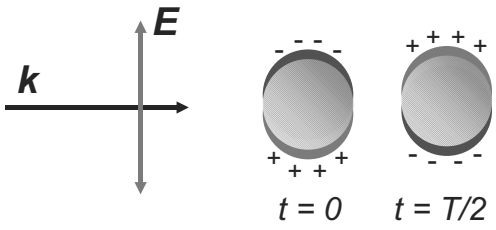

Figure 1.1: Excitation of a plasmon mode by an incoming plane wave with wave vector $\boldsymbol{k}$, electric field amplitude E, and frequency $f = 1/T$. The generated surface polarization gives rise to a restoring force that leads to a harmonic oscillation of the conduction electrons within the nanoparticle.

distributed.

The pronounced optical properties of metal nanoparticles give rise to a wide variety of applications. For example, strongly scattering nanoparticles have high potential as biomarkers for molecular imaging [5], and can be used to improve the extraction efficiency of light-emitting diodes [6]. Strongly absorbing nanoparticles enable controlled drug delivery and photothermal cancer treatment [7], as well as photothermal molecular imaging [8]. Besides, linear arrays of noble-metal nanoparticles can be used to transport electromagnetic energy over micrometer distances with a lateral confinement of a few tens of nanometers [9, 10]. Furthermore, the large field enhancements near metal nanoparticles can boost light-matter interactions, which is useful for e.g. single-molecule detection based on surface-enhanced Raman scattering (SERS) [11, 12]. A related phenomenon is the enhancement of the luminescence intensity of an optical emitter that is located in the vicinity of a metal nanoparticle. This process, which we refer to as plasmon-enhanced luminescence[‡], is the main subject of this thesis.

1.1 Plasmon-enhanced luminescence

Plasmons strongly influence the luminescence properties of optical emitters that are located at short distance from metal nanoparticles. Several mechanisms play a role in this effect. First, the excitation of plasmon modes by an incident electromagnetic wave can enhance the pump rate of a nearby emitter due to the local field enhancement. Second, the coupling of an emitter to plasmon modes affects both the radiative and nonradiative decay rates. This phenomenon is based on the principle that the strength with which an emitter couples with the

[‡]Other commonly used terms are *surface-enhanced fluorescence* [13] and *metal-enhanced fluorescence* [14].

electromagnetic field depends on the emitter's environment [15]. According to classical electrodynamical theory, the power P that an oscillating point dipole transfers to the electromagnetic field, which is a measure for the excited state decay rate of an emitter[§], can be described as [16, 17]:

$$P = \frac{\omega}{2}\mathrm{Im}\left(\boldsymbol{\mu} \cdot \mathbf{E}\right), \tag{1.1}$$

where $\boldsymbol{\mu}$ is the fixed dipole moment of the emitter, ω is the oscillation frequency, and $\mathbf{E}$ is the electric field generated by the source dipole evaluated at the position of the source dipole. This electric field can be modified by placing strongly polarizable objects in the vicinity of the emitter, for example a metal nanoparticle with a plasmon resonance frequency that matches the emission frequency, as is schematically depicted in Fig. 1.2. Equation 1.1 indicates that decay rate enhancements associated with the excitation of plasmons can be interpreted as a consequence of a plasmon-induced enhancement of the electric field generated by the dipole itself.

Analogous to the energy captured from an incident plane wave, also the energy that is transferred from the emitter to the plasmon modes of a nanoparticle is partly dissipated and partly coupled to radiation. The first process accounts for enhanced nonradiative decay, the latter for enhanced radiative decay. Since the balance between dissipation and coupling to radiation depends strongly on geometry, as explained above in the context of scattering and absorption, the geometrical tunability of the optical properties of metal nanoparticles plays a crucial role in the optimization of plasmon-enhanced luminescence.

Despite the fact that Ohmic losses are intrinsic to metals, the luminescence intensity of optical emitters can potentially be enhanced by several orders of magnitude by metal nanoparticles. As a consequence, plasmon-enhanced luminescence has been the subject of intense research over several decades. Pioneering work was done in conjunction with studies on SERS in the 1970s and 1980s [13]. These early investigations, which were focused on the interaction of emitters with rough metal surfaces, resulted in the observation of substantial photoluminescence enhancements [18]. In addition, models were developed that describe plasmon-enhanced luminescence based on classical electromagnetic theory [19–21]. During the last decade, there has been a strong revival in experimental efforts to control spontaneous emission dynamics by metal nanostructure geometries [22–27]. In particular the development of novel nanofabrication methods as well as near-field characterization techniques have enabled experiments on (sometimes individual) molecules interacting with well-defined metal nanostructures, often referred to as nano-antennas [28, 29]. These experiments have led to the observation of photoluminescence enhancement and

[§]Here we assume that the excited-state decay rate is not affected by e.g. electron-electron interactions or phonon-assisted processes, which would provide additional nonradiative decay channels.

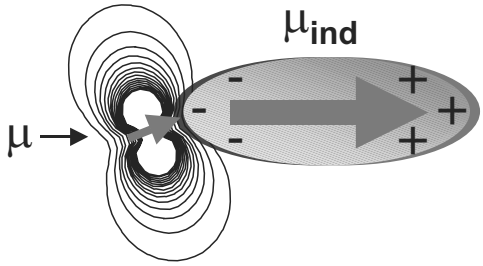

Figure 1.2: An emitter (left), represented as a point dipole with dipole moment $\boldsymbol{\mu}$, polarizes an anisotropic nanoparticle (right). At the plasmon resonance frequency, the induced dipole moment $\boldsymbol{\mu_{ind}}$ can be substantially larger than the source dipole moment $\boldsymbol{\mu}$.

quenching, depending on the distance between emitter and metal [22], with concomitant changes in excited state lifetime [23, 24].

1.2 Contents of this thesis

This thesis focuses on controlling plasmon-enhanced luminescence. We develop novel nanofabrication methods to integrate engineered metal nanostructures with solid-state light emitters in planar geometries that have a clear link with applications. In our experiments, we use silicon quantum dots and optically active erbium ions as model emitters that are fully compatible with standard CMOS fabrication technology. We demonstrate that the luminescence from these emitters can be significantly enhanced, and that the luminescence spectrum and polarization can be controlled by nanoparticle shape. In addition, we present detailed theoretical studies of the radiative and nonradiative decay rates of emitters near spherical and anisotropic metal nanoparticles. These calculations provide insight in the mechanism of plasmon-enhanced luminescence, and they indicate how nanoparticle geometries can be optimized to obtain the highest luminescence enhancements possible. Furthermore, we describe the integration of Ag nanoparticles in a prototype field-effect light-emitting device and demonstrate enhanced luminescence under electrical excitation.

Part I of this thesis describes three novel fabrication methods of Ag nanoparticles.

- Chapter 2 focuses on the fabrication of Ag nanoparticles with well-defined sizes and shapes on insulating substrates by electron-beam lithography. Structures made by the procedure described in this chapter, which exhibit plasmon resonances in the near-infrared, are used in the experiments on

plasmon-enhanced luminescence presented in part II and III.

- In Chapter 3 we report on the fabrication of two-dimensional arrays of Ag nanoparticles in Si by a sequential Si/Ag/Si electron-beam evaporation process. The Ag nanoparticles, which are formed during the evaporation process, exhibit plasmon resonances in the near-infrared, extending the applicability of plasmon-based applications into this technologically important spectral range.

- Chapter 4 describes the fabrication of Ag nanoparticles by a sequence of $Na^+ \leftrightarrow Ag^+$ ion exchange and ion irradiation of Na^+-containing glass. We consistently derive the Ag-nanocrystal depth profile and the corresponding refractive index depth profile by combining multiple characterization techniques. These nanoparticle geometries may also find applications in (non-linear) integrated optics.

Part II of this thesis is devoted to the experiments on plasmon-enhanced luminescence of silicon quantum dots (Si QDs) embedded in planar SiO_2 films.

- Chapter 5 describes how the photoluminescence intensity of Si QDs can be enhanced in a spectrally selective way by coupling to Ag nanoparticles. The luminescence enhancement, which ranges from a factor 2 to a factor 6, is directly correlated with the plasmon-related extinction properties of the nanoparticles.

- In Chapter 6 it is demonstrated that the photoluminescence intensity of Si QDs can be enhanced in a polarization-selective way by engineered elongated Ag nanoparticles. This behavior is directly correlated with the extinction properties of the nanoparticles.

- Chapter 7 reports on the integration of Ag nanoparticles and Ag films in field-effect light-emitting devices that were fabricated using processing facilities at Intel Inc. The Si QD electroluminescence intensity of these devices was enhanced by up to a factor 2.5. The data are related to nanoscale roughness of the metal film.

Part III is dedicated to the interaction of optically active erbium (Er^{3+}) ions with either Ag or Si nanoparticles.

- In Chapter 8 it is demonstrated that the photoluminescence intensity of optically active Er^{3+} ions positioned in close proximity of anisotropic Ag nanoparticles is significantly enhanced if the nanoparticles support plasmon modes that are resonant with the erbium emission at 1.5 μm. Opportunities for the reduction of quench processes in a wide range of erbium-doped materials are discussed.

- Chapter 9 focuses on the interaction of Er^{3+} ions with Si nanoparticles. The optical absorption cross section of the ${}^4I_{15/2} \rightarrow {}^4I_{13/2}$ transition at

1.5 μm of Er^{3+} ions embedded in SiO_2 and Si-rich oxide was measured using cavity ringdown spectroscopy. The experiment demonstrates that the silicon nanoparticles incorporated in Si-rich oxide do not enhance the peak cross section of the Er^{3+} $^4I_{15/2} - {}^4I_{13/2}$ transition by $1-2$ orders of magnitude, contrary to what has been reported in earlier work.

Part IV of this thesis describes theoretical studies of the influence of a metal nanoparticle on the radiative and nonradiative decay rates and on the luminescence quantum efficiency of an emitter positioned at short distance of the nanoparticle.

- Chapter 10 focuses on spherical nanoparticles. The influence of emitter-metal separation and nanoparticle size on the balance between radiative and nonradiative decay rate enhancements is analyzed based on exact electrodynamical theory. In addition, these results are compared to results obtained from an improved version of the Gersten and Nitzan model, which can be generalized to anisotropic nanoparticles more easily than exact electrodynamical theory.

- In Chapter 11 the improved Gersten and Nitzan model is applied to analyze how much the intensity emitted by a planar active layer of a light-emitting device can be enhanced by an array of anisotropic Ag nanoparticles. The calculated trends are compared to the experimental results described in Chapter 5.

- Chapter 12 describes the influence of particle anisotropy on the quantum efficiency of a low-quantum-efficiency emitter positioned at short distance of a metal nanoparticle. The analysis, which is based on the improved Gersten and Nitzan model, is focused on the spectral separation of radiative and dark plasmon modes in anisotropic metal nanoparticles.

Altogether, the thesis provides insight in the fundamental aspects of plasmon-enhanced luminescence, and correlates these to experiments on light emitters in practical geometries. Specific insights in possible applications are discussed in the corresponding chapters.

Part I

Fabrication of Ag nanostructures

Chapter 2

Ag nanostructures made by electron-beam lithography

Arrays of anisotropic Ag nanoparticles were fabricated on SiO_2 substrates by a combination of electron-beam lithography, Ag evaporation, and lift-off. Scanning electron microscopy was used to characterize the arrays. Since SiO_2 is a suitable host material for various optical emitters, including silicon quantum dots and erbium ions, the fabricated structures provide the opportunity to study the coupling between these dopants and the plasmon modes of Ag nanoparticles.

2.1 Introduction

Electron-beam lithography (EBL) is a powerful tool for the fabrication of metal nanostructures. The ultimate resolution is better than 10 nm [30, 31], and the technique is highly flexible. The flexibility originates from the fact that the electron-beam is scanned over the surface by a programmable pattern generator, so that the method does not rely on pre-fabricated masks.

In this chapter, we describe the fabrication of arrays of Ag nanoparticles on silica substrates by EBL. The size and shape of these nanoparticles is varied. In this way, the plasmon resonances can be tuned over a broad spectral range in the visible and near-infrared. In part II and III of this thesis we utilize this effect to study resonant coupling between optical emitters and plasmon modes.

2.2 Fabrication

The fabrication process consists of a number of steps that are described in the following subsections.

2.2.1 Substrate cleaning and spin coating

Substrates with a size of 10×10 mm^2 were sonicated in demineralized water for 5 minutes to remove small particles. These substrates were then cleaned in a 5:1:1 volume mixture of demineralized water, hydrogen peroxide (Merck, 30 wt.%), and ammonium hydroxide (Merck, 33 wt.%), at a temperature of 75 °C for 15 minutes. Hydrogen peroxide (H_2O_2) is a powerful oxidant, which removes organic residues. Ammonium hydroxide (NH_4OH) is a strong complexant for heavy metals. Cleaning in H_2O:NH_4OH:H_2O_2 comprises the first step of the RCA process, which is the standard sequence of chemistries to clean silicon wafers, as developed at the research laboratories of RCA (Radio Corporation of America) [32]. This process does not attack silicon. After thorough rinsing in demineralized water, the substrates were immersed in 2-propanol. The substrates were dried in a nitrogen gas flow just before spin-coating.

The clean substrates were spin-coated (Süss Microtec Delta 10) in a two-step process for reasons that become apparent in section 2.2.2. First, a solution of 4 wt.% 495k polymethylmethacrylate (PMMA) in chlorobenzene was spin-coated at 2000 rpm for 60 seconds, and baked at 175 °C for 30 minutes, in order to obtain a 100-nm-thick PMMA layer. Subsequently, a 4 wt.% 950k PMMA solution was spin-coated at 2500 rpm for 60 seconds, and baked at 175 °C for 30 minutes, resulting in a second 100-nm-thick PMMA layer. Note that 495k and 950k refer to the molecular weights of the respective PMMA polymers. A Ge layer with a thickness of $15 - 20$ nm was evaporated on top of the PMMA stack. This conductive layer prevents the occurrence of charging effects during electron-beam exposure.

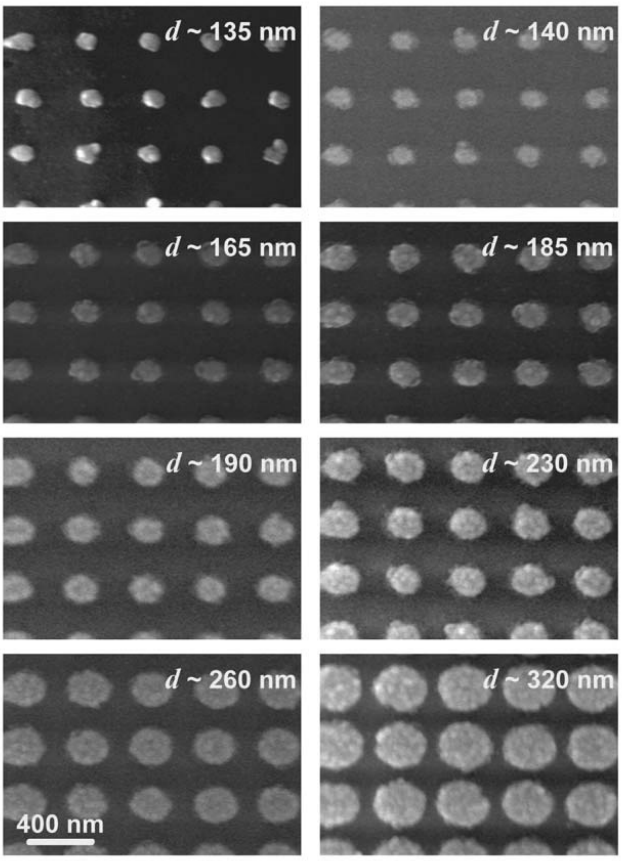

Figure 2.1: Scanning electron microscopy images of arrays of disk-shaped Ag nanoparticles with a diameter between 135 nm and 320 nm. The height of the nanoparticles is 20 nm. The array pitch is 400 nm.

2.2.2 Electron-beam lithography and development

The dual-layer PMMA stack was exposed to a 30-keV electron beam (Jeol JSM 6460) that was controlled by a pattern generator (Raith Elphy-Plus). The patterns consisted of arrays of dots that define the positions at which circular or elongated Ag nanoparticles will be formed later in the process; the dose per dot, which determines the Ag nanoparticle size, is between $0.01 - 0.5$ pC. The typical writing current is 60 pA. The sizes of the arrays were either 50×50 μm^2 or 100×100 μm^2.

After removing the Ge layer by reactive-ion etching (RIE) using an SF_6/O_2 plasma, the PMMA was developed in a 1:3 mixture of methylisobutylketone

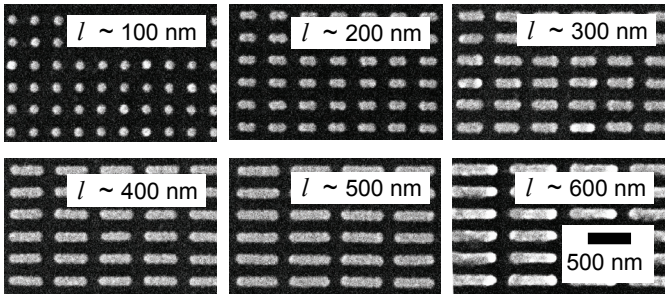

Figure 2.2: Scanning electron microscopy images of arrays of elongated Ag nanoparticles. The height of the nanoparticles is 20 nm.

(MIBK) and 2-propanol for 60 seconds. Due to the lower molecular weight of the bottom PMMA layer, an undercut profile is created.

2.2.3 Metal evaporation and lift-off

A 20-nm-thick Ag film was evaporated on top of the patterned PMMA by electron beam evaporation. The PMMA was then dissolved in acetone at 60 °C, leaving Ag on the substrate only where the PMMA was removed during the development process. The undercut profile in the mask prevents the Ag nanoparticles positioned on the substrate from being connected to the Ag layer on top of the PMMA stack. Since the adhesion of Ag to glass is limited, we used Si as an adhesion material in part of our experiments. In those cases, 2 nm of Si was evaporated before the Ag deposition without braking the vacuum in between.

2.3 Characterization by scanning electron microscopy

Figure 2.1 shows SEM images of arrays of Ag nanoparticles in the form of cylindrical disks. The array pitch and the nanoparticle height are fixed at 400 nm and 20 nm, respectively. The different disk diameters, ranging from 135 nm to 320 nm, correspond to different electron-beam irradiation fluences delivered to fixed positions (i.e., the centers of the disks). The Ag nanoparticles exhibit some geometrical irregularities, as can be seen best for the smallest particles (top left). The smallest particle size that was achieved is ∼80 nm. This minimum size could possibly be reduced by optimizing process parameters such as the PMMA stack thickness or by implementing advanced process steps

such as megasonic-assisted development [33].

Figure 2.2 shows SEM images of elongated Ag nanoparticles. These particles were made by electron-beam irradiation of a linear array of spots. In this way, particles with a height of 20 nm, a width of 100 nm, and a variable length of 100 to 600 nm were created.

2.4 Conclusions

Arrays of Ag nanoparticles have been fabricated on SiO_2 substrates. The realization of Ag nanoparticles on these transparent substrates provides the opportunity to study the resonant interaction between optical emitters embedded in SiO_2 and the plasmon modes of Ag nanoparticles with well-defined sizes and shapes. These experiments are described in part II and III of this thesis.

Chapter 3

Infrared plasmons in two-dimensional Ag nanoparticle arrays in Si

Two-dimensional arrays of Ag nanoparticles embedded in amorphous silicon were fabricated by a sequential Si/Ag/Si electron-beam evaporation process. The spontaneously formed nanoparticle arrays exhibit plasmon resonances in the near-infrared (0.9 eV) with tails extending below 0.5 eV. The data are compared with calculations that take into account measured particle size ($\sim$10 nm), particle aspect ratio ($\sim$1.5), and separation ($\sim$13 nm). It is concluded that the large redshift, relative to plasmon resonances in more common metallo-dielectric materials, is mainly due to the high refractive index of the amorphous-silicon matrix, with nanoparticle-shape anisotropy and interparticle coupling contributing several tenths of an electron volt. This work enables plasmon-related applications in the near-infrared, including the telecommunication wavelength of 1.5μm (0.8 eV).

3.1 Introduction

Metal nanoparticles have been the subject of extensive research for many years because of the large electromagnetic field enhancements associated with the excitation of collective conduction electron oscillations, so-called plasmons [4]. These electric field enhancements enable applications such as spontaneous emission enhancement [18] and single molecule detection based on surface-enhanced Raman scattering [11]. Furthermore, resonant energy transfer between closely spaced metal nanoparticles enables transport of electromagnetic energy below the diffraction limit [10].

Since all these applications rely on the resonant properties of plasmons, they are restricted to a limited frequency range, which is determined by the dielectric functions of the involved media, the size and shape of the particles, and the electromagnetic interaction between them [4]. For composites consisting of isolated spherical noble-metal nanoparticles embedded in glass, constituting some of the most extensively investigated metallo-dielectric materials, the plasmon resonances occur in the visible regime. In order to utilize plasmons that are resonant in the near-infrared, e.g. for telecommunication or sensing, a number of methods have been investigated to lower the resonance frequency: using high-index matrices such as GaAs [34] or TiO_2 [35], applying nanolithography to define anisotropically shaped nanoparticles [36], and aligning nanoparticles to induce electromagnetic interaction, by methods such as nanolithography [37] or ion irradiation [38].

In this chapter, we report on the experimental realization of two-dimensional Ag nanoparticle arrays embedded in amorphous silicon (a-Si), in which these three mechanisms (i.e., high-index matrix, anisotropically shaped nanoparticles, and interparticle coupling) are combined to shift the plasmon resonance well into the near-infrared, peaking at 0.9 eV (1.4 μm), with tails below 0.5 eV (2.5 μm).

3.2 Experimental

Two-dimensional Ag nanoparticle arrays embedded in a-Si were fabricated by sequential Si/Ag/Si electron-beam evaporation on both glass and NaCl substrates, resulting in samples as schematically sketched in Fig. 3.1(a). The Ag depositions were varied in duration in order to fabricate samples with evaporated Ag thicknesses of 0.6, 1.0 and 2.2 nm respectively, as was monitored *in-situ* using a crystal thickness monitor and verified afterwards by Rutherford backscattering spectrometry (RBS). The Ag evaporation rate was $\leq$0.05 nm/min. For all samples, the Ag nanoparticles, which were formed spontaneously during deposition, were positioned in the center of a 14-nm-thick a-Si layer by performing the Ag deposition in between two separate a-Si depositions. After each a-Si deposition, 300-eV-Kr-ion etching was applied to

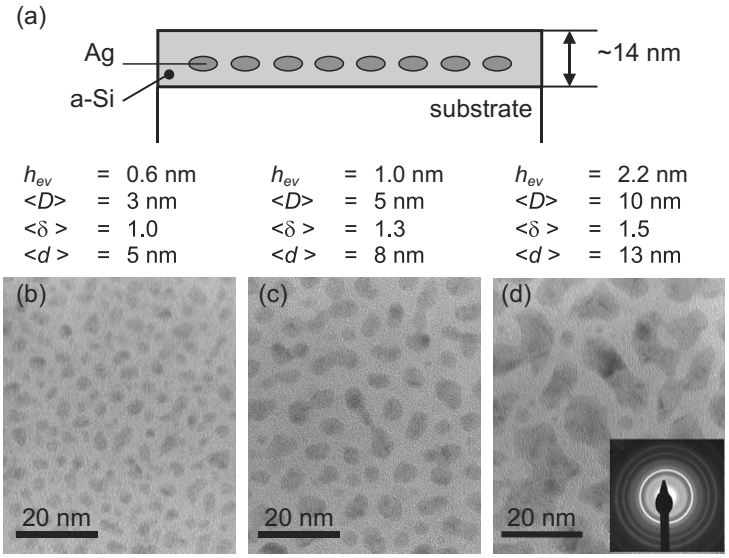

Figure 3.1: (a) Schematic representation of the sample geometry, and (b–d) plan-view bright-field TEM images of the Ag nanoparticle arrays embedded in a-Si prepared with (b) 0.6 nm, (c) 1.0 nm, and (d) 2.2 nm Ag, respectively. Evaporated Ag thickness h_{ev}, mean equivalent diameter $\langle D \rangle$, mean aspect ratio $\langle \delta \rangle$, and mean interparticle spacing $\langle d \rangle$ are indicated for each sample. The inset in (d) shows a SADP pattern, revealing the crystalline structure of the Ag nanoparticles.

reduce the surface roughness to ∼0.3 nm [39]. X-ray reflectrometry was used to monitor the a-Si thickness during both deposition and etching steps [40]. The substrates were kept at room temperature throughout the entire process.

The thin films deposited on NaCl were used to investigate the shape, size and separation of the Ag nanoparticles by plan-view transmission electron microscopy (TEM). For this purpose, the Si/Ag/Si films were separated from the NaCl in water and subsequently put on carbon-coated copper grids. A Philips CM30T and a Philips CM30UT-FEG electron microscope, operated at 300 keV, were used to take bright-field (BF) images, high-resolution (HREM) images and selected-area diffraction patterns (SADP). Elemental composition was investigated by energy-dispersive spectroscopy (EDS). Optical transmittance T and specular reflectance R were measured at (near-)normal incidence in the energy range $0.5 - 4$ eV with a Perkin-Elmer Lambda 900 spectrophotometer for the samples deposited on glass. Extinction E spectra were calculated from: $E = 1 - T - R$.

3.3 Results

Figures 3.1(b–d) show plan-view bright-field TEM images of the Ag-containing samples. Clearly distinguishable nanoparticles can be observed. EDS on a large particle confirmed the composition to be Ag. The TEM images reveal that increasing the evaporated Ag thickness leads to larger particle sizes. Quite irregular shapes can be observed for the large particles in Fig. 3.1(d). SADP patterns, one of which is displayed in the inset of Fig. 3.1(d), show rings indicating the presence of finely dispersed crystalline material (sharp rings) and amorphous material (broad rings). The sharp rings are found to correspond to crystalline Ag lattice spacings, while the broad rings are mainly attributed to a-Si. The crystalline structure of the Ag nanoparticles is confirmed in HREM images (not shown), in which multiple crystals can be recognized in each nanoparticle.

Characteristic parameters for the three sample topologies are listed in Figs. 3.1(b–d). The Ag areal density (in at/cm^2) was measured by RBS with an accuracy better than 5%. Subsequently, the evaporated Ag thickness h_{ev} was derived from the areal density and the bulk density for Ag. h_{ev} thus represents the mean Ag thickness, which does not depend on the nanoparticle distribution. The mean in-plane equivalent particle diameter $\langle D \rangle$ was obtained from TEM, where D is defined as the diameter of a circle with the same in-plane area as the particle under consideration. Combining h_{ev} with the areal particle density, the characteristic particle height h_{ob} was determined by assuming an oblate ellipsoidal shape. The mean particle aspect ratio $\langle \delta \rangle$ (major over minor diameter) increases from 1.0 (spherical particles) for the thinnest film to 1.5 for the thickest film. The mean center-to-center interparticle spacing $\langle d \rangle$ increases from 5 to 13 nm. These numbers indicate that significant particle coarsening occurred for the thicker films.

Figure 3.2(a) shows extinction spectra for all three Ag evaporated samples and a reference sample without Ag (all these samples were fabricated on glass). The reference sample shows a broad feature above 1.5 eV, due to the intrinsic band-to-band absorption in a-Si. The samples with Ag exhibit additional extinction, mainly at energies below 2.5 eV, which is attributed to the excitation of plasmons in the Ag nanoparticles. This contribution is more clearly shown in Fig. 3.2(b) in which absorption by a-Si has been corrected for. The plasmon-related extinction spectrum is shown to be rather broad ($\sim$1 eV full width at half-maximum), and increases in magnitude and shifts towards lower energies for increasing Ag content. The extinction peak energies are plotted versus evaporated Ag thickness in Fig. 3.3 (closed squares).

3.4 Discussion

In order to calculate the relative importance of the mechanisms contributing to the redshift of the plasmon resonance, we first evaluate the influence of the

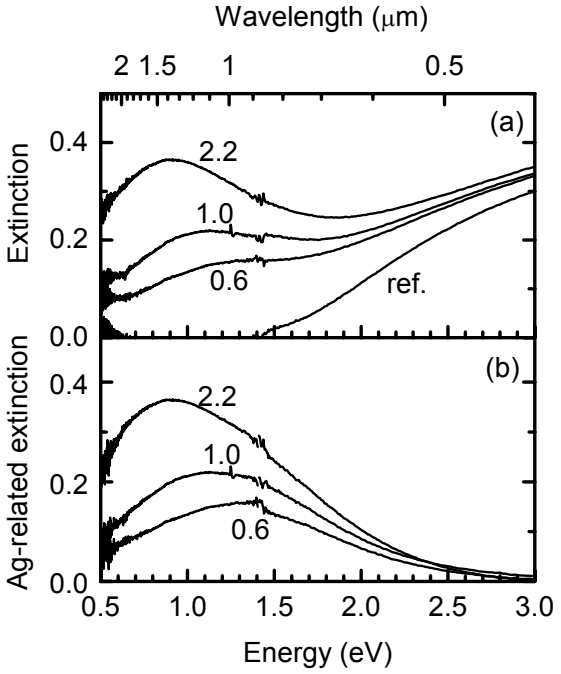

Figure 3.2: Extinction spectra of Ag nanoparticle arrays embedded in a-Si: (a) raw data, (b) Ag-related extinction. The evaporated Ag thicknesses are indicated in nm. The plasmon absorption peak increases in magnitude and shifts towards lower energies for increasing Ag content.

refractive index of the a-Si matrix and of shape anisotropy. The ensemble-averaged resonance frequency was obtained by averaging the calculated plasmon resonance frequencies of a large number of particles (103, 98, and 48, for the 0.6, 1.0, and 2.2 nm depositions, respectively) taking the TEM data (shape anisotropy and volume) as input. Each particle i was approximated as an oblate with minor axis h_{ob} and major axes D_i.

The plasmon resonance frequency $\omega_{0,i}$ of nanoparticle i, found by evaluating the resonance condition of its polarizability in the quasi-static limit [4], is described by:

$$\omega_{0,i} = \omega_p \sqrt{\frac{L_i}{\epsilon_m - L_i(\epsilon_m - \epsilon_\infty)}}, \tag{3.1}$$

with $\epsilon_m = n_m^2$ the dielectric constant of the embedding medium, L_i a geometrical factor determined by the aspect ratio δ_i [41], and ϵ_∞ and ω_p parameters of a modified Drude model for the real part of the dielectric function of Ag:

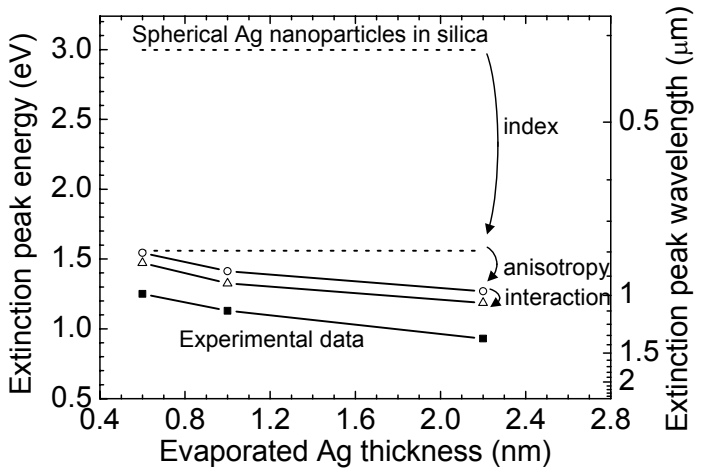

Figure 3.3: Calculated (open circles and triangles) and experimental (closed squares) absorptance peak energies for Ag nanoparticle arrays in a-Si. The resonance energy for spherical Ag nanoparticles in silica glass is indicated for reference. The three mechanisms contributing to the redshift are indicated.

$\epsilon'(\omega) = \epsilon_\infty - (\omega_p/\omega)^2$, determined by fitting the model to experimental data for Ag [42]. The refractive index of the a-Si matrix n_m was determined from transmittance and reflectance measurements of the reference sample without Ag and found to be 3.7 in the spectral range under consideration. For nanoparticles embedded in the center of a 14-nm-thick a-Si layer, it is appropriate to use this bulk value for the refractive index of the matrix [43]. The average extinction peak frequency ω_{peak} was calculated by summing over the particle ensemble taking into account the oscillator strength for each particle using its volume as a normalization factor.

The open circles in Fig. 3.3 show the calculated absorptance peak energies ($\hbar\omega_{peak}$) for the three nanoparticle ensembles embedded in a-Si. Data for the plasmon resonance energy of Ag nanoparticles in silica glass (index 1.46) are shown for reference. Clearly, the largest contribution to the calculated redshift is due to the high refractive index of the a-Si matrix compared to silica. The anisotropy for the 1.0 and 2.2 nm films adds another $0.2-0.3$ eV to the redshift.

To model the influence of interparticle coupling, the nanoparticles were considered as ideal dipoles that are coupled by near-field interaction, analogous to Ref. [44]. Under the assumption that the dipoles are oscillating in phase

(far-field excitation), the resonance frequency of nanoparticle i is given by:

$$\omega_i = \sqrt{\omega_{0,i}^2 - \frac{\omega_p^2}{4\pi\epsilon_m} \sum_{j \neq i} \frac{V_j(3\cos\theta_{i,j} - 1)}{d_{i,j}^3}}, \tag{3.2}$$

where $\omega_{0,i}$ is the resonance frequency if there would be no interaction, as described by Eq. 3.1, and $\theta_{i,j}$ the angle between the orientation of the dipoles (i.e. incident polarization) and the interparticle axis. In this summation we have taken the particle coordinates derived from TEM as input parameters (evaluating the same particles as in the analysis above). Only particles j, with volume V_j at distance $d_{i,j}$ from particle i, with $d_{i,j} < 30$ nm were taken into account, as coupling is negligible for larger distances. By averaging over the particle ensembles, the absorptance peak energies ($\hbar\omega_{peak}$) are derived as plotted in Fig. 3.3 (open triangles). As can be seen, interparticle coupling adds a relatively small redshift of $\sim$0.1 eV.

Comparing the experimental data to the calculation, a discrepancy of $\sim$0.2 eV is observed for all samples. This may be due to the approximations of oblate-shaped particles and resonantly interacting ideal dipoles in our model. Finite-difference time-domain calculations of the relaxation of excited nanoparticle ensembles could be used to avoid these approximations. Note that the calculated decreasing trend with increasing thickness is in good agreement with the experimental result.

The bandwidth of the measured extinction peak ($\sim$1 eV) is significantly larger than the homogeneous linewidth of plasmon resonances in Ag nanoparticles ($0.2 - 0.3$ eV) [4]. The large spectral width is attributed to variations in particle shape and orientation.

3.5 Conclusions

We have shown that a sequential Si/Ag/Si electron-beam evaporation process enables the fabrication of two-dimensional Ag nanoparticle arrays that exhibit plasmon resonances in the near-infrared. A model has been applied to analyze the redshift of the plasmon-induced extinction band, with experimentally determined geometric parameters as input. Taking into account the refractive index of the matrix, shape anisotropy and interparticle coupling, the experimental data are quite well described. It is concluded that the main origin of the redshift ($\sim$1.5 eV), compared to the plasmon resonance frequency of spherical Ag nanoparticles in silica, is the high refractive index of the a-Si matrix; shape anisotropy ($\langle d \rangle$ up to 1.5) contributes another $0.2 - 0.3$ eV, while the influence of coupling effects is limited to $\sim$0.1 eV. The data indicate that an increased Ag deposition thickness leads to larger shape anisotropy and thus a larger plasmon redshift.

The achievement of infrared plasmons in silicon enables applications such as plasmon-enhanced luminescence in the infrared, as is shown in Chapter 8, where Ag nanoparticles are defined by electron-beam lithography. As will be shown in Chapter 10, the optimum metal nanoparticle size to achieve plasmon-enhanced luminescence is in the range $30-100$ nm. Increasing the size of these spontaneously formed Ag nanoparticles, e.g. by changing the Ag deposition conditions or by thermal annealing, would therefore be required for the purpose of luminescence enhancement. Arrays of Ag nanoparticles fabricated in a similar way as presented here have been successfully applied for improving the outcoupling efficiency of light emitting diodes [6].

Chapter 4

Depth-resolved nanostructure and refractive index of borosilicate glass doped with Ag nanocrystals

We present an investigation of the Ag-nanocrystal depth profile as well as the corresponding refractive index depth profile of borosilicate glass that was first doped with Ag by $Na^+ \leftrightarrow Ag^+$ ion exchange and subsequently irradiated with 1-MeV Xe ions. By combining RBS, XPS, XE-AES, and transmission and reflection spectroscopy, we show unambiguously that the Ag nanocrystals are formed in a layer with a thickness (90 ± 20 nm) that is significantly smaller than the range (340 nm) of the 1-MeV Xe ions used to induce Ag nucleation. The effective refractive index for the highest Xe fluence is $n = 2.1 + i0.8$ at the resonance wavelength ($\lambda = 430$ nm). The implications for the integration of plasmon-based functionalities in photonic devices based on the described fabrication method are discussed.

4.1 Introduction

Composite materials consisting of nobel-metal nanoparticles embedded in a dielectric are known to exhibit surface plasmon resonances (SPR) at optical frequencies [4]. The local electromagnetic field enhancements associated with these resonances enable a broad range of applications including optical switches [45], optical filters [46], bistable devices [47], selective solar absorbers [48], and broadband waveguide polarizers [49].

During the last decades, many experimental methods have been introduced to fabricate metal-dielectric composites (often referred to as nanocermets). These methods include ion implantation [50], sol-gel processing [51], and sputtering or co-deposition techniques [52]. Also a sequence of $Na^+ \leftrightarrow Ag^+$ ion exchange and ion irradiation of Na^+-containing glass has been proposed [53]. This two-step process enables the fabrication of planar optical waveguides in which Ag nanocrystals are formed in lithographically defined sections, since mask-assisted ion irradiation can be applied to locally nucleate Ag nanocrystals [54]. Consequently, this approach provides the possibility of integrating SPR-based functionalities in photonic devices. As an example, Figure 4.1 shows a schematic of a planar waveguide in which nanocrystal-doped regions are formed in order to fabricate a nonlinear Bragg grating. Two-dimensional nonlinear photonic crystals have also been proposed [54]. Crucial for these applications is the local control of nanocrystal formation by ion irradiation.

In order to form well-defined Ag-nanoparticle sections with controlled optical properties, a detailed knowledge of the ion-beam-induced changes of material properties is of crucial importance. Within this context, we present an investigation of the Ag-nanocrystal depth profile as well as the corresponding refractive index depth profile of $Na^+ \leftrightarrow Ag^+$ ion-exchanged and subsequently Xe-irradiated borosilicate glass. The analysis is based on Rutherford backscattering spectrometry (RBS), X-ray photoelectron spectroscopy (XPS), X-ray-excited Auger spectroscopy (XE-AES), and optical transmittance and reflectance measurements. We conclude that the Ag nanocrystals are formed in a layer with a thickness that is significantly smaller than the range of the ions used to induce the nucleation, and we derive the optical constants for the Ag-nanocrystal-doped layer.

4.2 Experimental

Ag nanocrystals were formed in Na^+-containing Schott BK7 glass by a combination of $Na^+ \leftrightarrow Ag^+$ ion exchange and 1-MeV-Xe irradiation. The composition of the BK7 glass before ion exchange was 23 at.% Si, 61 at.% O, 5 at.% B, 7 at.% Na, 3 at.% K, 0.2 at.% Ba, as was determined by Rutherford backscattering spectrometry (RBS). Samples of 1 mm thickness were ion-exchanged at 350 °C for 10 minutes in a salt melt of 5 mol% $AgNO_3$ in $NaNO_3$. Sub-

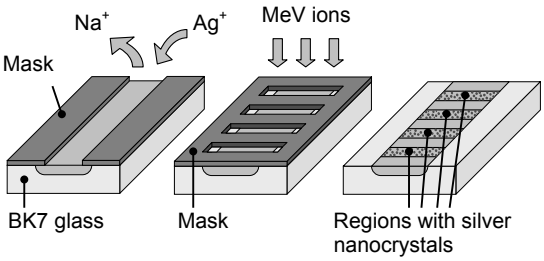

Figure 4.1: Schematic illustration of the fabrication process of a planar waveguide with Ag-nanocrystal-doped regions: (a) waveguide definition by a standard $Na^+ \leftrightarrow Ag^+$ ion-exchange process, (b) Ag-nanocrystal formation by ion irradiation using a mask-assisted process, and (c) the resulting metallodielectric Bragg grating.

sequently, Ag nanocrystals were formed by 1-MeV-Xe irradiation (ion range: 340 nm) under normal incidence at 77 K. Three samples were exposed to different fluences: 5.5×10^{14}, 3.0×10^{15}, and 1.0×10^{16} ions/cm^2, respectively. Transmission electron microscopy (TEM) has shown that this leads to the formation of Ag nanoparticles with diameters ranging from below 3.5 nm to $10 - 15$ nm [55].

RBS was performed using a 2-MeV-He beam to determine the Ag depth profile of the $Na^+ \leftrightarrow Ag^+$ ion-exchanged borosilicate glass before and after Xe irradiation. In addition, X-ray photoelectron spectroscopy (XPS) and X-ray excited Auger spectroscopy (XE-AES) were performed to identify the Ag chemical state as function of depth (range $10 - 450$ nm) [56, 57]. These measurements were done with a PHI Quantera scanning X-ray microprobe, using 1 keV Ar sputtering for depth profiling (depth accuracy: 10%). Optical transmittance and specular reflectance were measured at (near-)normal incidence in the spectral range of $1.2 - 4$ eV ($1000 - 300$ nm). Simulations, based on the transfer matrix method and the Maxwell-Garnett effective medium theory, were performed to obtain information on the depth-dependent optical constants.

4.3 Results

4.3.1 Ag depth profile

Figure 4.2 shows the Ag depth profile of unirradiated and 1-MeV-Xe irradiated $Na^+ \leftrightarrow Ag^+$ ion-exchanged borosilicate glass as obtained by RBS. Both Ag^0 and Ag^+ are represented in Fig. 4.2, as RBS is insensitive to the Ag chemical state. The unirradiated sample, having an Ag concentration of 7 at.% at the

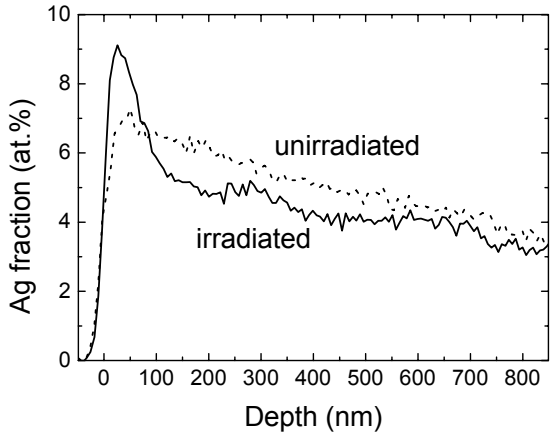

Figure 4.2: Ag depth profile, obtained by RBS, of unirradiated (dashed line) and 1-MeV-Xe-irradiated (solid line) Na+ $\leftrightarrow$ Ag^+ ion-exchanged borosilicate glass. The Xe fluence for the irradiated sample is 1.0×10^{16} ions/cm^2.

surface, shows a gradual decrease in Ag concentration as a function of depth, which is typical for the ion exchange process. The depth profile of the 1-MeV-Xe irradiated sample (fluence: $1.0{\times}10^{16}$ ions/cm^2) shows Ag accumulation in a layer of ∼80 nm directly below the surface (Ag peak concentration 9 at.%) and Ag depletion underneath that layer extending to a depth of >800 nm. The depth profiles of the samples irradiated at the other fluences exhibit a similar trend (not shown).

Ag accumulation in a layer directly below the surface and Ag depletion beneath that layer has also been observed in Ag-containing borosilicate glass that was thermally annealed in hydrogen [58]. This effect has been attributed to Ag reduction in the surface region and subsequent Ag^+ migration towards the surface due to the reduction-induced change in the Ag^+ electrochemical potential [59]. Accordingly, the Ag depth profiles shown in Fig. 4.2 would indicate that Ag nanoparticles (Ag^0) are mainly present in the first ∼80 nm below the surface.

4.3.2 Ag^0 depth profile

Figure 4.3 shows the XE-AES spectra of (a) unirradiated and (b) 1-MeV-Xe-irradiated (fluence: 1.0×10^{16} ions/cm^2) $Na^+ \leftrightarrow Ag^+$ ion-exchanged borosilicate glass at depths between 10 and 200 nm. The energy range is such that the Ag $M_4N_{45}N_{45}$ (358 eV) and $M_5N_{45}N_{45}$ (352 eV) Auger lines are visible;

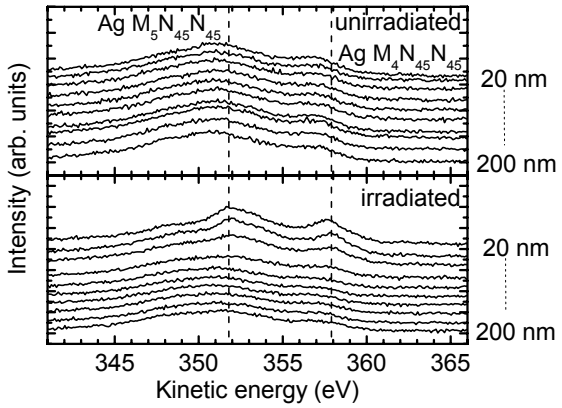

Figure 4.3: XE-AES spectra of the Ag $M_4N_{45}N_{45}$ and $M_5N_{45}N_{45}$ Auger lines of (a) unirradiated and (b) 1-MeV-Xe-irradiated (fluence: 1.0×10^{16} ions/cm^2) $Na^+ \leftrightarrow Ag^+$ ion-exchanged borosilicate glass over a depth range of $20 - 200$ nm (with a 20-nm step size). The spectra are shifted vertically for clarity. The dashed vertical lines indicate the peak positions for the Ag^0 chemical state.

both are sensitive to the Ag chemical state. The spectra obtained from the unirradiated sample all look similar, and the peak positions are fairly constant over depth. In contrast, the spectra obtained from the irradiated sample show a clear shift in Ag $M_4N_{45}N_{45}$ and $M_5N_{45}N_{45}$ Auger lines for the first $60-100$ nm. In fact, the corresponding peak positions are found to coincide with the peak energies for Ag^0 measured on a pure-Ag reference sample, which are indicated as dashed vertical lines in Fig. 4.3. Hence, XE-AES proves that only in a surface layer with a thickness of $60 - 100$ nm Ag nanoparticles (Ag^0) are present in significant quantities.

To make this result more specific, Figure 4.4 shows the depth-dependent Ag modified Auger parameter α', compiled by summation of the Ag $M_4N_{45}N_{45}$ Auger kinetic energy and the Ag $3d_{5/2}$ binding energy, using XE-AES and XPS spectra taken at 60 different depths in the range of $20-200$ nm. As static charge corrections cancel in α', it is a more accurate measure for chemical state identification than XE-AES by itself. Reference values of α' for Ag^0 and Ag_2O are indicated by the dashed lines [56]. The gradual change in α' with depth is schematically indicated by the gray band. Figure 4.4 shows unambiguously that Ag nanoparticles (Ag^0) are only present in the first 90 ± 20 nm. Additionally, it can be seen that the α' values for the unirradiated sample, as well as for the irradiated sample at larger depths, differ from the Ag_2O literature value, reflecting that the Ag chemical state in $Na^+ \leftrightarrow Ag^+$ ion-exchanged borosilicate glass is different from that of Ag in Ag_2O.

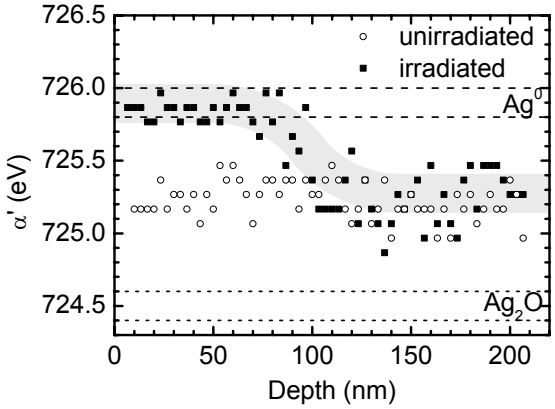

Figure 4.4: Modified Auger parameter α' for Ag as function of depth, obtained by XPS and XE-AES, over a depth range of 20−200 nm (with a 3-nm step size), for unirradiated (■) and 1-MeV-Xe-irradiated (◯) $Na^+ \leftrightarrow Ag^+$ ion-exchanged borosilicate glass. The Xe fluence for the irradiated sample is 1.0×10^{16} ions/cm^2. The gray band is a guide to the eye representing the trend for the irradiated sample. The α' literature values for Ag^0 and Ag_2O are indicated for reference.

4.3.3 Refractive index depth profile

Figure 4.5 shows optical transmittance (T) and reflectance (R) spectra for samples irradiated with Xe ions at fluences of (a) 1.0×10^{16}, (b) 3.0×10^{15}, and (c) 5.5×10^{14} ions/cm^2. The transmittance spectra were taken at normal incidence and are corrected for absorption by irradiation-induced defects, by performing a smooth background subtraction [55]. The reflectance spectra were taken at near-normal incidence on the ion-exchanged and ion-irradiated side. All samples show a dip in transmittance at ∼2.9 eV (430 nm), corresponding to the surface plasmon resonance energy of spherical Ag nanoparticles embedded in BK7 glass. This dip, which increases in magnitude with ion fluence, is accompanied with a peak in reflectance, being rather broad for the highest ion fluence.

In order to correlate the measured transmittance and reflectance spectra on one hand and the Ag^0 depth profile on the other hand, the spectral transmittance and reflectance were modeled. The calculations are based on the Maxwell-Garnett effective medium theory [41] to convert the Ag^0 depth profile to a refractive index profile, and on the transfer matrix method to subsequently calculate the spectral transmittance and reflectance. In the latter method, the gradually changing refractive index profile was discretized as a series of 1-nm-thick slabs. For every slab, the refractive index was derived from the material

composition through the Maxwell-Garnett effective medium theory, which implicitly assumes spherical inclusions (Ag^0 in this case) embedded in a matrix (BK7 glass in this case). The Ag dielectric function was described using literature values [42] whereas the refractive index of the glass was taken to be 1.5. The Ag^0 filling fraction, regarded as being constant for every slab, was considered as the main parameter for determining the complex effective refractive index. The Ag-nanoparticle size was taken into account in the Ag^0 dielectric function through the limited-mean-free-path model for the conduction electrons [4]. The particle size was assumed to be constant with depth for every sample. The depth profile of the Ag^0 volume fraction was described using a complementary error function with three free parameters: surface concentration, characteristic profile thickness, and characteristic profile curvature. The choice for this type of function is motivated by the shape of the Ag^0 depth profile determined from XPS and XE-AES, as shown in Fig. 4.4.

The simulated transmittance and reflectance spectra, shown as dashed lines in Fig. 4.5, resemble the measured data quite well. Most features are reproduced, including the low-energy shoulder of the reflection peak for the highest ion fluence (see Fig. 4.5(a)), which is attributed to interference within the nanocrystal-doped layer. The Ag^0 depth profiles used to obtain these spectra are shown in Fig. 4.6. The fitted particle diameters are 1.2, 4, and 4 nm for Xe implantation fluences of 5.5×10^{14}, 3.0×10^{15}, and 1.0×10^{16} ions/cm^2, respectively. Given the broad distributions of nanoparticle sizes in each sample, these numbers reflect characteristic values for each sample. The profile for 1.0×10^{16} ions/cm^2 is found to have a maximum Ag^0 content of 9 vol.%. Since the near-surface Ag concentration, as determined by RBS, amounts 10 vol.% (9 at.%), this implies that nearly all Ag is present as nanoparticles (Ag^0). The high simulated Ag^0 surface content is required to account for the relatively strong peak in reflectance, whereas the depth-integrated Ag^0 concentration is largely related to the strength of the transmittance dip. Small deviations between the experimental data and the simulated spectra in Fig. 4.5 may be due to the fact that the particle diameter varies with depth. According to the Maxwell-Garnett effective medium theory, an Ag-nanocrystal concentration of 9 vol.% corresponds to an effective refractive index of $n = 2.1 + i0.8$ at the resonance wavelength ($l = 430$ nm).

The Ag-nanoparticle depth profile derived from the simulation of the measured transmittance and reflectance spectra for the Xe fluence of 1.0×10^{16} ions/cm^2 is in very good agreement with the depth profile derived from the XPS and XE-AES measurements. This confirms that Ag nucleation mainly occurred in a relatively thin layer below the surface ($\sim$80 nm). For the two lower fluences, the simulated Ag^0 content at the surface is lower in order to fit the less pronounced peaks in reflectance, while the total amount of Ag^0 must be lower to account for the smaller dips in transmittance. These constraints lead to the depth profiles shown in Fig. 4.6 (dashed and dotted lines), with the resulting transmittance and reflectance spectra shown in Figs. 4.5(b) and (c).

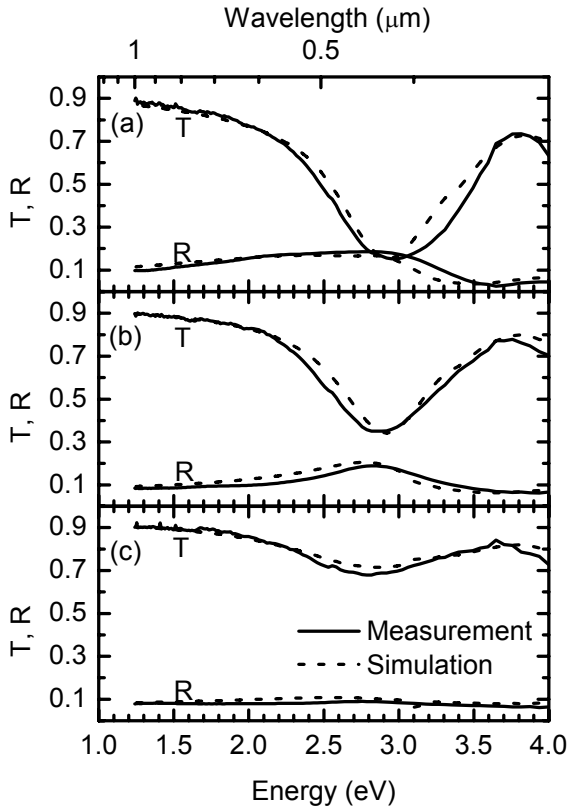

Figure 4.5: Optical transmittance (T) and reflectance (R) spectra of 1-MeV-Xe-irradiated $Na^+ \leftrightarrow Ag^+$ ion-exchanged borosilicate glass for (a) 1.0×10^{16}, (b) 3.0×10^{15}, and (c) 5.5×10^{14} ions/cm^2, respectively (solid lines). The dashed lines are the results of simulations based on the transfer matrix method and the Maxwell-Garnett effective medium theory.

4.3.4 Discussion

The conclusion that 1-MeV-Xe irradiation of $Na^+ \leftrightarrow Ag^+$ ion-exchanged borosilicate glass induces Ag-nanocrystal nucleation in a layer with a thickness significantly smaller than the corresponding ion range puts a number of earlier published results in a new perspective. First of all, it implies that the reported effective refractive index of the material used for the fabrication of highly dispersive micropatterns is incorrect [54]. That refractive index was derived under the assumption that the Ag nanocrystals were formed in a layer with a thickness of 450 nm. The corresponding analysis, in which the real and imaginary

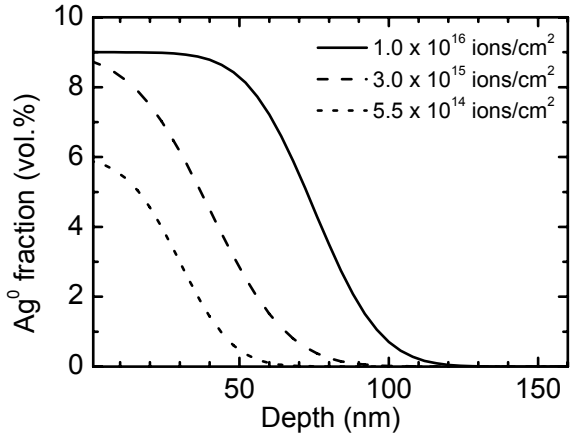

Figure 4.6: Ag^0 depth profiles used as inputs for the simulations of the transmittance and reflectance spectra.

parts of the effective refractive index were considered as independent variables [60] resulted in peak values of 2.6 for the real and 0.15 for the imaginary parts of the refractive index for a Xe fluence of 5.0×10^{15} ions/cm^2 [54]. From Fig. 4.6 it can be seen that an irradiation at a Xe fluence of 5.0×10^{15} ions/cm^2 would lead to an Ag-nanocrystal depth profile with a surface content of $\sim$9 vol.%. For such a composition, the effective refractive index is $2.1 + i0.8$ at the resonance wavelength (l = 430 nm), i.e. a significantly lower value for the real part of the refractive index and a much higher value for the imaginary part compared to Ref. [54]. Consequently, the index contrast of micropatterns fabricated by the described method is lower than originally thought, whereas the extinction is significantly higher. This implies that the material is less attractive for e.g. the realization of (nonlinear) photonic crystals.

Given the present data, the earlier published analysis that atomic displacement energy loss is the main factor for Ag-nanocrystal nucleation in $Na^+ \leftrightarrow Ag^+$ ion-exchanged glass during ion irradiation must be reconsidered [55]. This analysis was based on a comparison of the energy deposition by electronic excitations and by atomic displacements, both integrated over the full ion range. However, the results presented in this paper indicate that that comparison is not necessarily the most relevant one, as nanocrystals are only formed at depths much smaller than the ion range. To study the Ag-nanocrystal formation mechanism, a more extensive investigation, including the analysis of the nanocrystal depth profiles for irradiations with various species, is required. An example of such an analysis is reported by Valentin et al [61]. In that paper, the Cu-nanocrystal formation induced by ion irradiation of Cu-containing glass

is studied. It is reported that, also in that experiment, nanocrystal formation occurs in a depth range that is much smaller than the range of the ions used to induce the nucleation. Our conclusions are in agreement with those results.

Additionally, this paper provides a new perspective for studies of interaction and sensitization effects of Ag nanocrystals and optically active Er ions. In a previous paper [62], it was demonstrated that Ag ions, incorporated into soda-lime silicate glass by ion-exchange (as in the present paper) act as efficient sensitizer for Er, presumably mediated by a defect state related to Ag ions. It was also noted that no sensitization effect of Ag nanocrystals on the Er excitation was observed. With the present knowledge that the nanocrystal depth profile is only shallow, and the Er was implanted deeply, it can now be concluded that no such interaction was to be expected in that work.

Finally, we note that the Ag-nanoparticle-doped glass studied here has been used as starting material for the fabrication of Ag nanoparticle arrays [38]. In that work, 1-MeV-Xe-irradiated $Na^+ \leftrightarrow Ag^+$ ion-exchanged borosilicate glass was subsequently irradiated with 30-MeV Si ions. The Ag nanoparticle arrays show strong optical anisotropy due to differences in transverse and longitudinal surface plasmon modes in the arrays.

4.4 Conclusions

By combining multiple techniques (RBS, XPS, XE-AES, and optical transmittance and reflection measurements), we consistently derived the Ag-nanocrystal depth profile as well as the corresponding refractive index profile of 1-MeV-Xe-irradiated $Na^+ \leftrightarrow Ag^+$ ion-exchanged borosilicate glass. It is shown unambiguously that the Ag nanocrystals are formed in a layer with a thickness of 90 ± 20 nm below the surface (for a Xe fluence of 1.0×10^{16} ions/cm^2). The analysis has put a number of earlier published results, including the apparent absence of influence of Ag nanocrystals on erbium luminescence [62], in a new perspective.

Part II

Plasmon-enhanced Si quantum dot luminescence

Chapter 5

Spectral tunability

In the presence of arrays of Ag nanoparticles, silicon quantum dots exhibit 2- to 6-fold luminescence enhancements at emission frequencies that correspond to the dipole plasmon resonance frequency of the Ag nanoparticles. Using electron-beam lithography to alter the pitch and particle diameter, this wavelength-selective enhancement can be varied as the plasmon resonance wavelength is tuned from 600 to 900 nm. The luminescence intensity enhancement is attributed to coupling of the silicon quantum dot emission dipoles to the plasmon modes of the Ag nanoparticles rather than to an enhanced excitation rate.

5.1 Introduction

Since the observation in 1990 of strong room-temperature photoluminescence from porous silicon [63, 64], significant worldwide interest has been directed toward silicon-based photonics for integrated optoelectronics. An integral part of such systems is a silicon-based, power-efficient light emitter. From that perspective, silicon quantum dots (Si QDs) have been intensively investigated as light sources. Si QDs exhibit room-temperature luminescence due to radiative recombination of quantum-confined excitons, and their emission frequency can be tuned through part of the visible and near-infrared spectrum by varying the QD size [65] or surface termination [66]. Si QDs can have internal quantum efficiencies higher than 50% [67], but they suffer from low radiative decay rates ($\sim$10 kHz) relative to those of direct-bandgap semiconductors and organic dyes ($\sim$100 MHz). Coupling of optical emitters to plasmon modes in metal nanostructures provides an opportunity to enhance the Si QD radiative decay rate [19]. In this way, the intrinsic drawback of the indirect-bandgap material Si can partially be circumvented. An enhanced radiative decay rate leads, under the appropriate conditions, to an enhancement of the emitted intensity, as is discussed in detail in part IV of this thesis.

In this chapter, we report on the enhancement of the photoluminescence (PL) intensity of Si QDs in the vicinity of Ag nanoparticles fabricated by electron-beam lithography. When the plasmon resonance of the Ag nanoparticles is tuned throughout the Si QD emission spectrum, we observe a strong correlation between the frequency at which the PL emission is enhanced and the plasmon resonance frequency. From this behavior, we conclude that the observed PL enhancement is caused by coupling of the Si QD emission dipoles with the plasmon modes of the Ag nanoparticles. This coupling mechanism can cause both an enhancement of the radiative decay rate and an angular redistribution of the emission.

5.2 Experimental

Si QDs were produced by ion implantation of 11-keV Si^+ ions to a fluence of 1.7×10^{16} cm^{-2} into a 1.6-mm-thick fused SiO_2 strip (Technical Glass Products). Monte Carlo simulations performed with SRIM (Ref. [68]) indicate that such an implantation yields a Gaussian depth distribution of Si in the SiO_2, with a peak excess Si concentration of 10% at a depth of 20 nm. The implanted SiO_2 was annealed in Ar for 20 minutes each at 200 and 450 °C, and then for 30 minutes at 1000 °C, to form Si QDs with typical diameters of $3-5$ nm [69]. The samples were subsequently heated in forming gas (10% H_2, 90% N_2) for 30 minutes at 450 °C to eliminate emission from defect states in the SiO_2 matrix [69]. After Si QD formation, the QD distribution was brought to an average depth Δ of 8, 13, or 18 nm from the surface by etching in 2.3% HF (aq). The

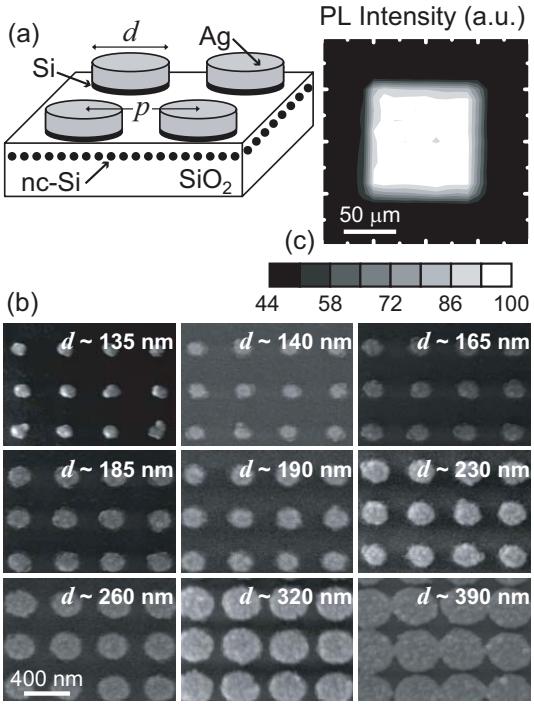

Figure 5.1: (a) Array of Ag nanoparticles with diameter d, and pitch p on Si-QD-doped SiO_2. (b) SEM images of a series of Ag nanoparticle arrays with $p = 400$ nm, $d = 135 - 390$ nm. (c) PL intensity map over a representative Ag array ($p = 400$ nm, $d = 320$ nm, $\Delta = 8$ nm) in 10-μm steps, integrated from $l = 640$ to 950 nm.

etch rate was 0.25 nm/s, as determined by spectroscopic ellipsometry (Sentech SE-850) on an analogous sample of SiO_2 on a Si substrate. Ellipsometry also indicated that after etching, the surface roughness was less than $\sim$0.2 nm.

To obtain strong plasmonic effects, the Si-QD-doped SiO_2 was coupled to Ag nanoparticles. Ag was chosen because it has the lowest absorption at visible frequencies, and therefore produces the strongest field enhancements among all practical metals with plasmon resonances in this spectral range. The Ag nanoparticles were fabricated by electron-beam lithography, as described in Chapter 2. The resulting structure is sketched in Fig. 5.1(a), and scanning electron microscopy (SEM) images of one series of Ag arrays, with a 400-nm pitch and increasing diameters ($135 - 390$ nm), are displayed in Fig. 5.1(b). The size of each array was 100×100 μm^2.

Each array of Ag nanoparticles with height $h = 20$ nm was characterized by a distinct pitch p ($200 - 500$ nm), particle diameter d ($100 - 440$ nm), and

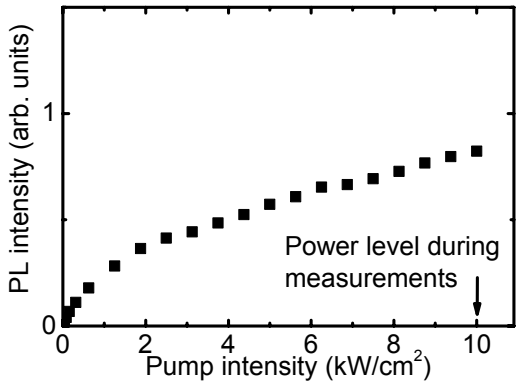

Figure 5.2: Si QD PL intensity as function of pump intensity measured on the unpatterned reference area. The photoluminescence intensity is integrated from $\lambda = 650 - 900$ nm. The pump wavelength is 532 nm.

thus cylinder aspect ratio $a = d/h$ $(5 - 22)$. As a consequence of these geometric differences, the arrays were characterized by distinct plasmon resonance frequencies [41], which were determined by measuring the transmission spectrum through each Ag nanoparticle array. For the transmission measurement, the arrays were illuminated with a white light source incident through a 60× microscope objective (NA = 0.8), and the transmitted light was collected with a 20× microscope objective (NA = 0.4). The spectral transmittance through each Ag nanoparticle array was normalized by the transmittance through a nearby region without Ag nanoparticles.

PL spectra were acquired under excitation from a frequency-doubled Nd:YAG laser operating at λ_{exc}=532 nm focused through a microscope objective to a 10-μm-diam spot. The PL intensity was recorded using a thermoelectrically cooled CCD detector (sensitivity range of $200 - 1100$ nm) in conjunction with a 30-cm-focal-length grating spectrograph. A dichroic filter that absorbs light at wavelengths below 550 nm was used to eliminate incident laser light from the detector. Si QD excitation and PL emission collection were performed both through the Ag arrays and through the SiO_2 substrate, and all of these combinations gave similar results for the enhancement magnitude and spectral dependence, indicating that the Si/Ag system was acting as a coupled entity. Reference luminescence measurements were obtained from a region of Si-QD-doped SiO_2 not located under a Ag nanoparticle array. To check for PL signal uniformity over the range of the 100 μm × 100 μm particle arrays, as well as over the range of the Ag-free reference areas, the samples were mounted on a translation stage and the PL intensity was measured in 10 μm steps. A relatively high pump intensity, 10^4 W/cm^2, was used to ensure operation as

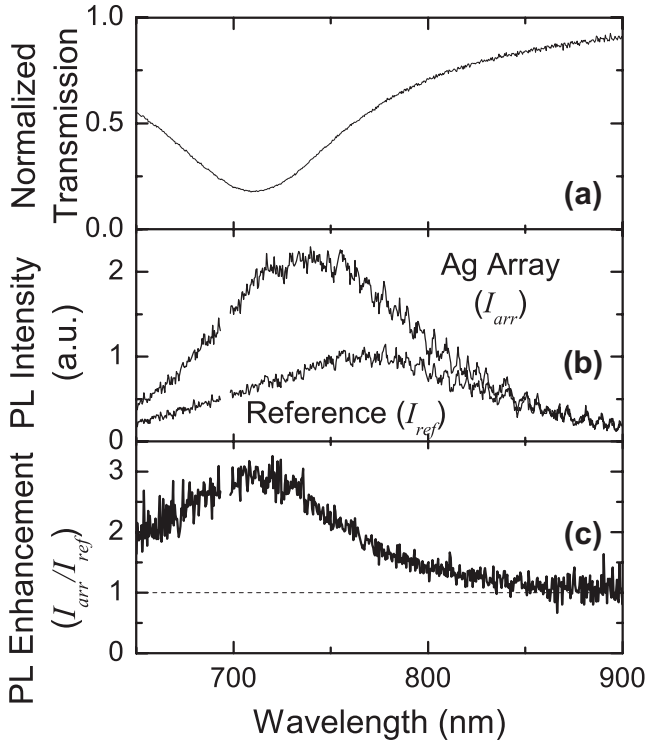

Figure 5.3: Optical characterization of a representative sample (p = 400 nm, d = 320 nm, Δ = 13 nm). (a) Normalized transmission through Ag nanoparticle array. (b) PL intensity from Si QDs in the absence (bottom curve) and presence (top curve) of Ag nanoparticles. (c) PL intensity enhancement (ratio of curves in (b)).

close as possible to the saturated pump power regime, where the PL emission is limited by the radiative decay rate and is independent of the internal quantum efficiency. Figure 5.2 shows the integrated Si QD PL intensity measured on the reference area plotted versus pump intensity. The intensity level at which the measurements on Si QDs coupled to Ag nanoparticles were done is indicated by the arrow. It is shown that the Si QDs were not pumped in complete saturation.

Figure 5.1(c) shows a typical result for a two-dimensional scan (d = 320 nm, p = 400 nm, and Δ = 8 nm). The PL intensity (integrated from λ = 640 to 950 nm) emitted from the array region was approximately twice that emitted from the uncoupled QDs in the reference areas, and the PL intensity was essentially independent of position in both areas. The spatial resolution of this measurement is not sufficient to identify differences in PL intensity at length

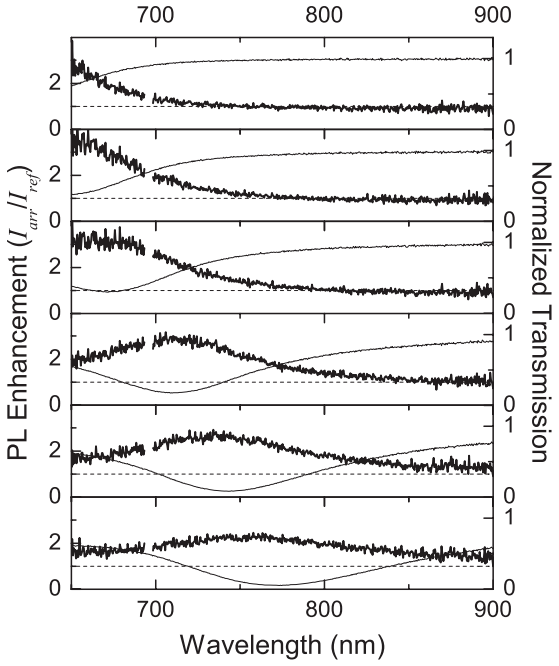

Figure 5.4: PL intensity enhancement and normalized transmission curves for samples with $p = 400$ nm, $\Delta = 13$ nm; d is increasing from top to bottom panel, with $d = 165$, 185, 190, 230, 260, and 320 nm, respectively.

scales smaller than the pitch.

5.3 Results

Figure 5.3 shows the correspondence between the spectral position and shape of the Si QD PL enhancement and the transmission dip associated with the Ag nanoparticles to which these Si QDs are coupled (array parameters: $d =$ 190 nm, $p = 400$ nm, and $\Delta = 13$ nm). The normalized transmission spectrum of the Ag nanoparticles (see Fig. 5.3(a)) exhibits a dip centered at 710 nm that can be attributed to extinction associated with the excitation of plasmon modes in the Ag nanoparticles. As illustrated in Fig. 5.3(b), the PL intensity on the array I_{arr} is enhanced significantly compared to the Si QD PL intensity in the reference area I_{ref}, especially at wavelengths where the plasmon mode is resonant. Figure 5.3(c) shows the PL enhancement spectrum, I_{arr}/I_{ref}. The center wavelength and width of the enhancement peak correspond closely to the center wavelength and width of the transmission dip shown in Fig. 5.3(a).

Figure 5.4 shows normalized transmission and PL enhancement spectra for

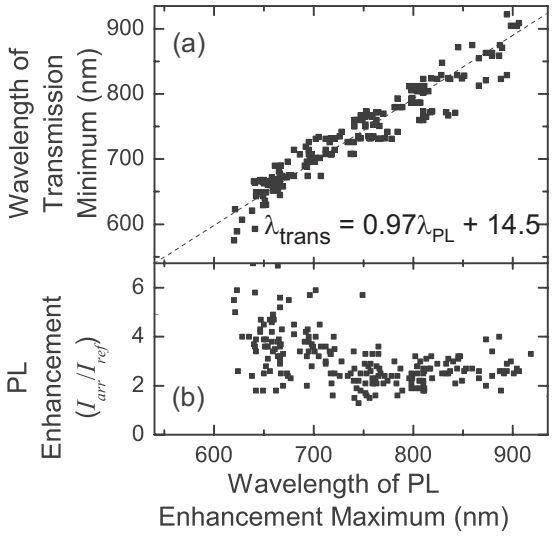

Figure 5.5: (a) Correspondence between the wavelength of minimum transmission and the wavelength of maximum PL enhancement for over 180 different samples. (b) Comparison between the magnitude of maximum PL enhancement and the wavelength at which this maximum is reached for over 180 different samples.

6 samples, with increasing nanoparticle diameter d from top to bottom at a fixed 400-nm pitch and $\Delta = 13$ nm. As d is increased, the transmission dip grows larger in magnitude and shifts to larger wavelengths. The decreased transmission is attributed to an increase in Ag coverage. The shift of the minimum transmission wavelength can be understood qualitatively based on the increase in nanoparticle size and in aspect ratio a (from 8 to 16), which are both known to cause a redshift of the plasmon modes parallel to the long axes of of a nanoparticles [41].

The PL enhancement spectra in Fig. 5.4 exhibit a redshift with increasing d and a that is similar to the trend in transmission dips. Thus, there is a strong correlation between the PL enhancement and the plasmon resonance of the nanoparticles. This correspondence is illustrated for 187 different samples in Fig. 5.5(a), in which the wavelength of minimum transmission is correlated with the maximum PL enhancement wavelength. The observed trend is well fitted by a straight line with a slope of 0.97 ± 0.03 and a y intercept of 14 ± 17 nm.

Despite variations in Δ, p, and d, the strong spectral correspondence between Si QD PL enhancement and particle plasmon resonance indicates that the PL enhancement can consistently be ascribed to coupling of the Si QD emission dipoles with plasmon modes of the Ag nanoparticles. No lumines-

cence enhancements were observed for samples that show transmission dips resonant with the 532-nm excitation source.

Figure 5.5(b) shows the magnitude of the maximum PL intensity enhancement as a function of wavelength for over 180 different samples. Coupling Si QDs to Ag nanoparticle arrays produces up to 6-fold enhancements, and the greatest increases are observed at short emission wavelengths, where smaller nanoparticles are resonant. It is expected that only Si QDs positioned closer to Ag particles than the typical range of $20-50$ nm experience considerable near-field coupling. The total number of Si QDs coupled to Ag nanoparticles thus increases with particle coverage. The fact that a smaller overall PL enhancement is found for larger particles then implies that the emission enhancement per QD must be greater near the smaller particles. The samples considered in Fig. 5.5 have $d = 100 - 440$ nm, $p = 200 - 500$ nm, and $\Delta = 8 - 18$ nm. The large spread in enhancement factors is attributed to variations in the depth at which the Si QDs are positioned in the substrate. This explanation seems most likely as the coupling between Si QDs and plasmon modes depends strongly on separation. No systematic dependence on Δ could be observed, which we ascribe to fabrication tolerances.

5.4 Conclusions

In conclusion, we have observed 2- to 6-fold enhancements in PL intensity of Si QDs upon coupling to Ag nanoparticles. The enhancement can be spectrally controlled between 600 and 900 nm by tuning the plasmon resonance frequency of the Ag nanoparticles through varying the nanoparticle diameter. Coupling to engineered plasmonic structures thus provides an interesting approach to controlling the emission of Si quantum dots. The largest luminescence enhancement that could possibly be obtained using arrays of metal nanoparticles is analyzed in Chapter 11.

Chapter 6

Polarization selectivity

The photoluminescence intensity of silicon quantum dots is enhanced in a polarization-selective way by coupling to elongated Ag nanoparticles. The observed polarization dependence provides direct proof that the PL enhancement is due to electromagnetic coupling of the silicon quantum dot emission dipoles with dipolar plasmon modes of the Ag nanoparticles. The polarization selectivity demonstrates the potential of engineered plasmonic nanostructures to optimize and tune the performance of light sources in a way that goes beyond solely enhancing the emission and absorption rates.

6.1 Introduction

In recent years, the control of spontaneous emission by metallic nanostructures has regained considerable interest following up on the pioneering work that was performed in conjunction with studies on surface-enhanced Raman scattering (SERS) in the 1970s and 1980s [13]. These early investigations, which focused on the interaction of emitters with rough metal surfaces, resulted in the observation of surface-enhanced fluorescence (SEF) [18]. In addition, semi-classical models were developed that describe SEF based on the electromagnetic coupling of dipole emitters with plasmon modes, i.e., collective conduction electron oscillations, in metal nanoparticles [19, 20]. These models predict large modifications of the excitation rate as well as of the radiative and nonradiative decay rates upon coupling emitters to metallic nanostructures.

The renewed interest in plasmon-enhanced fluorescence during the last decade was motivated by advances in both single-molecule spectroscopy and nanoscale fabrication. First, single-molecule spectroscopy provides the possibility to verify theoretical models in great detail, and has led, for example, to the observation of photoluminescence enhancement and quenching depending on the distance between emitter and metal [22], with concomitant changes in excited state lifetime [23, 24]. Second, nanoscale fabrication offers the possibility to engineer plasmonic structures with high precision. This is of crucial importance since fluorescence enhancement and quenching depend differently on nanostructure properties such as material, size, and shape, as well as on emitter-nanostructure separation distance [19, 20]. Only in a limited part of this extensive parameter space can plasmonic nanostructures provide substantial improvements to the radiative properties of emitters.

Apart from influencing the balance between fluorescence enhancement and quenching, the nanostructure geometry also affects the polarization and directionality of the enhanced fluorescence [70]. Experimental evidence of the influence of metallic nanostructures on PL polarization has been attained with single quantum dot measurements on rough metal surfaces [71].

In this chapter, we report on the enhancement of Si QD PL upon coupling the Si QDs to engineered elongated Ag nanoparticles [72]. The observed polarization selectivity enables us to conclude that, under the present excitation conditions, the PL enhancement is due to the coupling of the silicon quantum dot emission dipoles with dipolar plasmon modes in the Ag nanoparticles, rather than due to an enhancement of the excitation rate. This conclusion follows directly from the correspondence between the measured PL and extinction data, and it does not rely on, for example, a rate-equation model. A compelling property of Si QDs that is utilized in this study is their broad emission spectra, which enables the identification of spectral trends in PL enhancement over a wide wavelength range upon varying the nanoparticle properties [73].

6.2 Experimental

Si QDs were produced by ion implantation of 11-keV Si^+ ions to a fluence of 1.7×10^{16} cm^{-2} into a 1.0-mm-thick silica substrate (suprasil, Hereaus). Monte Carlo simulations performed with SRIM (Ref. [68]) indicate that such an implantation yields a Gaussian depth distribution of Si in the SiO_2, with a peak excess Si concentration of 10% at a depth of $\sim$ 20 nm. The implanted silica was annealed in Ar for 20 minutes each at 200 C and 450 °C, and then for 30 minutes at 1000 °C, to form Si QDs with typical diameters of $2 - 5$ nm [74]. The samples were subsequently heated in forming gas (10% H_2, 90% N_2) for 30 minutes at 450 °C to passivate defects. After Si QD formation, the QD distribution was brought to an average depth of about 10 nm from the surface by etching the oxide in 2.3% HF(aq). The etch rate was 0.25 nm/s, as determined by spectroscopic ellipsometry on an analogous sample of SiO_2 on a Si substrate. Ellipsometry also indicated that after etching, the surface roughness was less than $\sim$ 0.2 nm.

On top of the Si-QD-doped SiO_2 substrates, elongated Ag nanoparticles were fabricated based on the electron-beam-lithography procedure described in Chapter 2. Ag was chosen because this metal exhibits the lowest Ohmic damping at visible and infrared frequencies, and thus gives rise to the highest electromagnetic field enhancements. The resulting structure is sketched in Fig. 6.1(a), and a scanning electron micrograph (SEM) image of the array is displayed as an inset in Fig. 6.1(b). The dimensions of these nanoparticles are: $240 \times 140 \times 20$ nm^3.

6.3 Results

6.3.1 Extinction measurements

Due to the anisotropic particle dimensions, the fabricated Ag nanoparticle array exhibits polarization-dependent extinction spectra, as is shown in Fig. 6.1(b). These extinction spectra were measured in an optical microscope by white-light illumination through a 60× objective (NA = 0.8) from the top, and collection through a 20× objective (NA = 0.4) from the bottom, after which the light was passed through a polarizer. The plotted extinction E is defined as $E = 1 - T$, where T is the intensity transmitted through the array relative to the intensity transmitted through the unpatterned reference area. Therefore, the extinction is a measure of the fraction of light that is removed from the forward-propagating beam by absorption and scattering due to the nanoparticles. Figure 6.1(b) shows extinction spectra measured on one particular array for two polarizations angles θ : parallel ($\theta = 0°$) and perpendicular ($\theta = 90°$) to the long axis. For both polarizations, a pronounced peak in extinction can be observed. These relatively broad features can be associated with the excitation of plasmon modes in the Ag nanoparticles [4]. The extinction spectrum

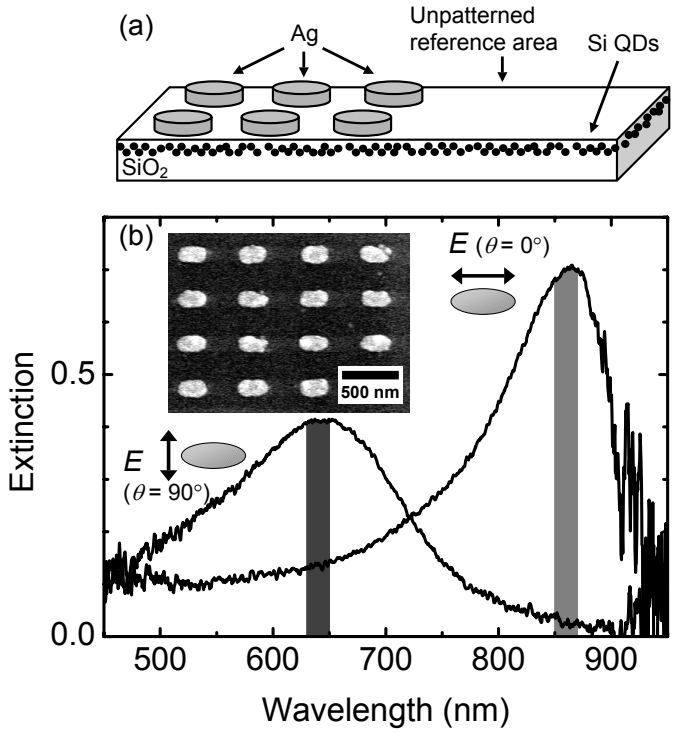

Figure 6.1: (a) Schematic representation of the sample consisting of an SiO_2 substrate, which is doped with Si quantum dots at a depth of about 10 nm, with an array of elongated Ag nanoparticles on top. (b) Extinction spectrum of an array of elongated Ag nanoparticles for two polarizations: parallel and perpendicular to the long axis (both measured at normal incidence). The bars centered at 640 and 860 nm indicate the wavelength ranges that are considered in Fig. 6.2, as well as in Figs. 6.3(b) and (c). Inset: Scanning electron micrograph of the same array (total array size: $50 \times 50\ \mu m^2$).

for ($\theta = 90°$) exhibits a peak at 640 nm, whereas the extinction for ($\theta = 0°$) reaches its maximum around 860 nm. Due to reduced white light intensity as well as reduced detector sensitivity, the extinction spectra are less accurate above 900 nm. The polarization dependence of the extinction can be understood qualitatively based on the fact that the nanoparticle surface charge distributions generated by plane-wave illumination are different for the two polarizations. Accordingly, dissimilar restoring forces are built up, which leads to blue- and red-shifted resonance frequencies for transverse and longitudinal polarizations, respectively. The extinction spectra do not exhibit features that

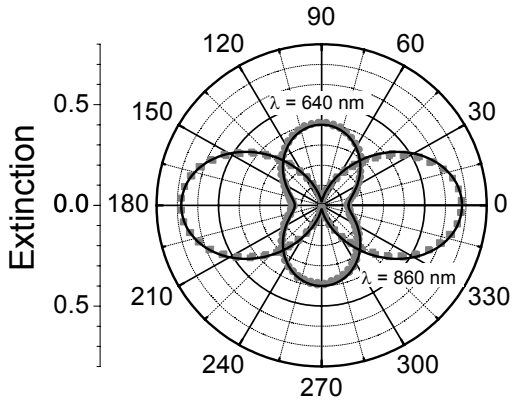

Figure 6.2: Polar plot of the extinction as a function of the polarization angle θ relative to the nanoparticle long axis measured on an array of elongated Ag nanoparticles for two wavelengths: 640 and 860 nm (symbols). The solid lines are fits to the experimental data by dipole patterns (see text).

indicate a diffractive response of the nanoparticle array [75–77], which implies that, for the present geometry, interparticle coupling is relatively weak.

Figure 6.2 shows a polar plot of the extinction as function of the polarization angle θ for two characteristic wavelengths: 640 nm and 860 nm. The data exhibit dipole-like polarization patterns that are oriented perpendicular to one another. In fact, the measured extinction data for 860 nm can be fitted perfectly by a dipole pattern: $E = A\cos^2\theta$, with $A = 0.68$ (solid line), where 0.68 corresponds to the extinction at 860 nm measured at $\theta = 0°$, as shown in Fig. 6.1(b). The polar plot of the extinction at 640 nm can be fitted very well by a superposition of two dipolar patterns that are oriented perpendicular with respect to one other: $E = B\sin^2\theta + C\cos^2\theta$, with $B = 0.40$ and $C = 0.14$ (solid line). These numbers are in agreement with the extinction values at 640 nm for the two spectra shown in Fig. 6.1(b); the second term thus represents the tail of the longitudinal extinction feature. The good agreement between the experimental data and the fits shows that the extinction is dominated by the dipolar plasmon modes of the Ag nanoparticles. The fact that higher-order multipole modes do not need to be invoked is attributed to the small dimensions of the nanoparticles compared to the wavelength of light.

6.3.2 Photoluminescence measurements

On the same array for which the extinction was measured, PL spectra were acquired under excitation from a frequency-doubled Nd:YAG laser operating at

$\lambda_{exc} = 532$ nm that was focused onto the sample surface through a microscope objective to a 10-μm-diameter spot (corresponding to an area containing 500 nanoparticles). A relatively high pump power, 10^4 W/cm^2, was used to ensure operation as close as possible to the saturated pump power regime, where the PL emission is limited by the radiative decay rate and is independent of the internal quantum efficiency. The polarization of the pump source was kept constant during all measurements. The PL intensity was collected from the bottom, passed through a polarization analyzer, and subsequently recorded using a thermoelectrically cooled CCD detector in conjunction with a 30-cm-focal-length grating spectrograph. A dichroic filter that absorbs light below 550 nm was used to eliminate incident laser light from the detector.

Figure 6.3(a) shows PL spectra measured on the unpatterned reference area and on the nanoparticle array, the latter for two polarization angles: $\theta = 0°$ and $\theta = 90°$. The reference spectrum is a typical ensemble-averaged Si QD PL spectrum that spans a relatively wide wavelength range ($600-1000$ nm), which is due to both homogeneous and inhomogeneous broadening. The PL intensity on the array is found to be enhanced in a strongly wavelength- and polarization-dependent way compared to the reference. The maximum enhancements at the emission wavelengths of $\lambda_{em} = 640$ nm and $\lambda_{em} = 860$ nm, for $\theta = 90°$ and $\theta = 0°$ respectively, exceed a factor of 3. Such enhancement values can be observed by collecting through the substrate as well as from the top side [73]. These numbers represent ensemble-averaged values, and much larger enhancements are expected at lightning-rod-type hotspots close to the sharp corners of the Ag nanoparticles.

To enable a more detailed analysis of the polarization dependence of the PL enhancement, Figs. 6.3(b) and (c) display polar plots of the PL intensity as function of the polarization angle of the emission measured both on the array and on the unpatterned reference area for $\lambda_{em} = 640$ nm and $\lambda_{em} = 860$ nm. We focus on these two wavelengths since they correspond to the extinction maxima for the transverse and the longitudinal polarization, respectively. For both wavelengths, the PL intensity on the reference area (circular line in the center of each plot) is polarized isotropically, so the data are not dependent on the polarization of the pump light. Indeed, the absence of polarization memory has also been observed for single Si QDs. Furthermore, any orientation dependent emission due to a small size anisotropy for single Si QDs [78] is expected to be averaged out for Si QD ensembles in an amorphous SiO_2 matrix [78].

As can be seen in Figs. 6.3(b) and (c), the PL intensity on the array is enhanced compared to the reference. Moreover, this enhancement is polarized in the same direction as the extinction at the emission wavelength, both for $\lambda_{em} = 640$ nm and $\lambda_{em} = 860$ nm (see Fig. 6.2). Note that these perpendicularly oriented PL enhancement patterns, including the supporting extinction data, were obtained from a single array of elongated Ag nanoparticles. Besides, the PL measurements were done without changing the polarization

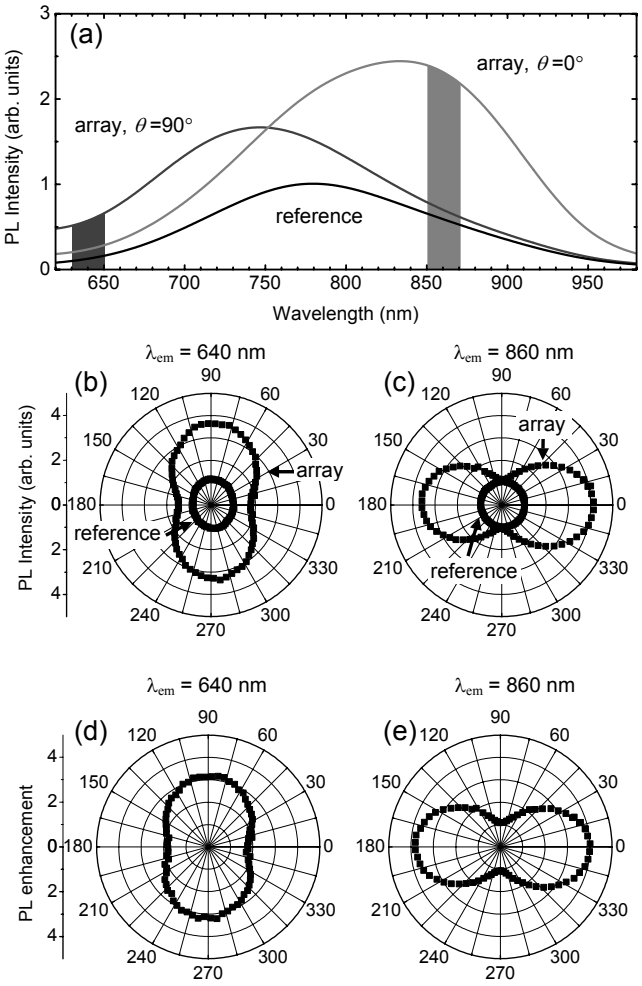

Figure 6.3: (a) Si quantum dot photoluminescence spectra measured on the reference area and on the array, the latter for two emission polarization angles q (relative to the nanoparticle long axis): $\theta = 0°$ and $\theta = 90°$. The bars indicate the wavelength ranges that are considered in (b) and (c). (b) Polar plot of the Si QD photoluminescence as function of θ for $\lambda_{em} = 640$ nm. (c) Similar data as in (b) for $\lambda_{em} = 860$ nm. (d) Polar plot of the Si QD photoluminescence enhancement as function of θ for $\lambda_{em} = 640$ nm. (e) Similar data as in (d) for $\lambda_{em} = 860$ nm. Pump wavelength: 532 nm.

of the pump light, so the excitation conditions for the array measurements at $\lambda_{em} = 640$ nm and $\lambda_{em} = 860$ nm were completely identical. Consequently, the striking correspondence between the polarization dependence of the extinction at the emission wavelength on one hand, which can be associated with dipolar plasmon modes, and the polarization dependence of the PL enhancement on the other hand shows that the PL enhancement is due to the electromagnetic coupling of the Si QD emission dipoles with dipolar plasmon modes of the Ag nanoparticles.

It can be noted that the profiles in Figs. 6.3(b) and (c) are not completely symmetric for rotation over 180°. For example, the PL intensity on the array is higher at $\theta = 0°$ than at $\theta = 180°$ in Fig. 6.3(c). This asymmetry is attributed to a small misalignment in our setup. Indeed, by normalizing the angular profiles of the arrays by the reference data, perfectly symmetric curves are observed, is seen in Figs 6.3(d) and (e).

The correspondence between the polarization dependences of the PL enhancement on one hand and the extinction at the emission wavelength on the other hand strongly suggests that the observed PL enhancement is not caused by a plasmon-induced enhancement of the Si QD excitation rate. In particular, at the emission wavelength of 860 nm, the emission polarized perpendicular to the long axis ($\theta = 90°$) is hardly enhanced (see Fig. 6.3(c)). This is attributed to the fact that at 860 nm there is basically no spectral overlap with plasmon modes, for $\theta = 0°$ (see Fig. 6.1), so there can be no resonant coupling of the Si QD emission dipoles with the plasmon modes at this wavelength. However, if the observed PL enhancement would be partially caused by an enhanced excitation rate, the enhancement shown in Fig 6.3(c) should contain an emission-polarization-independent contribution, which would be present at $\theta = 90°$ as well. The fact that such a contribution is not observed indicates that the PL enhancement is not caused by a plasmon-induced enhancement of the optical excitation rate.

In order to verify this hypothesis more explicitly, we performed a control experiment in which we measured the PL enhancement as function of pump polarization. Ag nanoparticle arrays with a slightly smaller aspect ratio than those in Fig. 6.3, covered with a 20-nm-thick Si layer were used. As shown in Fig. 6.4(a), these samples too exhibit polarized emission, at their resonance wavelength of 790 nm (measured for a fixed pump polarization). The polarized emission is indicative of the anisotropic plasmonic properties of the Ag nanoparticles. Figure 6.4(b) displays a polar plot of the PL enhancement versus polarization angle of the pump light (measured without polarization filtering of the emission). This graph shows a completely isotropic response, and therefore it can be concluded that the observed PL enhancement is not caused by a plasmon-induced enhancement of the Si QD excitation rate.

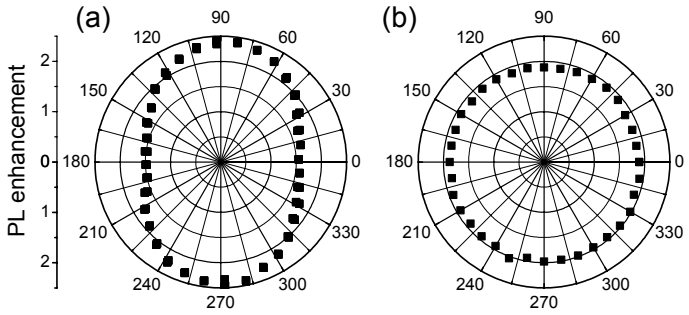

Figure 6.4: Polar plots of the Si QD photoluminescence intensity versus the polarization angle of (a) the emission and (b) the pump light, both with respect to the long axis of the nanoparticles. Emission wavelength: 790 nm. Pump wavelength: 532 nm.

6.4 Conclusions

In conclusion, we have observed a polarization-selective PL intensity enhancement upon coupling Si QDs to engineered elongated Ag nanoparticles. The dependences of the PL enhancement on pump and emission polarization show unambiguously that the PL enhancement is due to the electromagnetic coupling of the Si QD emission dipoles with dipolar plasmon modes in the Ag nanoparticles. The polarization selectivity enables us to draw this conclusion without relying on, for example, rate-equation models. The measured ensemble-averaged PL enhancements exceed a factor 3, and much larger enhancement values are expected close to the sharp corners of the metal nanoparticles. The observed polarization selectivity demonstrates that plasmonic nanostructures enable the optimization of light sources not only by enhancing emission rates, but also by affecting the polarization of the enhanced emission.

Chapter 7

Electroluminescence

Ag nanoparticles were integrated in field-effect light emitting devices fabricated using processing facilities at Intel Inc. The Si QD electroluminescence intensity of these devices was enhanced by up to a factor 2.5. The largest enhancement was not measured on an array of well-defined Ag nanoparticles, but on a device area covered with a 20-nm-thick Ag film. This trend, which differs strongly from the behavior found in Chapters 5 and 6, is attributed to the relatively large RMS roughness (5 nm) of the polysilicon surface on which the Ag was deposited. The hypothesis is that this roughness gave rise to the formation of ensembles of Ag aggregates much smaller than the lithographically defined structures, and that these aggregates dominate the scattering properties of the Ag. The performed photoluminescence and electroluminescence measurements are not conclusive on the enhancement mechanism, but the influence of nanoscale roughness on the outcoupling efficiency seems an important factor.

7.1 Introduction

In the previous two chapters, it was described that the photoluminescence (PL) intensity of silicon quantum dots (Si QDs) can be enhanced by Ag nanoparticles. The observed spectral and polarization selectivity demonstrated that the measured PL enhancement was due to coupling of the Si QD emission dipoles to plasmon modes rather than due to an enhanced optical excitation rate. The conclusion that the enhancement was not caused by an enhanced optical excitation rate implies that the concept of emitter-plasmon coupling could also be applied to enhance the luminescence intensity of electrically driven light sources.

In this chapter, we describe the integration of arrays of Ag nanoparticles, similar to those described in Chapters 5 and 6, in CMOS-compatible field-effect light emitting devices (FELEDs) [79]. The active layer in these devices consists of a 15-nm-thick SiO_2 film that is doped with Si QDs. Originally, these devices were designed to study the luminescence properties of Si QDs under variable charging conditions [80]. After postprocessing the FELEDs, we have studied the luminescence intensity enhancement induced by the integrated Ag nanoparticles. A 2- to 3-fold enhancement in the luminescence intensity was detected under both optical and electrical excitation. The origin of the detected luminescence enhancement is discussed.

7.2 Experimental

7.2.1 Device structure

The FELEDs used in the experiment are composed of MOS ring gate transistors that were fabricated at a 300-mm-wafer facility at Intel Corporation in Hillsboro, Oregon. First, a 15-nm-thick dry thermal oxide was grown on a p-type silicon wafer at 900 °C. Si^+ ions were then implanted into the oxide to an average depth of 10 nm and to a peak concentration of 20 at.%. The implanted wafers were annealed for 5 minutes at 1050 °C in 2% oxygen in argon to nucleate and grow Si QDs in the SiO_2 layer. Subsequently, a 40-nm-thick polysilicon layer was deposited above the Si-QD-doped SiO_2 by low-pressure chemical vapor deposition at 600 °C. The ring gate MOS transistors were created in this stack using standard photoresist patterning and reactive ion etching techniques to remove both the polysilicon gate and the Si-QD-doped SiO_2 from the source and drain regions in a single-mask process. Finally, the sample was implanted with P^+ and As^+ to degenerately dope the source, drain, and gate regions. FELEDs fabricated in this way showed electroluminescence as described in Ref. [79].

To study the coupling between Ag nanoparticles and electrically excitable Si QDs, the polysilicon gate was thinned down. First, the native oxide was removed from the silicon surface by an etch of 5 seconds in buffered hydrofluoric

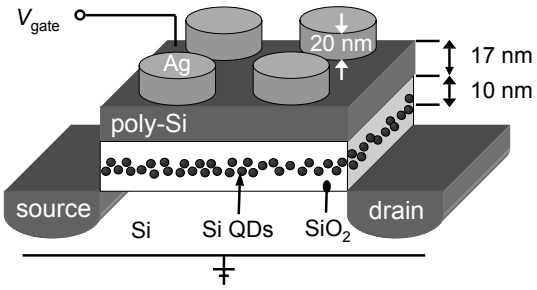

Figure 7.1: Schematic of the field-effect light-emitting device (FELED). The polysilicon gate has been thinned down to ∼17 nm, and Ag nanoparticles have been fabricated on top of the device. Under the gate, the 15-nm thick SiO_2 film contains Si QDs at an average depth of 10 nm. In the experiments, the semitransparent gate was biased with a voltage V_{gate} relative to source and drain.

acid (7.2% HF (aq), 36% NH_4F (aq)). Then, following a rinse in 18 MΩ·cm resistivity water, the silicon was etched for 10 seconds in a solution of 1 ml HF and 150 ml nitric acid (HNO_3). This solution etches polysilicon at a rate of ∼2 nm/s, and may also roughen the surface [81]. By ellipsometry, we verified that the top gate thickness was reduced to about 17 nm. FELEDs with this top-gate thickness still showed electroluminescence after postprocessing, in contrast to devices that were etched further down.

An Ohmic contact to the gate was made by photolithographical patterning and by the thermal evaporation of a 10-nm-thick chrome wetting layer and a 200-nm-thick gold pad. The *p*-type silicon backside of the device was metalized by thermal evaporation of a 200-nm-thick aluminum layer, followed by a 12-hour anneal at 100 °C.

The thinned devices were covered with arrays of Ag nanoparticles using an electron-beam lithography procedure similar to the protocol described in Chapter 2. The final sample structure is schematized in Fig. 7.1.

7.2.2 Optoelectronic characterization

Photoluminescence (PL) and electroluminescence (EL) spectra of the Si QDs were measured in an inverted optical microscope. For this purpose, the devices were mounted on a homemade package to which the gate contacts were connected using gold wires adhered with a wedge bonder. An image of a sample is shown in Fig. 7.2(a). Multiple Ag nanoparticle arrays, of 50 × 50 μm^2 in size, characterized by different array pitches and disk diameters are shown in Fig. 7.2(b). The increasing contrast from left to right reflects the increasing Ag coverage for the successive arrays. The dark areas on the righthand side

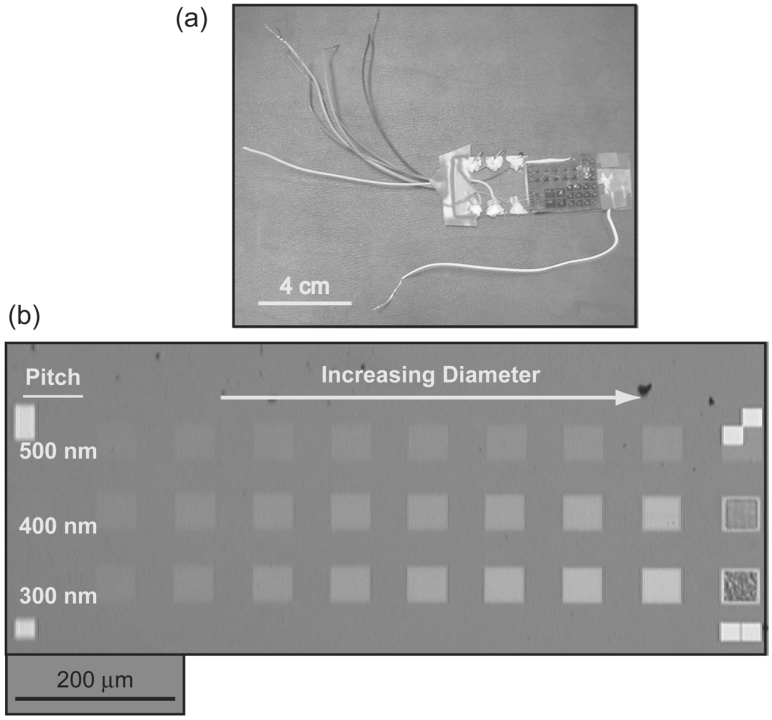

Figure 7.2: (a) Image of a packaged sample with several post-processed field-effect light-emitting devices (FELEDs). (b) Optical image of multiple arrays of Ag nanoparticles with different disk diameters and array pitches on a single FELED. The total surface area of the FELED is 10×10 mm^2.

are totally covered with a 20-nm-thick Ag film, instead of with an array of nanoparticles.

Photoluminescence measurements were performed by pumping the devices through the polysilicon top gate with the 488-nm line of an Ar^+ laser. Electroluminescence spectra were measured by applying a square-wave input voltage between the gate and the p-type silicon backside. The voltage level of the square-wave input was swapped between plus and minus $6-9$ V at a frequency of 5 kHz. In both situations, the luminescence signal was collected using a $50\times$ objective (NA $= 0.45$). The field of view was limited to 20×20 μm^2. The signal was detected using a silicon CCD detector array (sensitivity range $200-1100$ nm), cooled with liquid nitrogen to -130 °C, in conjunction with a 27.5-cm-focal-length grating spectrograph.

PL lifetime measurements were performed by chopping the 488-nm pump beam with an acousto-optic modulator (AOM). The luminescence in a 50-

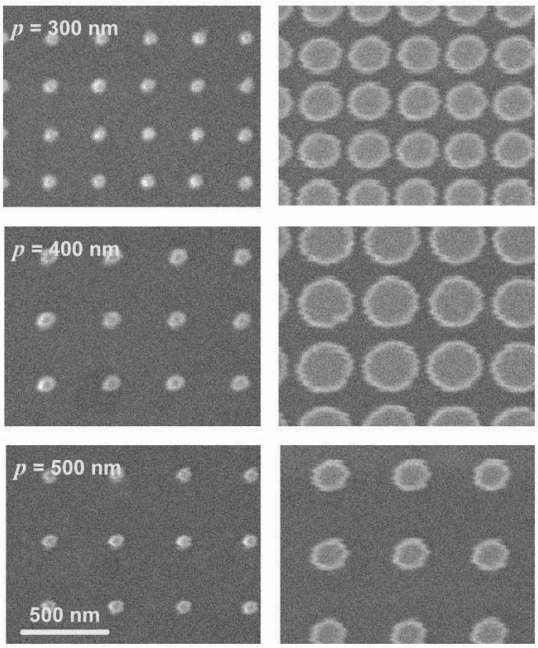

Figure 7.3: Scanning electron microscopy (SEM) images of Ag nanoparticle arrays on top of the light-emitting devices. The scale bar for all images is displayed in the left bottom corner. The array pitch is indicated by p for all three rows separately.

nm-wide band around the luminescence peak wavelength was selected with a spectrograph and detected by a thermo-electrically cooled photomultiplier tube.

For both the photoluminescence and electroluminescence measurements, the signal detected on the arrays was compared to the signal measured on the surrounding reference area. This reference area was located on the same electrical device as the arrays.

7.3 Results and discussion

Scanning electron microscopy (SEM) images of some of the arrays of Ag nanoparticles positioned on top of the existing FELEDs are shown in Fig. 7.3, for different disk diameters and pitches.

Under both optical and electrical excitation, the detected Si QD luminescence intensity was affected by the presence of the Ag nanoparticles. The photoluminescence measurements showed an enhancement of the PL intensity

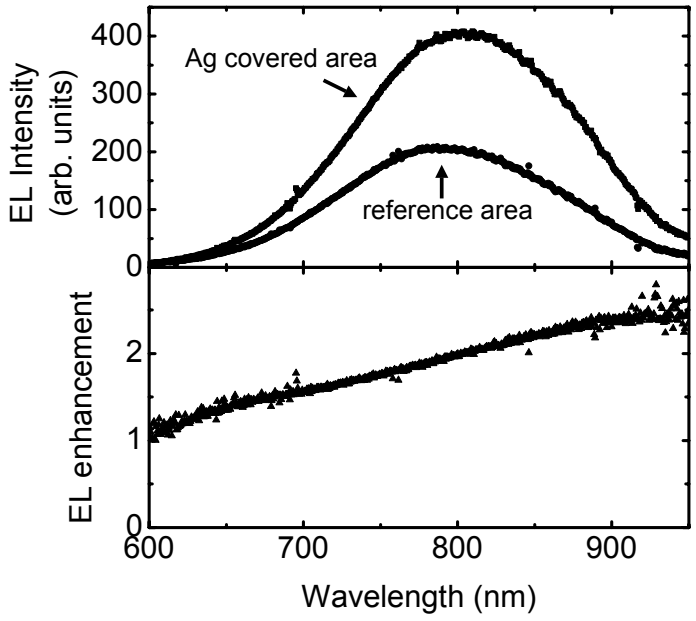

Figure 7.4: (a) Electroluminescence spectra measured on a device area covered by a 20-nm-thick Ag film and on a reference area without Ag. (b) Electroluminescence enhancement obtain by dividing the electroluminescence intensity on the Ag covered area by the reference measurement.

by up to a factor 2 compared to the surrounding reference area. An important difference with respect to the measurements done on silica substrates (Chapter 5), however, is that no systematic change in PL spectrum was observed when nanoparticle size or shape were varied. The only clear trend is that the PL enhancement increases with Ag coverage. This behavior, which is opposite from the trend found for the samples on silica substrates (Chapter 5), is discussed in more detail within the context of the EL measurements further on.

PL lifetime measurements yielded decay curves that were fitted with a stretched exponential function with $\tau = 10$ μs and $\beta = 0.7$. No significant difference was detected between array and reference areas. The fit results for τ and β are consistent with measurements performed on the FELEDs before postprocessing [80]. The small value for τ compared to the radiative lifetime of $\sim$100 μs for Si QDs in SiO_2 emitting at the same same wavelength [67, 82], indicates that strong nonradiative decay channels are active.

Measurements of the electroluminescence intensity showed a similar trend as the photoluminescence measurements: the intensity on the Ag-covered ar-

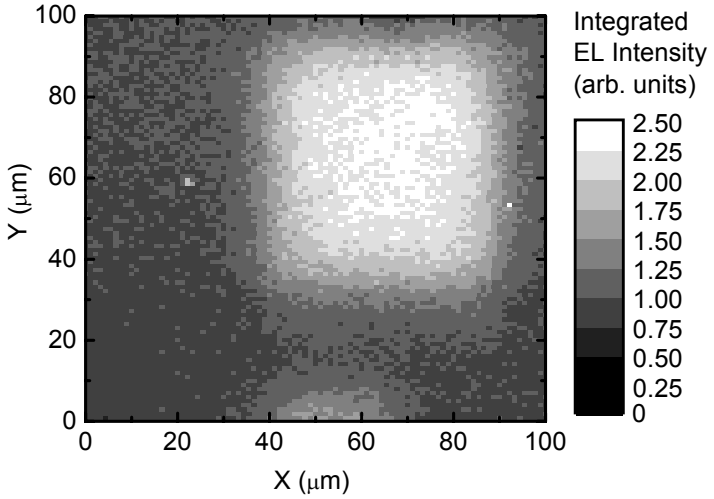

Figure 7.5: Electroluminescence intensity map of an area of 100×100 μm^2 that contains a 50×50 μm^2 area (top right) where the device is covered with a 20-nm-thick rough Ag film. The emission is integrated from $\lambda = 600 - 1100$ nm.

eas is enhanced compared to the reference area (by up to a factor 2.5), and the enhancement increases with Ag coverage. Remarkably, the highest EL enhancement is observed for a 20-nm-thick Ag film rather than for an array of Ag nanoparticles. For the 20-nm-thick Ag film, the measured EL spectrum is shown in Figure 7.4(a), together with the reference spectrum. Figure 7.4(b) shows the corresponding EL enhancement spectrum. A possible explanation for the fact that the EL enhancement is optimal for the Ag film rather than for a Ag nanoparticle array is related to the polysilicon etch used to thin down the top gate. This process resulted in an RMS roughness of 5 nm, as was determined by atomic force microscopy (AFM) [83]. The roughness might have induced the formation of ensembles of small Ag aggregates with plasmon properties independent of the lithographically defined structures. If these Ag aggregates exhibit the strongest plasmon resonances in the infrared, analogous to the spontaneously formed Ag nanoparticles described in Chapter 3, then that could also explain the increasing EL enhancement with increasing emission wavelength, as shown in Fig. 7.4(b).

To illustrate the EL uniformity over a 50×50 μm^2 area of a 20-nm-thick Ag film, as well as over the reference area, Figure 7.5 shows a map of the EL intensity acquired using the CCD detector in imaging mode (emission integrated over $\lambda = 600 - 1100$ nm). The EL intensity is constant over the array

at roughly twice the intensity of the reference area.

Due to the fact that no change in Si QD luminescence lifetime between Ag-covered areas and reference areas was detected, the experiment is not conclusive on the enhancement mechanism. It is known, however, that nanoscale roughness can enhance the outcoupling efficiency of light-emitting devices by scattering light out of high-index structures, in which light would otherwise be trapped by total internal reflection [6]. It is likely that this effect plays an important role here as well.

7.4 Conclusions

The electroluminescence intensity of Si QD FELEDs was enhanced by Ag nanoparticles. The nanoparticles were fabricated on top of existing FELEDs after the polysilicon gate was thinned down to a thickness of about 17 nm. No correlation between the luminescence enhancement and the Ag geometry defined by electron-beam lithography was observed. We attribute the absence of such a correlation to the formation of small Ag aggregates due to the roughness of the etched polysilicon layer on top of which the Ag was deposited.

Part III

Erbium ions coupled to Ag or Si nanostructures

Chapter 8

Plasmon-enhanced erbium luminescence

It is demonstrated that the photoluminescence intensity of optically active erbium ions positioned in close proximity of anisotropic Ag nanoparticles is significantly enhanced if the nanoparticles support plasmon modes that are resonant with the erbium emission. In addition, the photoluminescence enhancement is found to be polarized corresponding to polarization of these plasmon modes. Both observations demonstrate that the photoluminescence intensity enhancement is due to coupling of the Er^{3+} $^4I_{13/2}$ $-^4$ $I_{15/2}$ transition dipoles with plasmon modes in the Ag nanoparticles. As this coupling mechanism is known to affect the emission rate, metal nanoparticles provide the opportunity to reduce temperature or concentration quench processes that are known to occur in a wide range of erbium-doped materials.

8.1 Introduction

Erbium-doped materials are of great interest in optoelectronics due to the Er^{3+} intra-4f emission at 1.54 μm, a standard telecom wavelength. Dielectrics doped with erbium can be used to fabricate planar optical amplifiers [84] and lasers [85], as well as light-emitting devices [86]. Erbium doping of silicon enables the realization of optoelectronic devices based on the most widely used semiconductor in microelectronics [87, 88]. For all Er-doped materials, however, a practical limitation is that due to the small oscillator strength of the Er^{3+} intra-4f transition at 1.54 μm ($^4I_{13/2} - ^4I_{15/2}$), loss processes can easily dominate the deexcitation of the $^4I_{13/2}$-level. For instance, in Er-doped dielectrics, the Er concentration needs to be kept low to avoid concentration quenching and cooperative upconversion [89]. Concentration quenching concerns energy migration to defect states or OH-groups by resonant interaction between closely spaced Er^{3+} ions. Cooperative upconversion, which can dominate the deexcitation of the Er^{3+} $^4I_{13/2}$-level already at Er^{3+} concentrations as low as $\sim$0.02 at.% [89], results in depopulation by energy exchange between two excited Er^{3+} ions.

In Er-doped Si, temperature quenching is the main constraint for device applications [90, 91]. It is caused by phonon-assisted energy backtransfer [89, 92], and Auger interactions with free carriers [91]; two processes that strongly limit the quantum efficiency of optical transitions in Er^{3+} at room temperature. Engineering of the Er sites, for example by oxygen co-doping [90], as well as device engineering [93] have not reduced the significance of these nonradiative processes sufficiently in order to turn Er-doped Si into a practical optoelectronic material.

An alternative approach to diminish the effect of quenching, which is different from limiting nonradiative processes, consists of enhancing the spontaneous emission rate of the Er^{3+} $^4I_{13/2} \rightarrow ^4 I_{15/2}$ transition by modifying the dielectric environment [94, 95]. Very strong effects of the environment on the emission rate are predicted for emitters that are positioned in close proximity of metal nanoparticles [19]. If a plasmon mode, i.e., a collective conduction electron oscillation [4], in a metal nanoparticle is resonant with an optical transition, the electromagnetic coupling between transition dipole and plasmon mode can result in an enhancement of the radiative decay rate by several orders of magnitude for emitter-nanoparticle separation distances of $\sim 5 - 20$ nm. At shorter distances, the presence of the metal leads to quenching [19].

Recently obtained results on the interaction between emitters and metal nanoparticles include the observation of an excited state lifetime reduction simultaneous with a photoluminescence (PL) enhancement [23, 24], and the observation of a continuous transition from PL enhancement to PL quenching upon varying the emitter-nanoparticle separation distance [22]. Besides, it has been demonstrated that the plasmon-induced enhancement of the luminescence of silicon quantum dots can be tuned spectrally [73], and can be polarized [96] by modifying the geometrical properties of the metal nanoparticles.

Most of the work on interactions between emitters and metal nanoparticles has been done with dyes or quantum dots that emit at wavelengths between 500 nm and 900 nm, a spectral range for which it is relatively easy to obtain resonant plasmon modes. However, enhancing the Er^{3+} radiative decay rate at 1.54 μm by employing resonant plasmon modes could be very attractive as well, especially in view of the opportunity to reduce the significance of various quench processes, including temperature quenching of Er in Si.

In this chapter, we report on the coupling of optically active Er^{3+} ions with plasmon modes in Ag nanoparticles. First, it is shown that by engineering Ag nanoparticles with a strong geometrical anisotropy, plasmon modes with a resonance wavelength of 1.5 μm can be obtained. Secondly, it is shown that the PL intensity of Er^{3+} ions positioned close to these nanoparticles is significantly enhanced. The dependences of the PL enhancement on both nanoparticle geometry and polarization demonstrate that the PL enhancement is due to coupling of the Er^{3+} $^4I_{13/2}$ $-^4$ $I_{15/2}$ transition dipoles with plasmon modes in the Ag nanoparticles.

8.2 Sample fabrication

The sample preparation was done in the following way. First, a 1-mm-thick SiO_2 substrate was covered with a 45-nm-thick sacrificial Al layer. Subsequently, the sample was implanted with 1.2×10^{16} Er ions/cm^2 at 150 keV, after which the Al layer was etched off in a 1:10 solution of KOH in water. As a result, the SiO_2 substrate was doped with 9×10^{15} Er ions/cm^2 in the top 50 nm, with a maximum concentration of 4 at.% at a depth of 10 nm. In order to obtain a model system in which the Er luminescence is quenched considerably, the sample was not annealed. The PL lifetime at 1.54 μm was less than 0.5 ms, which indicates that the internal quantum efficiency for emission is smaller than $\sim$3%, since the radiative lifetime of Er^{3+} in SiO_2 is 18 ms [97].

On top of the Er-doped SiO_2 substrate, Ag nanoparticles were fabricated using electron-beam lithography, by the procedure that is described in Chapter 2. Ag was chosen because this metal exhibits the lowest Ohmic damping at visible and infrared frequencies, and thus gives rise to the highest electromagnetic field enhancements [4]. The resulting structure is schematically depicted in Fig. 8.1(a), and scanning electron micrograph (SEM) images of the arrays are displayed in Fig. 8.1(b). From top left to bottom right, the Ag nanoparticle length l is increased from $\sim$100 nm to $\sim$600 nm, while the nanoparticle width is kept nearly constant at $\sim$100 nm. The height of all Ag nanoparticles is 20 nm, so that the smallest nanoparticles can be considered as circular disks, whereas all the other nanoparticles are elongated disks.

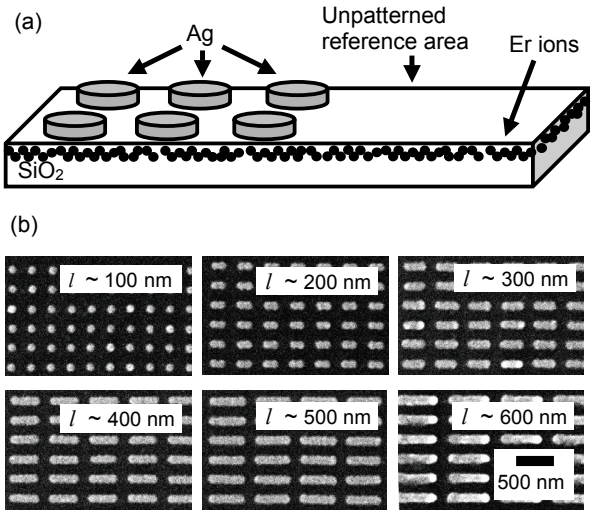

Figure 8.1: (a) Schematic representation of the sample consisting of an SiO_2 substrate, which is doped with Er ions in the upper 50 nm, with an array of Ag nanoparticles on top. (b) Scanning electron micrographs of six arrays of Ag nanoparticles. The nanoparticle length l is increased from ∼100 nm to ∼600 nm, while the width is kept constant at ∼100 nm. The height of the nanoparticles is 20 nm for all arrays

8.3 Optical characterization

The degree of geometrical anisotropy strongly influences the resonance frequencies of the nanoparticle plasmon modes, as can be seen in Fig. 8.2, which displays the transmission spectra of the arrays. These transmission spectra were measured at normal incidence with unpolarized light by illumination through a 60× microscope objective (NA=0.8) and collection through a 20× microscope objective (NA=0.4). The transmission through each Ag nanoparticle array was normalized by the transmission through an unpatterned reference area.

As can be seen in Fig. 8.2, the transmission spectrum of the circular disks ($l \sim 100$ nm) exhibits a broad dip centered at 2.1 eV, which can be attributed to absorption and scattering due to excitation of dipole plasmon modes in the Ag nanoparticles [4]. The spectral position of this dip depends on nanoparticle size and shape, the refractive index of the embedding media, and on coupling between the nanoparticles [4]. Note that in the Er emission band around 0.81 eV, which is indicated by the vertical gray band, the transmission for this array is nearly unity.

For the smallest elongated nanoparticles ($l \sim 200$ nm), the transmission

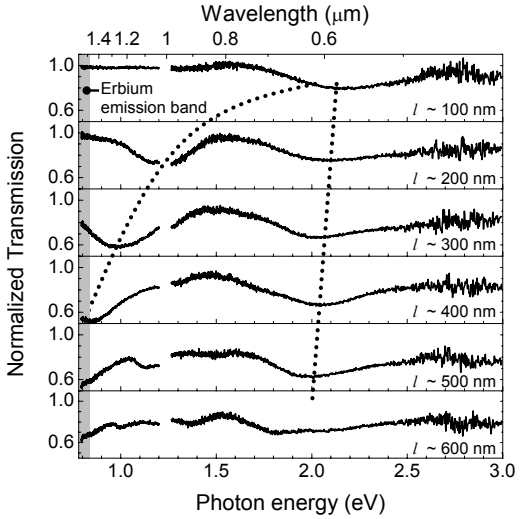

Figure 8.2: Transmission spectra of six Ag nanoparticle arrays, with the nanoparticle length l increasing from ∼100 nm to ∼600 nm. The dotted lines indicate the evolution of the transmission dips as function of the nanoparticle length. The erbium emission band is indicated by the gray bar.

spectrum is characterized by two dips. This is due to the fact that the degeneracy for the two polarizations is lifted. The low-energy dip is associated with the longitudinal plasmon mode (parallel to the long axis), whereas the high-energy dip is associated with the transverse plasmon mode (perpendicular to the long axis) [4]. The low-energy dip can be shifted towards the erbium emission band by increasing the anisotropy, as can be seen for $l \sim 300$ nm and $l \sim 400$ nm, and as is indicated by the left dotted line in Fig. 8.2. By further elongation, the low-energy dip shifts out of the detector range. Additional features appearing between 1.0 eV and 1.5 eV are attributed to the excitation of higher-order plasmon modes.

8.3.1 Spectral characteristics

In order to study the influence of the metal nanoparticles on the Er luminescence, PL spectra were acquired under excitation from a frequency-doubled Nd:YAG laser operating at $\lambda_{exc} = 532$ nm focused through 60× microscope objective (NA=0.8) from above the sample (see Fig. 8.1(a)) to a 10-μm-diameter spot. The PL intensity was collected from the bottom with 20× microscope objective (NA=0.4) and recorded using a charge-coupled device (CCD) detec-

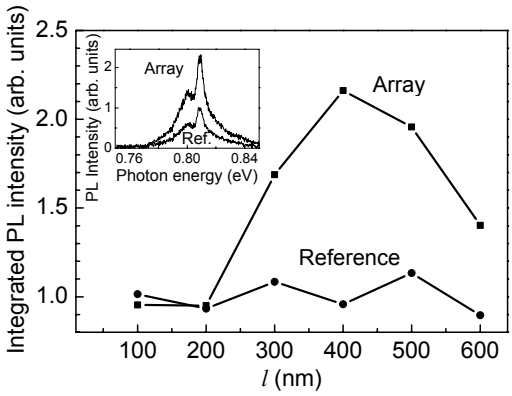

Figure 8.3: Integrated PL intensity at 1.54 μm as function of nanoparticle length l for 6 Ag nanoparticle arrays. Data measured both on the array and on the unpatterned reference area are shown. The inset shows two typical Er emission spectra. Pump wavelength: 532 nm.

tor in conjunction with a 30-cm-focal-length grating spectrograph. A dichroic filter was used to eliminate incident laser light from the detector. Reference PL spectra were obtained from areas close to the arrays where the Er implanted area was not covered with Ag nanoparticles.

Figure 8.3 shows the integrated Er PL intensity obtained at 1.54 μm for six arrays with increasing nanoparticle length l (l from 100 nm to 600 nm). In addition, the integrated PL intensity measured on nearby areas without nanoparticles is displayed as well. Two typical PL spectra for array and reference are shown in the inset. As can be seen in Fig. 8.3, the integrated PL intensities for array and reference are nearly identical for both $l \sim 100$ nm and $l \sim 200$ nm. Note that these data points correspond to the arrays for which the transmission in the Er emission band is practically unity (see Fig. 8.2). For longer nanoparticles, for which the low-energy transmission dip exhibits spectral overlap with the erbium emission band, the PL intensity on the array is enhanced compared to the reference area. The largest enhancement is observed for the nanoparticle length ($l \sim 400$ nm) for which the low-energy transmission dip has the best overlap with the Er emission band (see Fig. 8.2). Since this transmission dip is associated with the longitudinal plasmon mode, it can be concluded that the observed PL enhancement is due to the coupling of the Er^{3+} $^4I_{13/2} - ^4I_{15/2}$ transition dipoles with longitudinal plasmon modes in the nanoparticles. The close correspondence between array and reference measurements for both $l \sim 100$ nm and $l \sim 200$ nm, for which no plasmon mode is resonant with the emission, indicates that in the present configuration the measured PL intensity is not strongly affected by the potential difference

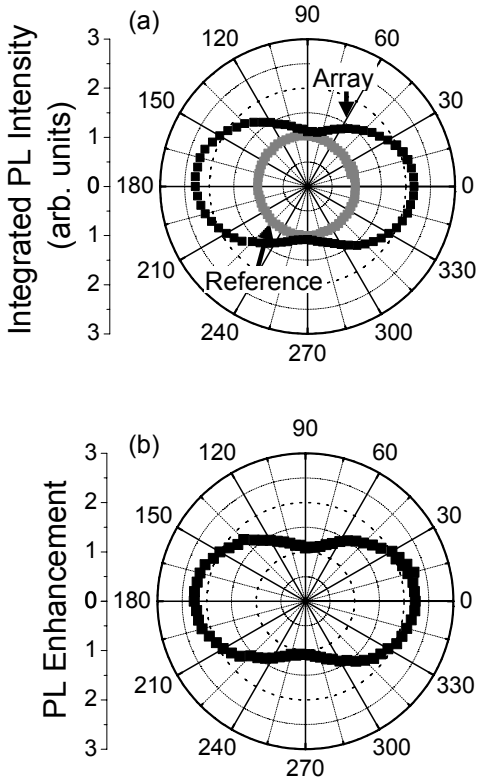

Figure 8.4: Polar plots of (a) the PL intensity for array ($l \sim 400$ nm) and reference and (b) the PL enhancement, both measured as function of the polarization angle θ of the emitted light relative to the long axis of the Ag nanoparticles. Pump wavelength: 532 nm.

in pump conditions between array and reference measurements.

8.3.2 Polarization characteristics

A second demonstration that the observed PL enhancement is due to the coupling of Er^{3+} ions with plasmon modes is given by polarization-dependent measurements of the PL intensity. These measurements were performed in the same configuration as was used to obtain the data shown in Fig. 8.3, except that the emitted light was passed through a polarization analyzer before illuminating the detector.

Figure 8.4(a) shows the PL intensity as function of the polarization angle θ

of the emitted light relative to the long axis of the nanoparticles (in the plane perpendicular to the surface normal) for $l \sim 400$ nm. The PL intensity on the unpatterned reference area is polarized isotropically (the circular pattern in the center of the plot), which implies that the PL intensity does not depend on the polarization of the pump light. The PL intensity on the array is clearly enhanced compared to the reference. Moreover, the enhancement is polarized in the direction of the long axis, which corresponds to the polarization direction of the nanoparticle plasmon mode that is resonant at 1.5 μm. This correspondence demonstrates that the observed PL enhancement is due to coupling of the Er^{3+} $^4I_{13/2} - ^4 I_{15/2}$ transition dipoles with plasmon modes in the metal nanoparticles.

It can be noted that the profiles in Fig. 8.4(a) are not completely symmetric for rotation over 180°. The asymmetry is attributed to a small misalignment in the setup. By normalizing the angular profile of the array by the reference data, perfectly symmetric curves are observed, as can be seen in Fig. 8.4(b). The two-fold PL enhancement observed is an ensemble average. Much larger local enhancement values are expected close to the sharp corners of the metal nanoparticles. Utilization of dense arrays of smaller nanoparticles is therefore expected to result in substantially larger ensemble-averaged enhancements. This issue is addressed in part IV of this thesis.

8.4 Conclusions

In conclusion, we have observed an enhancement of the photoluminescence intensity at 1.54 μm of optically active Er^{3+} ions in SiO_2 by coupling to engineered Ag nanoparticles. The PL enhancement is maximal if the Er emission is resonant with nanoparticle plasmon modes. Moreover, the PL enhancement is polarized corresponding to the polarization of the plasmon modes. Both these observations demonstrate that the Er^{3+} $^4I_{13/2} - ^4 I_{15/2}$ transition dipoles are coupled with nanoparticle plasmon modes. As this coupling mechanism is known to affect the emission rate, metal nanoparticles may reduce the significance of quench processes of Er embedded in various host materials, such as concentration quenching and upconversion in Er-doped dielectrics and temperature quenching of Er in Si.

Chapter 9

Absence of the enhanced intra-4f transition cross section at 1.5 μm of Er^{3+} in Si-rich oxide

We present measurements of the optical absorption cross section of the $^4I_{15/2} \rightarrow {}^4I_{13/2}$ transition at 1.5 μm of Er^{3+} ions embedded in SiO_2 and Si-rich oxide, using cavity ringdown spectroscopy on thin films. The peak absorption cross section for Er^{3+} embedded in Si-rich oxide (10 at.% excess Si) was found to be $(8 \pm 2) \times 10^{-21}$ cm^2 at 1536 nm, similar to typical values for Er embedded in SiO_2. The data imply that the silicon nanoclusters incorporated in Si-rich oxide do not enhance the peak cross section of the Er^{3+} $^4I_{15/2} - {}^4I_{13/2}$ transition by $1-2$ orders of magnitude, contrary to what has been reported in earlier work.

9.1 Introduction

In the previous chapters, the influence of metal nanoparticles on the properties of optical emitters was studied. In this chapter, we analyze the influence of silicon nanoclusters (i.e., dielectric inclusions) on the emission properties of erbium ions in silicon-rich oxide. Erbium-doped Si-rich oxide (SRO:Er) is an optical gain medium in which Er^{3+} ions, exhibiting an intra-4f transition at 1.5 μm, are surrounded by silicon nanoclusters that serve as broadband sensitizers [98–100]. A sensitizer coupled to an Er^{3+} ion absorbs light at a cross section several orders of magnitude larger than Er, and then transfers its energy to the Er^{3+} ion. Sensitizers could enable optical amplification at 1.5 μm using low-cost light-emitting diodes in top-pumping configuration, instead of a waveguide-coupled laser tuned to an Er transition.

In addition to the sensitization effect, which is of great technological interest, it has been reported that silicon nanoclusters would enhance the absorption and emission cross sections of the ${}^4I_{15/2} - {}^4I_{13/2}$ transition at 1.5 μm of Er^{3+} embedded in SiO_2 by $1-2$ orders of magnitude [101, 102]. This presumed enhancement was derived from optical absorption spectroscopy in linear waveguides [101], and it has been invoked to explain the high signal enhancement in SRO:Er linear amplifiers [102]. The enhanced emission cross section has also been used as an input parameter in a model describing the gain characteristics of SRO:Er amplifiers [103]. If true, the cross section enhancement would have a broad impact on Er amplifier and laser technology as it implies an enhancement of the optical gain coefficient by the same $1-2$ orders of magnitude. Thus more compact devices would be possible using SRO:Er.

Both reported cross-section enhancements are however based on indirect measurements, and a direct determination is still lacking. In this chapter, we present measurements of the Er^{3+} absorption cross section in both SRO:Er and SiO_2:Er by cavity ringdown spectroscopy (CRDS) on thin films [104, 105], which is an approach that does not require estimates on the overlap between an optical mode and the erbium profile as in earlier work. From the data it is concluded that the earlier reported $1-2$ orders of magnitude enhancement of the cross section of the Er^{3+} ${}^4I_{15/2} - {}^4I_{13/2}$ transition at 1.5 μm due to silicon nanoclusters is incorrect.

9.2 Experimental

SRO:Er and SiO_2:Er thin films were fabricated by ion implantation and thermal annealing of 2-mm-thick highpurity fused-silica substrates (Heraeus Suprasil 300). In the first fabrication step, the substrates were implanted with 300-keV and 150-keV Er ions to a total fluence of 1.2×10^{16} at/cm^2. The Er peak concentration measured by Rutherford backscattering spectrometry was 2.3 at.%. Subsequently, a dual Si implant (73 and 30 keV) was applied to part

of the Er-implanted samples to fabricate SRO:Er films. The Si fluences were chosen such that an excess Si concentration of ∼10 at.% was achieved over the full Er depth profile. One of the SRO:Er samples was annealed at 800 °C for 30 minutes in flowing Ar and at 700 °C for 30 minutes in forming gas (H_2:N_2 at 1:9) to optimize the Er^{3+} 1.5 μm photoluminescence (PL) intensity [106]. An SiO_2:Er reference sample (i.e., no Si implanted) was exposed to the same thermal treatment. A second SRO:Er sample was annealed at 1000 °C for 30 minutes in flowing Ar, comparable to the thermal treatments described in Refs. [101] and [102]. PL excitation spectroscopy using different lines of an Ar^+ laser showed that Er^{3+} embedded in SRO was mainly excited indirectly, confirming the coupling between Er^{3+} and silicon nanoclusters in these samples.

The Er^{3+} absorption spectrum at 1.5 μm was determined by cavity ringdown spectroscopy (CRDS) on thin films, which is a direct and highly sensitive absorption measurement method in which the sample under investigation is placed inside a high-quality optical cavity, see the inset of Fig. 9.1 [104, 105]. The measurements were carried out with the tunable idler output of an optical parametric oscillator (OPO), which is pumped by the third harmonic of a pulsed Nd:YAG laser operating at 30 Hz. The idler output of the OPO was tuned over the wavelength range of $1450 - 1630$ nm with an accuracy of 2 nm, and the resulting pulse had a typical bandwidth of 2 nm, a duration of 5 ns, and a pulse energy of 10 mJ. The pulse was injected into a stable optical cavity (length 0.4 m) formed by two planoconcave highly reflecting ($R > 0.9997$) mirrors without using mode-matching optics, resulting in an effective spot size of 3 mm. Thus, the total injected pulse energy was less than 3 μJ. The cavity was purged with dry nitrogen to reduce the effects of H_2O absorption lines. The temporal decrease in light intensity inside the cavity upon pulse injection was detected with a photodiode. Individual transients were sampled using a 12-bit, 100-MHz data acquisition system.

9.3 Results

Figure 9.1 shows cavity ringdown transients detected at 1536 nm for both an SRO:Er sample that was annealed at 800 °C and a bare silica substrate. After the first microsecond, the transients exhibit a single-exponential behavior of which the rate is determined by the intrinsic cavity loss and the loss generated by the sample placed in the cavity [104]. The ringdown time for SRO:Er (3 μs) is significantly shorter than for silica (8 μs) due to the stronger extinction of the SRO:Er sample. The single-exponential parts of individual transients were fitted with a standard weighted linear regression technique to extract the ringdown time. Reported values of the optical loss per pass, which includes both scattering and absorption contributions, have been corrected for the empty cavity response and were deduced from averages of the ringdown time over 100 laser shots at every wavelength.

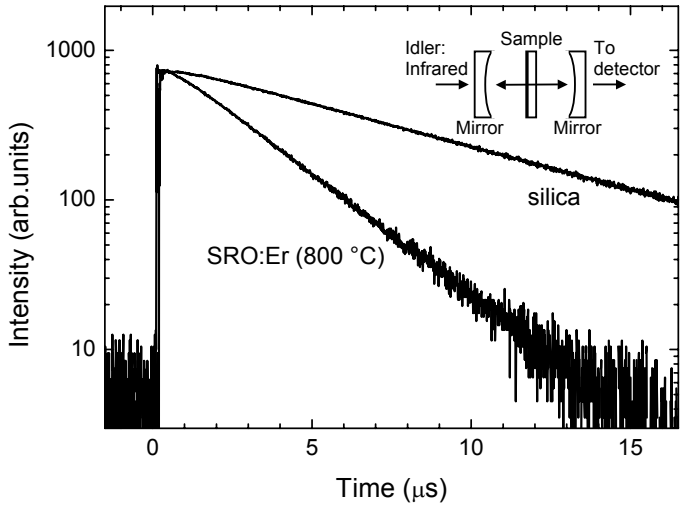

Figure 9.1: Cavity ringdown transients for both an SRO:Er sample and a bare silica substrate detected at 1536 nm upon injection of a 5-ns pulse at $t = 0$. The experimental configuration is sketched in the inset.

Figure 9.2 shows the optical loss spectra for SRO:Er and SiO_2:Er determined in this way. Every optical loss spectrum shows a characteristic Er^{3+} absorption spectrum superimposed on a background that is decreasing with wavelength, which is attributed to loss processes not related to Er, such as scattering. Repeated measurements after sample realignment gave reproducible results for both peak shape and magnitude, as well as for the decreasing background trend, with some variations in background level. We attribute the latter to variations in both alignment and sample quality.

The estimates of the background losses indicated in Fig. 9.2 (dashed lines) are based on a qualitative comparison with absorption spectra derived by PL spectroscopy using McCumber theory [107, 108], as is illustrated in Fig. 9.3. Figure 9.3(a) shows a PL spectrum for SRO:Er (annealed at 800 °C) taken at room temperature. The absorption spectral shape derived from this spectrum is shown in Fig. 9.3(b), together with the corresponding absorption spectrum derived from the optical loss data shown in Fig. 9.2 by subtraction of the background loss (dashed line). The spectral resemblance between the CRDS-based spectrum and the normalized PL-based spectrum validates the estimate of the background loss. The important feature shown in Fig. 9.2 is that, for all three samples, the Er absorption is very similar over the entire wavelength range (within 20%). The Er^{3+} $^4I_{15/2} \rightarrow {}^4I_{13/2}$ absorption cross section is thus found to be similar for SiO_2:Er and SRO:Er annealed at either 800 or

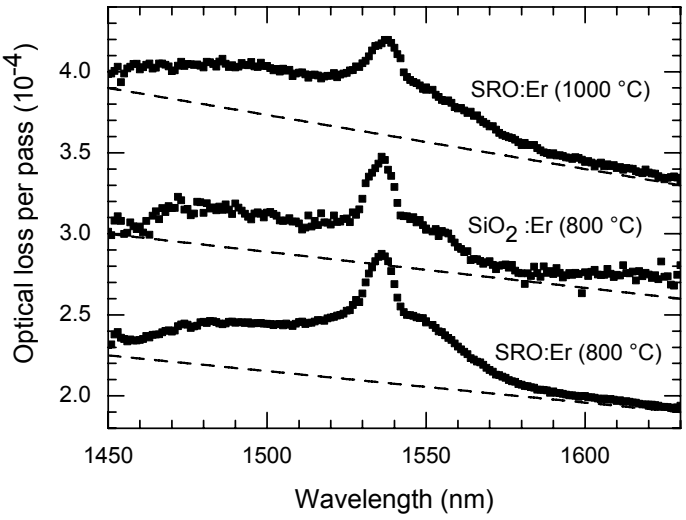

Figure 9.2: Optical loss spectra for SRO:Er (annealed at 800 °C and 1000 °C) and SiO_2:Er (annealed at 800 °C) measured by cavity ringdown spectroscopy (CRDS) on thin films. All spectra have been corrected for the empty cavity response. Estimates of the background loss are indicated for all spectra (dashed lines)

1000 °C. Here, it is assumed that all Er ions are in the 3+ valence state, which is justified by the fact that no other valences of Er are reported for a variety of hosts [109]. In addition, X-ray absorption spectroscopy of the Er $3d^{10}4f^{11} \rightarrow 3d^{9}4f^{12}$ transitions for Er-doped silicon has shown no evidence of other Er valence states [110]. The Er^{3+} $^4I_{15/2} \rightarrow {}^4I_{13/2}$ absorption cross section for SRO:Er can directly be obtained from Fig. 9.3(b) by dividing the Er absorption by the Er areal density. This procedure yields a peak absorption cross section, which is related to the maximum gain coefficient for SRO:Er amplifiers, of $(8 \pm 2) \times 10^{-21}\mathrm{cm}^2$ at 1536 nm, where the error bar is determined mainly by the uncertainty in the background level of the absorption measured. This result is similar to typical values obtained for Er embedded in glasses [111]: $(4.8-7.0) \times 10^{-21}$ cm^2, confirming that silicon nanoclusters do not enhance the cross section of the Er^{3+} $^4I_{15/2} - {}^4I_{13/2}$ transition by $1-2$ orders of magnitude. Note that the cross section in SRO:Er is expected to be $10-20\%$ larger than in SiO_2:Er due to the higher refractive index of the heterogeneous SRO [95], but the limited signal-to-noise ratio of the SiO_2:Er sample does not allow one to resolve this difference from the performed measurements.

For the determination of the Er^{3+} $^4I_{15/2} \rightarrow {}^4I_{13/2}$ absorption cross section, bleaching of the Er^{3+} ions has been neglected. This is legitimate since the

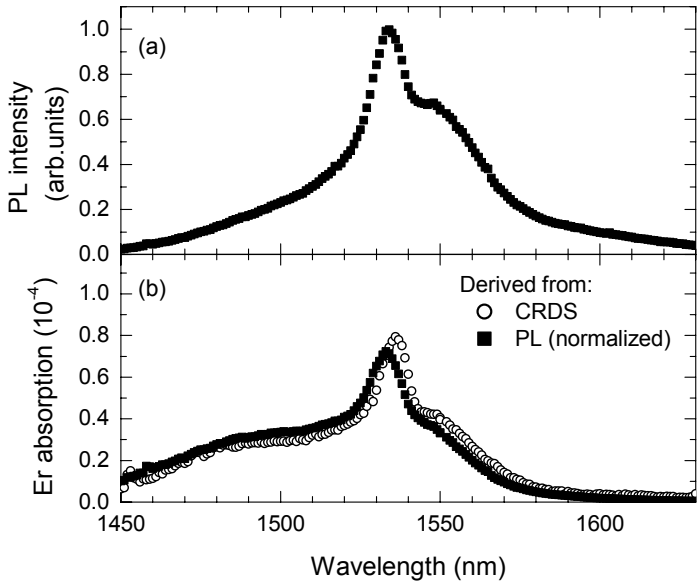

Figure 9.3: (a) PL spectrum of SRO:Er (annealed at 800 °C) measured at room temperature under 488 nm excitation. (b) Er absorption spectra derived both from the optical loss spectrum, by a subtraction of the background (◯), and from the PL spectrum by means of McCumber theory (■).

effective pump power inside the cavity was adequately low, as can be derived in the following way. Upon pulse injection, the pulse energy in the cavity was lower than 3 μJ. Taking into account the cavity length, ringdown time, and laser spot size, this corresponds to an effective time-integrated photon flux of 6×10^{17} photons/cm^2 per pulse. This implies that for an Er^{3+} absorption cross section of 8×10^{-21} cm^2 less than 0.5% of the Er^{3+} population was inverted per pulse. Subsequent pulses can be regarded independently, since the interval between them (33 ms) is much larger than the Er^{3+} lifetime in our samples (3 ms). The relatively short Er^{3+} lifetime is ascribed to the presence of nonradiative de-excitation channels in the heavily doped matrix. If the cross section had been 2×10^{-19} cm^2, still only 12% of the Er^{3+} population would have been inverted, and the Er absorption peak would be 20 times larger than observed. This implies that the error in the absorption cross section induced by Er^{3+} bleaching is much smaller than the error induced by the uncertainty in the background level.

Finally, we speculate on the apparent discrepancy between the cross section for SRO:Er derived here, and the much larger values claimed in earlier work.

Kik's tenfold enhanced cross-section claim [101] was based on a calculation that involved an estimated overlap between the optical waveguide mode and the Er profile. Possibly, this overlap was underestimated. As CRDS does not require estimates on modal overlap in order to determine the absorption cross section, the method presented in the current work provides more reliable results. The reported near-hundredfold cross section enhancement derived from gain characteristics of SRO:Er linear amplifiers by Han et al. [102] remains puzzling. In any case, such an enhancement is inconsistent with the Er luminescence lifetime of 8 ms reported in the same paper: according to the Füchtbauer-Ladenburg equation [108], the reported Er emission cross section of $(2 \pm 0.5) \times 10^{-19}$ cm^2 would correspond to a radiative lifetime of $\sim$0.3 ms.

9.4 Conclusions

In conclusion, we have measured the optical absorption cross section of the Er^{3+} $^4I_{15/2}$ $-$ $^4I_{13/2}$ transition at 1.5 μm in both SRO:Er and SiO_2:Er by cavity ringdown spectroscopy on thin films, proving that this is a suitable technique for the determination of rare-earth absorption cross sections. The peak absorption cross section for SRO:Er was found to be $(8 \pm 2) \times 10^{-21}$ cm^2, which is identical (within 20%) to the measured cross section for SiO_2:Er, and which is a typical value for Er embedded in glasses. This result is in disagreement with earlier reported cross sections enhancements for SRO:Er. The conclusion affects modeling of the gain characteristics of SRO:Er materials that use the presumed enhanced cross section as an input parameter [103].

Part IV

Modeling of plasmon-enhanced luminescence

Chapter 10

Exact electrodynamical theory versus an improved Gersten and Nitzan model

We present a theoretical study of the modifications of the radiative and non-radiative decay rates of an optical emitter in close proximity to a noble-metal nanosphere, based on exact electrodynamical theory. We show that the optimal nanosphere diameter for luminescence quantum efficiency enhancement associated with resonant coupling to plasmon modes is in the range $30 - 110$ nm, depending on the material properties. The optimal diameter is found to be a trade-off between (1) emitter-plasmon coupling, which is most effective for small spheres, and (2) the outcoupling of plasmons into radiation, which is most efficient for large spheres. In addition, we show that the well-known Gersten and Nitzan model does not describe the existence of a finite optimal diameter unless the model is extended with the correction factor for radiation damping. With this correction and a correction for dynamic depolarization, the Gersten and Nitzan model, which can be generalized to spheroids much more easily than exact electrodynamical theory, is found to provide a reasonably accurate approximation of the decay rate modifications associated with coupling to the dipole plasmon mode. We anticipate that the Gersten and Nitzan model in the form that we validate in this chapter for spheres will allow the investigation of the influence of particle anisotropy on plasmon-enhanced luminescence in an analytical way.

10.1 Introduction

During the last decade, there has been a strong revival in experimental efforts to control spontaneous emission dynamics by metal nanostructures [22–27]. In particular the recent advancements in nano-optics, which allow for experiments on single molecules interacting with well-defined metal nanostructures, often referred to as nano-antennas [28, 29], serve as a strong impetus for this development. These single-molecule experiments, which focus on the resonant coupling of emitters with plasmon modes, i.e., collective conduction electron oscillations in the metal, have led to the observation of photoluminescence enhancement and quenching depending on the distance between emitter and metal [22], with concomitant changes in excited state lifetime [23, 24].

In addition to these fundamental breakthroughs, the recent progress in nanotechnology enables the introduction of plasmon-enhanced luminescence in various applications, e.g. for enhancing the brightness of technologically important light emitters [73, 112], or for enhancing emission in a polarization-selective way [96]. Besides, plasmon-enhanced luminescence has great potential for sensing applications [113] and for improving the light-harvesting capabilities of solar cells [114].

With the ongoing interest in the electromagnetic interaction between emitters and metal nanostructures, both from a fundamental and an applications point of view, there is a growing demand for theoretical studies that provide insight in the physical factors that determine the performance of nano-antenna geometries [70, 115–119]. The need for such investigations is emphasized by the fact that, due to both the absorptive nature of metals and the high confinement of plasmonic modes, only in a limited part of the extensive parameter space, metal nanostructures can provide exceptional improvements to the radiative properties of optical emitters.

In this chapter, we present an extensive survey, based on an exact electrodynamical theory [21, 120, 121], of the modifications of the radiative and nonradiative decay rates of an emitter in close proximity to a metal sphere. We focus on the enhancement of the luminescence quantum efficiency of a low-quantum-efficiency emitter by resonant coupling to the plasmon modes of the sphere. We explain the dependencies of the quantum efficiency on emitter-metal separation and on sphere size based on the scattering and absorption properties of the plasmon modes of the sphere. This approach provides physical insight in the extent to which radiative and nonradiative decay rate enhancements are intrinsically linked, or can be separated by design. By comparing results for Ag and Au to the results for an ideal Drude metal, we also determine which of the observed trends are intrinsic to a free-electron response, and which are related to interband transitions in the metals. Furthermore, we address the strong influence of dipole emitter orientation relative to the sphere on plasmon-enhanced luminescence.

In the second part of this chapter, we compare the decay rate modifications

calculated from exact electrodynamical theory with the results obtained from the model by Gersten and Nitzan (GN) [19, 122]: a quasistatic model in which retardation effects are treated as perturbations. The advantage of the GN model is that it can be generalized to spheroids based on an expansion in terms of an orthogonal set of eigenfunctions. Such an expansion is not known for exact electrodynamical theory [123]. The goal of our comparison is to verify the accuracy of the GN model for the particle sizes of interest. In this chapter, we have improved the GN model to account for radiation damping [20] and dynamic depolarization [124] according to Wokaun et al. We demonstrate that the improved GN model can be applied over a substantially larger particle-size range than the original version [125]. In particular, we show that the improved GN model, in contrast to the original version, does describe the existence of a finite optimal diameter for plasmon-enhanced luminescence, which is consistent with the exact electrodynamical theory.

The chapter is organized as follows. In section 10.2 we summarize the two theoretical approaches that we adopt. In section 10.3 we discuss the influence of the separation between a low-quantum-efficiency emitter and a Ag sphere on the radiative and nonradiative decay rates, and thus on the quantum efficiency, of the emitter. In section 10.4 we focus on the dependence of the quantum efficiency enhancement on the sphere size. In section 10.5, we compare the exact electrodynamical theory to both the original and the improved GN models. Finally, conclusions are presented in section 10.6.

10.2 Methods

The modification of spontaneous emission is a phenomenon that can be described classically [15, 126]. The excited state decay rate, which in the presence of absorbing dielectrics consists of radiative and nonradiative components, is proportional to the work $W = \boldsymbol{\mu} \cdot \mathbf{E}$ that the field $\mathbf{E}$ generated by the current source $\mathbf{j}(\mathbf{r}, t)$ does on the source itself [16, 17].

In the first calculation method, we use this concept to analyze decay rate modifications induced by a metal sphere at short distance. These modifications are calculated analytically using exact electrodynamical theory in the following way [21, 120]. The excited state decay rate in the presence of a metal sphere, normalized to the rate in a bulk dielectric, is obtained by comparing the work W done on a source in the presence of the sphere to the work W_0 done on the same current source in the bulk dielectric. The analytical expressions for this rate, which can be derived from the Green function [121] for a dielectric sphere, are given in the Appendix. The modification of the radiative decay rate is found by comparing the energy flux through a surface that encloses both source and sphere to the radiated power of the same source dipole in the bulk dielectric (see Appendix). Subsequently, the component of the nonradiative decay rate that is associated with dissipation in the absorbing sphere is obtained by taking

the difference between the excited state decay rate and the radiative decay rate. Note that the nonradiative decay rate, and thus also the excited state decay rate, of a luminescent species may contain additional components, e.g., due to Auger processes, that are not described by the local electromagnetic theory. Within the context of the exact electrodynamical theory, also the angular emission distribution of a source dipole in proximity to a metal sphere is analyzed. Such distributions are calculated from an expansion of the electric dyadic Green function in terms of vector spherical harmonics [121].

In the Gersten and Nitzan (GN) model [19, 122], which is the second calculation method that we adopt, the modifications of the radiative and nonradiative decay rates are calculated in a two-step approach. In the first step, the electromagnetic interaction between source dipole and sphere is analyzed using the quasistatic approximation [47]. In this approximation it is assumed that all dimensions are much smaller than the wavelength of light, so that retardation can be neglected in the description of the coupling. The analysis can then be based on electrostatics. The solution for the electrostatic potential is a superposition of the source dipole potential and the induced multipoles of the sphere [122]. Note that for particles that are much smaller than the wavelength, a dipole source at short distance induces higher-order multipoles as well, because of the strong gradients in the near field of the source. This is different for plane-wave illumination of such particles, which only can excite dipole modes. In the second step, an effective dipole moment of the coupled system is identified. This effective dipole moment, which comprises a vectorial superposition of the source dipole moment and the induced dipole moment, is used to calculate the radiated power. By normalization to the power radiated by an uncoupled source with identical dipole moment, the modification of the radiative decay rate is obtained. The nonradiative decay rate due to coupling with the absorbing sphere is determined by calculating the power that is dissipated in the sphere using the Joule heating law [127]. Since the electric field in the sphere is a superposition of all multipole modes, all these modes contribute to the nonradiative decay rate, whereas only the dipole mode is assumed to affect the radiative decay rate. This assumption is not made in the approach that relies on the exact electrodynamical theory. In section 10.4, it is discussed for what metal sphere sizes the assumption is justified. We find that under particular conditions higher-order modes can enhance the radiative decay rate as well.

We have modified the first step of the GN model by taking into account that the magnitude of the induced dipole moment is not only limited by absorption losses, as is implicitly assumed in the quasistatic approximation, but also by radiation losses [20]. Besides, the redshift of the dipole plasmon resonance caused by retardation of the depolarization field due to the finite dimensions of the sphere, referred to as dynamic depolarization [124], is implemented as well. Both these corrections to the original GN model are taken into account by an effective nanoparticle polarizability that differs from the electrostatic polariza-

bility by a correction factor [128]. With this correction factor, which in Ref. [124] is derived from a self-consistent calculation of the particle polarization, the expression for the quasistatic scattering coefficient of a sphere corresponds closely to a power-series expansion of the Mie scattering coefficient until the third order in size parameter. Neither of these two corrections has been taken into account in a previous comparison of the GN model and the exact electrodynamical theory [125], although the first correction is essential for satisfying the optical theorem, i.e., energy conservation in electromagnetic fields.

10.3 Decay rate modifications versus emitter-sphere separation

We consider the modifications of the radiative decay rate Γ_R, the nonradiative decay rate Γ_{NR}, and the quantum efficiency $\eta = \Gamma_R/(\Gamma_R + \Gamma_{NR})$ of an emitter that is embedded in a homogeneous dielectric with a refractive index of 1.3 and which has an internal luminescence quantum efficiency of 1% in the absence of the sphere. The choice for the relatively low quantum efficiency is motivated by the fact that it enables the illustration of some important aspects associated with the coupling of an emitter to the plasmon modes of a metal sphere. In this section, the emitter is positioned near a Ag sphere with a diameter of 60 nm. The optical data of Ag are taken from Palik [42], and the source dipole orientation is averaged over all solid angles (see the Appendix), which is representative for experiments on collections of atoms with randomly oriented transition dipole moments. The influence of specific dipole orientations on the decay rate enhancements will be discussed later. The emission wavelength (λ_{em} = 433 nm) is chosen such that the emission is resonant with the dipole plasmon mode of the sphere. All results in this section were calculated from the exact electrodynamical theory, as described in section 10.2.

Figure 10.1(a) shows the radiative decay rate, normalized to the radiative decay rate in the absence of the sphere, as a function of the distance to the sphere surface (solid line). At a distance of 0 nm, the radiative decay rate is 50 times larger than in the absence of the sphere, and it drops off to a factor of 2 in about 30 nm. The radiative decay rate is composed of two contributions: the radiative decay rate of the emitter in the absence of the sphere (dotted line) and the contribution due to presence of the sphere (dashed line), which can be fully attributed to coupling to the dipole mode. In section 10.4, it is described for which parameters higher-order modes have substantial impact on the radiative decay rate as well. An explanation of the decomposition of the decay rates into various contributions can be found in the Appendix.

Figure 10.1(b) shows a similar plot for the nonradiative decay rate. The solid line represents the total nonradiative decay rate, which is composed of two types of contributions. The dotted line is the sphere-independent contribution, which is 99 times larger than its radiative counterpart because of the choice

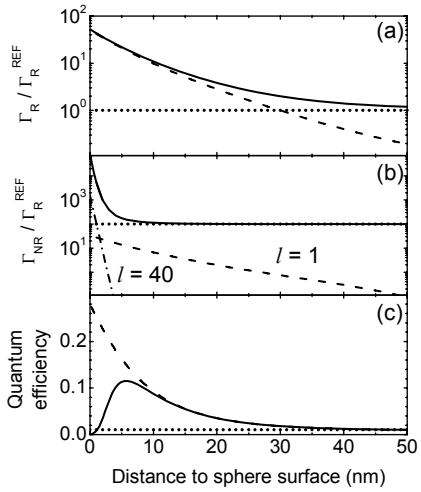

Figure 10.1: (a) Radiative decay rate of a dipole emitter, the orientation of which is averaged over all solid angles, versus the distance to the surface of a 60-nm-diameter Ag sphere (solid line), the contribution to the radiative decay rate due to coupling with the dipole plasmon mode (dashed line), and the radiative decay rate in the absence of the sphere (dotted line). (b) Nonradiative decay rate versus distance to the sphere surface when taking into account coupling to all modes up to $l = 60$ (solid line), the contributions to the nonradiative decay rate due to the $l = 1$ or dipole mode (dashed line) and due to the $l = 40$ mode (dash-dotted line), and the nonradiative decay rate in the absence of the sphere (dotted line). The decay rates in both (a) and (b) are normalized to the radiative decay rate in the absence of the sphere. (c) Luminescence quantum efficiency versus distance to the sphere surface when taking into account coupling to all modes up to $l = 60$ (solid line) and when taking into account coupling to the dipole plasmon mode only (dashed line), and the quantum efficiency in the absence of the sphere (dotted line). Emission wavelength: 433 nm. Calculation method: exact electrodynamical theory.

for a quantum efficiency of 1% in the absence of the sphere. The dashed lines are contributions due to coupling to two representative plasmon modes with different angular mode numbers l: $l = 1$ (dipole) and $l = 40$. The $l = 1$ mode contributes to the nonradiative decay rate at relatively large distances, whereas the $l = 40$ mode is only significant at very small distances. In the calculation of the total nonradiative decay rate (solid line), coupling to all plasmon modes up to $l = 60$ was taken into account. Including such higher-order modes is required to achieve convergence at separations down to 1 nm.

Figure 10.1(c) shows the quantum efficiency η as a function of emitter-nanoparticle separation. The dashed line shows the behavior if only coupling

to the dipole mode is taken into account. The trend is a monotonic increase in quantum efficiency upon decreasing the emitter-nanoparticle separation. If all modes up to $l = 60$ are taken into account (solid line), a similar trend is found down to a separation of 10 nm, but a strong decrease is observed when the separation is reduced further. Despite the fact that the higher order plasmon modes are centered at different frequencies than the dipole mode (as will be shown later on), their collective influence at the dipole resonance frequency is still large enough to cause the reduction in quantum efficiency. This result demonstrates that quenching at short distances follows simply from coupling to higher order plasmon modes. Because these modes do not efficiently couple to the far-field, they can be considered as dark modes [129]. Coupling to these modes hence always reduces the quantum efficiency. We conclude that the quenching at short emitter-metal separations can be described without invoking electron-electron interactions between emitter and metal.

More quantitatively, Figure 10.1(c) shows that, at separations of 5 to 10 nm, the quantum efficiency is enhanced by an order of magnitude. At a separation of 6 nm, this quantum efficiency enhancement is the combined effect of 19-fold radiative decay rate enhancement and a 1.5-fold nonradiative decay rate enhancement. Obviously, the nonradiative decay rate enhancement depends strongly on the specific choice of the quantum efficiency in the absence of the sphere.

Note that the modification of the quantum efficiency enhancement, which we have focused on in this section, is not only a measure for the redistribution of energy in radiative and nonradiative decay channels, but also a measure for the increase in photoluminescence intensity due to decay rate modifications for experiments performed in the linear pump power regime. Note also that we do not consider enhancements of the optical excitation rate, as we focus on processes that could be utilized in light sources that rely on electrical excitation as well.

10.4 Quantum efficiency enhancement versus sphere diameter

10.4.1 Optimum size for quantum efficiency enhancement

The magnitude of the quantum efficiency enhancement due to resonant coupling to plasmon modes depends strongly on sphere diameter. This is illustrated in Figure 10.2, which shows the quantum efficiency of a dipole emitter, the orientation of which is averaged over all solid angles, as a function of the distance to a Ag sphere, for three sphere diameters: 10 nm, 60 nm, and 140 nm. The emitter, which is embedded in a dielectric with a refractive index of 1.3, is assumed to have a quantum efficiency of 1% in the absence of the sphere. The emission wavelength is adjusted for every diameter in order to match the size-dependent

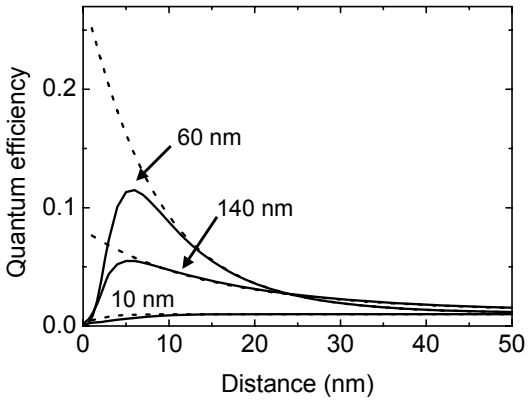

Figure 10.2: Quantum efficiency of a dipole emitter, the orientation of which is averaged over all solid angles, versus distance to the surface of a Ag sphere for three sphere diameters: 10 nm, 60 nm, and 140 nm, when taking into account coupling to all modes up to $l = 80$ (solid lines) and when taking into account coupling to the dipole mode only (dashed lines). The refractive index of the embedding medium is 1.3, and the quantum efficiency of the emitter in the absence of the sphere is 1%. The calculations were done at the wavelength of maximum radiative decay rate enhancement for each diameter. Calculation method: exact electrodynamical theory.

dipole resonance wavelength: 397 nm, 433 nm, and 683 nm, for diameters of 10 nm, 60 nm and 140 nm, respectively. For all three diameters, two curves are plotted: one for which only coupling to the dipole mode is taken into account (dashed lines), and one for which coupling to all modes up to $l = 80$ is taken into account (solid lines). As in the previous section, the results were calculated from the exact electrodynamical theory, as described in section 10.2.

Figure 10.2 shows that the highest quantum efficiency enhancement is found for the intermediate diameter (60 nm). By comparing the solid and dashed lines in the figure, it can be concluded that the size dependence of the maximum quantum efficiency enhancement is due to the electromagnetic properties of the radiative dipole mode only, and that it does not relate to the dark higher-order modes, which are responsible for the drop in quantum efficiency at short distances. A more detailed description of the sphere-size dependence of the quantum efficiency enhancement as well as of its interpretation in terms of the properties of the dipole plasmon mode follows hereafter.

Figure 10.3(a) displays the wavelength of maximum radiative decay rate enhancement associated with coupling to the dipole mode versus sphere diameter for a dipole emitter, the orientation of which is averaged over all solid angles, embedded in a dielectric with a refractive index of 1.3, for three sphere

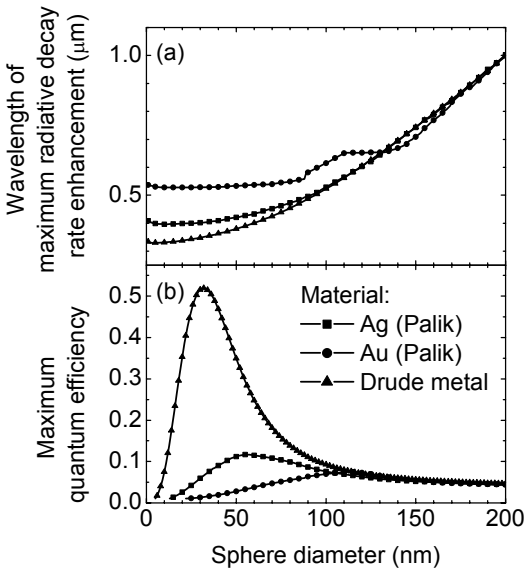

Figure 10.3: (a) Wavelength of maximum radiative decay rate enhancement associated with coupling to the dipole plasmon mode versus sphere diameter for a dipole emitter, the orientation of which is averaged over all solid angles, positioned in close proximity to a sphere, plotted for three sphere materials: Ag, Au, and a Drude-model fit for Ag. (b) Maximum quantum efficiency versus sphere diameter at the wavelength shown in (a), for the same three materials. The refractive index of the embedding medium is 1.3, and the quantum efficiency of the emitter in the absence of the sphere is 1%. Calculation method: exact electrodynamical theory.

materials: Ag, Au, and a Drude metal. The optical data for Ag and Au were taken from Ref. [42] and are shown in Fig. 10.4. The parameters for the Drude metal, i.e., plasma frequency (1.2×10^{16} rad/s) and electron relaxation frequency (9×10^{13} rad/s), were obtained from a fit to the data for Ag in the infrared part of the spectrum, where the Drude model provides an accurate description of the electromagnetic response of Ag. Figure 10.3(a) shows a redshift of the wavelength of maximum radiative decay rate enhancement with increasing diameter for all three materials. This redshift is directly related to the dipole resonance redshift for increasing size, which is mainly attributed to retardation of the depolarization field across the sphere diameter [124]. We note that the wavelength of maximum radiative decay rate enhancement is independent of emitter-sphere separation.

Figure 10.3(b) shows the maximum quantum efficiency calculated at the

wavelength shown in Fig. 10.3(a), also taking into account coupling to higher order modes (see the Appendix). The wavelength is not fixed because we intend to investigate the size dependence of the luminescence enhancement associated with coupling to the dipole plasmon resonance that shifts with size. The maximum quantum efficiency refers to the maximum values in quantum-efficiency-versus-distance plots, as are shown in Fig. 10.2, and thus represent different (optimized) emitter-sphere separations, ranging from $3-10$ nm. The data are calculated for an emitter that has a quantum efficiency of 1% in the absence of the sphere, and for a dipole orientation that is averaged over all solid angles. Figure 10.3(b) illustrates that for all three materials an optimal diameter for quantum efficiency enhancement can be identified. That this is also possible for the Drude metal implies that the existence of such an optimal diameter can be described based on a purely free-electron response for the metal.

Despite the qualitative correspondence between the three curves of Fig. 10.3(b), large numerical differences are found for the three materials. The optimal diameter is 30 nm for the Drude metal, 55 nm for Ag, and 110 nm for Au. Moreover, the maximum quantum efficiency is 52% for the Drude metal, 11% for Ag, and only 7% for Au. These differences are related to the fact that the imaginary part of the dielectric functions of Ag and Au are much higher than that of an ideal Drude metal, as is clearly visible in Fig. 10.4, for wavelengths below 600 nm. The difference is due to interband transitions [4]. Figure 10.4(b) illustrates that the Drude model fits the real part of the dielectric functions of both Ag and Au reasonably well over the spectral range >600 nm. It can be concluded from Figures 10.3 and 10.4 that for plasmon-enhanced luminescence at wavelengths below ∼600 nm, Ag is more suitable than Au due to the smaller contributions of interband transitions to the imaginary part of the dielectric function.

In order to explain the origin of the optimal sphere diameter for quantum efficiency enhancement, as shown in Fig. 10.3(b), Figure 10.5 illustrates the sphere-diameter dependencies of the two processes that determine the quantum efficiency enhancement. We consider the same parameters as were used in Fig. 10.3, and we limit ourselves to Ag. Figure 10.5(a) displays the contribution of the total excited state decay rate that is associated with coupling to the dipole plasmon mode $\Gamma_{TOT,DIP}$ versus sphere diameter (see the Appendix for an explanation on how this dipole contribution is determined). The decay rate increases in magnitude for decreasing diameter. This trend is qualitatively comparable to the mode-volume dependence of the emission rate enhancement of an atom that is coupled to an optical microcavity mode in the weak coupling regime. Within that context, emission rate enhancements are often described using the Purcell factor, which is inversely proportional to the mode volume [130]. A detailed analysis of the correspondence between decay rate modifications near a metal sphere and the Purcell factor (as e.g. in Ref. [131]) is beyond the scope of this thesis.

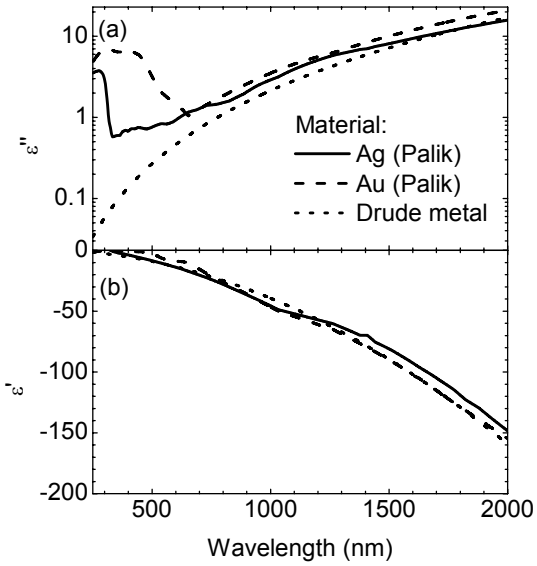

Figure 10.4: (a) Imaginary part, plotted on a logarithmic scale, and (b) real part, plotted on a linear scale, of the dielectric functions of the three sphere materials used in the calculations.

Figure 10.5(b) shows the fraction of the total power coupled to the dipole mode that is reradiated, denoted as F (line with symbols). This quantity, which is identical to the ratio of the dipolar components of the scattering and extinction cross sections, increases with diameter. Below a diameter of ∼30 nm, F equals the albedo of a spherical Rayleigh scatterer (dashed line), which is proportional to diameter cubed. Above ∼30 nm F flattens off due to retardation effects.

Since quantum efficiency enhancement involves both effective coupling of the emitter to the plasmon mode, and efficient outcoupling of plasmons into radiation, the opposite dependencies on sphere diameter shown in Figs. 10.5(a) and (b) give rise to a trade-off. This explains the origin of the optimal diameter for quantum efficiency enhancement.

10.4.2 Higher-order mode contributions to the emission enhancement

At wavelengths above ∼600 nm, where interband transitions are insignificant for both Ag and Au, resonant plasmon modes can be obtained by increasing the particle size, as shown in Fig. 10.3(a). However, plasmon-enhanced lumi-

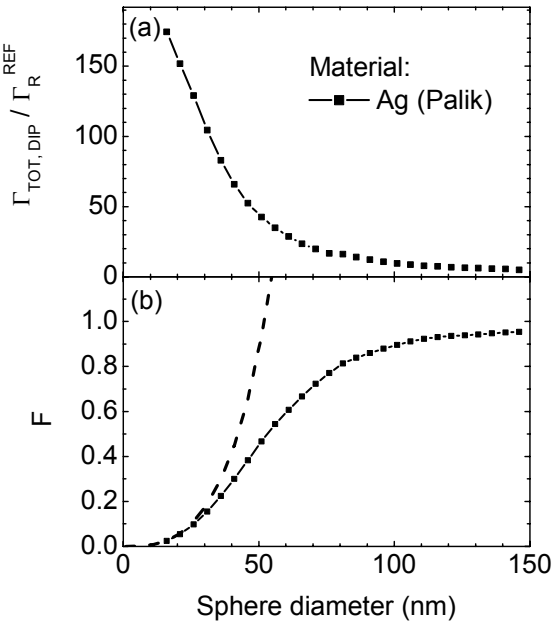

Figure 10.5: (a) Contribution to the total excited state decay rate that is associated with coupling to the dipole plasmon mode of the Ag sphere $\Gamma_{TOT,DIP}$, normalized to the radiative decay rate in the absence of the sphere , versus sphere diameter. (b) Fraction of the energy coupled to the dipole plasmon mode that is reradiated F (line with symbols). The dashed line represents the albedo of the sphere according to the quasistatic theory. The data represented as lines with symbols are calculated from the exact electrodynamical theory. The parameters are the same as for Fig. 10.3.

nescence is less effective for larger particles (see Fig. 10.3(b)). An alternative strategy to achieve resonantly enhanced luminescence at larger wavelengths, but with small particles, is to use anisotropic particles, with redshifted longitudinal resonances [36], to use arrays of coupled particles [132], or by increasing the refractive index of the embedding medium [34].

Figure 10.6 illustrates the effect of a high-index embedding medium ($n = 3.5$) on the quantum efficiency enhancement associated with coupling to the dipole mode of a sphere. Figure 10.6(a) shows that the higher refractive index causes a strong increase of the wavelength of maximum radiative decay rate enhancement (closed symbols) compared to the data shown in Fig. 10.3(a) for $n = 1.3$. Resonance wavelengths as large as 2.0 μm are observed for 150-nm diameter particles.

Figure 10.6(b) shows the maximum quantum efficiency calculated at the

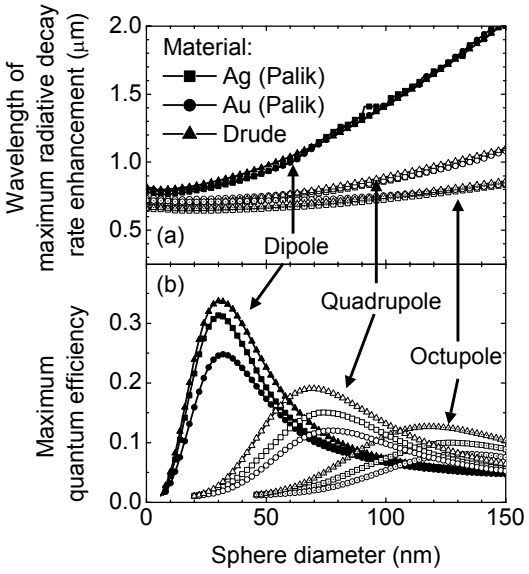

Figure 10.6: Calculations for a dipole emitter, the orientation of which is averaged over all solid angles, positioned in close proximity to a metal sphere (see text), embedded in a medium with a refractive index of 3.5. (a) Wavelength of maximum radiative decay rate enhancement due to coupling to either the dipole mode (closed symbols), the quadrupole mode (open symbols) or the octupole mode (open symbols with dots) versus sphere diameter, plotted for three sphere materials: Ag, Au, and a Drude-model fit for Ag. (b) Maximum quantum efficiency versus sphere diameter at the wavelengths shown in (a) for the same three materials. The quantum efficiency of the emitter in the absence of the sphere is 1%. Calculation method: exact electrodynamical theory.

wavelength of maximum radiative decay rate enhancement associated with coupling to the dipole mode (closed symbols). The curves for the three materials are more similar to each other than in Fig. 10.3(b). We attribute this to a better correspondence between the dielectric functions of the three materials in the spectral range of interest (see Fig. 10.4). The maximum quantum efficiencies for Ag and Au reach values of up to 31% and 25%, respectively, for a diameter of about 30 nm. These enhancements are substantially higher than the values of Fig 10.3(b), which confirms that plasmon-enhanced luminescence can be more effective for emission wavelengths above 600 nm, because interband transitions are prominent below 600 nm.

In contrast to the trend for Ag and Au, the maximum quantum efficiency for the Drude metal is smaller in Fig. 10.6(b) than in Fig. 10.3(b): 34% versus

52%, at around 30 nm. This effect is attributed to the difference in frequency dependencies of dissipation and radiation of the energy that is coupled to the dipole plasmon mode. Dissipation hardly depends on frequency, since the electron relaxation rate is fixed in the Drude model, whereas the local density of states of the embedding medium increases with the square of the transition frequency (and depends linearly on the refractive index of the medium). Consequently, plasmon-enhanced luminescence due to resonant coupling to plasmon modes of a Drude-metal sphere is more efficient at high emission frequencies (i.e., at small emission wavelengths). The smaller refractive index that is associated with the smaller resonance wavelength does not fully compensate this trend.

Figure 10.6(b) also shows quantum efficiency enhancement data obtained at the wavelengths of maximum radiative decay rate enhancement that are associated with coupling to either the quadrupole mode (open symbols) or the octupole mode (open symbols with dots). For the calculation of the maximum quantum efficiency, the contributions of all multipole modes at the wavelength of interest were taken into account for completeness. However, the radiative decay rate enhancement is dominated by the resonant mode in all cases. In Fig. 10.6(b) it is shown that, for spheres of about 75 nm, resonant coupling to the quadrupole mode can increase the quantum efficiency to 14% for Ag and to 11% for Au. The octupole mode enhances the quantum efficiency at diameters of around 130 nm, with slightly smaller maximum values as for coupling to the quadrupole mode. The quadrupole and octupole features in Fig. 10.6(b) illustrate that higher-order modes radiate rather efficiently for larger sphere sizes, which implies that they cannot be considered as dark modes for those sphere sizes. This issue is further discussed in section 10.5.

Since the quadrupole and octupole modes have smaller resonance wavelengths than the dipole mode, the associated maximum quantum efficiency enhancement occurs at a smaller wavelength, as shown in Fig. 10.6(a). Note that resonant coupling to higher-order modes is ineffective for increasing the quantum efficiency for spheres embedded in a medium with a refractive index of 1.3 (situation of Fig. 10.3), as interband transitions increase dissipation too much in the corresponding spectral range. Therefore, results on quantum efficiency enhancement associated with coupling to the quadrupole mode were not shown in Fig. 10.3.

10.5 Gersten and Nitzan model versus exact electrodynamical theory

All results in the previous sections were calculated from the exact electrodynamical theory. This section presents a comparison with the original and improved Gersten and Nitzan (GN) models, which are described in section 10.2. The advantage of the GN model is that it can be generalized to spheroids

based on an orthogonal set of eigenfunctions, so that anisotropy-induced shifts of the plasmon resonance frequencies and anisotropy-induced changes in field intensities can be accounted for. Such an orthogonal set of eigenfunctions for a spheroid is not known for exact electrodynamical theory [123].

10.5.1 Emission pattern

Figure 10.7 shows polar plots of the angular emission distribution of a source dipole located at a distance of 10 nm from the surface of a 60-nm-diameter Ag sphere, embedded in a medium with a refractive index of 1.3 for (a) the radial dipole orientation and (b) the tangential dipole orientation, both as indicated in the figure. The solid lines represent calculations by the exact electrodynamical theory, and the dashed lines represent the emission patterns associated with the GN model. The latter patterns are implicitly assumed to be dipole patterns, as the emission properties of the coupled system are characterized with an effective dipole moment, as discussed in section 10.2. The emission patterns for both dipole orientations were obtained at a specifically chosen wavelength, i.e., the wavelength that corresponds to the maximum radiative decay rate enhancement for an isotropic dipole ensemble. The numerical values for this wavelength are slightly different for the two calculation methods: 433 nm for the exact electrodynamical theory and 449 nm for the improved GN model. Both graphs are normalized to the maximum value of the emission pattern of the same source dipole in the absence of the sphere.

Figure 10.7(a) shows that, for the radial dipole orientation, the emission patterns are roughly similar in terms of shape and magnitude for both methods. The integral of the emission pattern over all solid angles, i.e., the radiative decay rate, is found to be 28 times larger than that of the same dipole emitter in the absence of the sphere, when calculated from the exact electrodynamical theory, and 26 times larger, when calculated from the GN model. In contrast, Figure 10.7(b) shows that the emission patterns for the two methods are very different for the tangential dipole orientation. The deviation from the dipole emission pattern that is obtained from the exact electrodynamical theory is obviously not described by the GN model due to its intrinsic restriction to dipole patterns. As a consequence, the calculated radiative decay rate enhancements for the tangential dipole orientation are rather different for the two methods: a factor 2.2 for the exact electrodynamical theory, and a factor 5.2 for the GN model. The fact that the emission pattern for the radial orientation resembles the dipole pattern much better than for the tangential orientation can be partly attributed to the fact that the radial dipole configuration is rotationally symmetrical, as the dipole itself, in contrast to the tangential dipole configuration. Highly structured emission patterns of an atom near an absorbing sphere have been analyzed by Dung et al. [133].

For both models, the radiative decay rate enhancements for the radial orientation are substantially different from the radiative decay rate enhancements

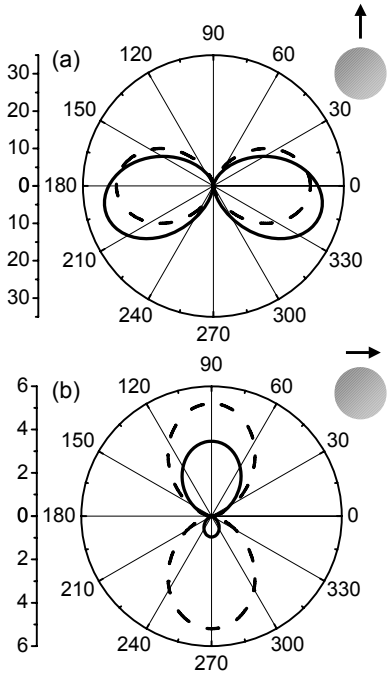

Figure 10.7: Polar plots of the angular intensity distributions of a dipole source, embedded in a medium with a refractive index of 1.3, at a distance of 10 nm from a 60-nm-diameter Ag sphere for (a) the radial dipole orientation and (b) the tangential dipole orientation, as indicated next to the polar plots. The solid lines represent calculations by the exact electrodynamical theory; the dashed lines represent the emission patterns associated with the improved GN model. The patterns in both plots are normalized to the maximum value of the emission pattern of the same source dipole in the absence of the sphere.

for the orientation tangential to the sphere surface. This feature is of great importance for designing optimized metal-emitter geometries. The orientation-dependent behavior of the radiative decay rate enhancement is further discussed in Figs. 10.9 and 10.10.

10.5.2 Emission enhancement

Figure 10.8 shows a comparison between the distance dependencies of the decay rate modifications obtained by the original (dashed lines) and improved (solid lines) GN models and by the exact electrodynamical theory (symbols). Analogous to Fig. 10.1, a Ag sphere with a diameter of 60 nm is considered.

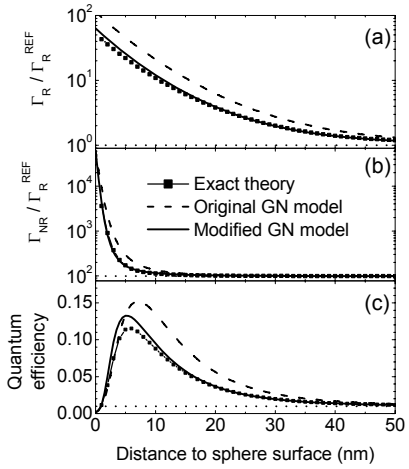

Figure 10.8: Comparison of the distance-dependent modifications of the radiative and nonradiative decay rates as well as of the quantum efficiency, as obtained by the original (dashed lines) and improved (solid lines) GN model and by the exact electrodynamical theory (symbols). (a) Radiative decay rate of a dipole emitter, the orientation of which is averaged over all solid angles, versus the distance to the surface of a 60-nm-diameter Ag sphere, and the radiative decay rate in the absence of the sphere (dotted line). (b) Nonradiative decay rate versus distance to the sphere surface, and the nonradiative decay rate in the absence of the sphere (dotted line). The decay rates in both (a) and (b) are normalized to the radiative decay rate in the absence of the sphere. (c) Quantum efficiency versus distance to the sphere surface, and the quantum efficiency in the absence of the sphere (dotted line). All curves were calculated at the wavelength of maximum radiative decay rate enhancement: 433 nm for the exact electrodynamical theory, 394 nm for the original GN model, and 449 nm for the improved GN model.

The dipole emitter, embedded in a dielectric with a refractive index of 1.3, is again assumed to have a luminescence quantum efficiency of 1% in the absence of the sphere. The dipole orientation is averaged over all solid angles.

Figure 10.8(a) shows that the radiative decay rate versus separation obtained with the improved GN model resembles the exact result significantly better than the curve obtained from the original GN model. The latter method leads to a substantial overestimation of the radiative decay rate. Figures 10.8(b) and 10.8(c) show similar effects for both nonradiative decay rate and quantum efficiency versus separation. We conclude from Figure 10.8 that the improved GN model provides a fairly accurate description of the decay rate modifications associated with resonant coupling to the dipole mode of a 60-nm-diameter Ag sphere, despite the large differences shown in Fig. 10.7(b). This is due to

the fact that the largest contribution to the orientation-averaged enhancement is associated with the radial dipole orientation for which the improved GN model and the exact theory yield quite similar radiation patterns. In addition, the slightly smaller radiative decay rate enhancement for the radial orientation (factor 26 vs. 28 at 10-nm separation), as calculated from the improved GN model, is counterbalanced by the larger enhancement for the tangential orientation (factor 5.2 vs. 2.2 at 10-nm separation).

Figures 10.7 and 10.8 focus on a 60-nm-diameter Ag sphere. In order to extend the comparison between the models to a larger sphere-diameter range, Figure 10.9 shows the dependence of the maximum quantum efficiency on sphere diameter, analogous to Fig. 10.3, calculated from the original (dashed lines) and the improved (solid lines) GN models and by the exact electrodynamical theory (symbols). Figure 10.9(a) displays the wavelength of maximum radiative decay rate enhancement versus sphere diameter for a dipole emitter positioned in close proximity to a Ag sphere, for a dipole orientation that is averaged over all solid angles. Only a small difference is found between the improved GN model and the exact theory over the whole diameter range, whereas the result from the original GN model, which does not describe the redshift of the dipole plasmon mode with increasing diameter, is entirely incorrect at larger sphere sizes. This confirms that the corrections introduced by Wokaun et al. [20, 124] provide a substantial improvement to the quasistatic description in the particle-size range of interest.

Figure 10.9(b) shows the maximum quantum efficiency of the dipole emitter versus sphere diameter calculated at the wavelengths shown in Fig. 10.9(a) for (1) the radial dipole orientation, (2) the tangential dipole orientation, and (3) the orientation averaged over all solid angles. For all three cases, the underlying optimal emitter-sphere separation (as in Fig. 10.2) is in the range between $3-10$ nm. Most notably, the original GN model does not describe the decrease in quantum efficiency enhancement for larger sphere sizes, as is obtained from the exact electrodynamical theory. In contrast, the improved GN model does describe this characteristic behavior. This difference illustrates an important advantage of the improved GN model compared to the original version. When comparing the improved GN model to the exact electrodynamical theory in more detail, perfect agreement is observed for the radial dipole orientation up to a diameter of 90 nm. For the orientation tangential to the surface, the two methods start to deviate at a diameter as small as 30 nm, consistent with was found in Fig. 10.7 for the 60-nm-diameter sphere. For the dipole orientation averaged over all solid angles, the maximum quantum efficiency enhancement, as calculated from the improved GN model, deviates 5% (i.e., 6.2% instead of 5.9%) from the exact result for a diameter of 30 nm, 15% for a diameter of 60 nm, and 35% for a diameter of 100 nm. These numbers indicate the applicability of the GN model with the corrections for radiation damping and dynamic depolarization included, when applied to larger particles.

Figures 10.7 and 10.9 show that, at the wavelength under investigation,

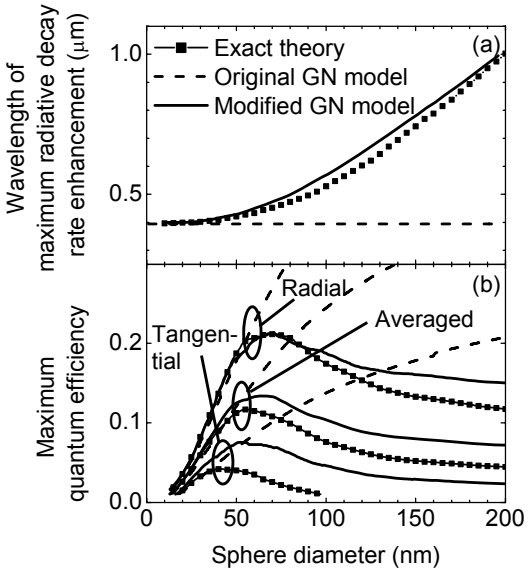

Figure 10.9: (a) Wavelength of maximum radiative decay rate enhancement associated with coupling to the dipole plasmon mode versus sphere diameter, for a dipole emitter positioned in close proximity to a Ag sphere. The orientation of the dipole is averaged over all solid angles. (b) Maximum quantum efficiency versus sphere diameter at the wavelength of maximum radiative decay rate enhancement shown in (a), for three dipole emitter orientations: radial, tangential, and averaged over all solid angles. In both graphs, results obtained with the original GN model (dashed lines), the improved GN model (solid lines), and the exact electrodynamical theory (lines with symbols) are plotted. The refractive index of the embedding medium is 1.3, and the quantum efficiency of the emitter in the absence of the sphere is 1%.

the radiative decay rate enhancement for the radial dipole orientation is substantially higher than for the tangential dipole orientation. To examine the difference between the two orientations in more detail, Figure 10.10 shows the spectral dependence of the radiative decay rate enhancement for the radial and tangential dipole orientations. The separation is fixed at 10 nm, and the refractive index of the embedding medium is 1.3. Two sphere diameters are considered: 30 nm in Fig. 10.10(a), and 60 nm in Fig. 10.10(b). The results are plotted both for the exact electrodynamical theory (symbols) and the improved GN model (lines). Figure 10.10(a) shows that, for a sphere diameter of 30 nm, the correspondence between the enhancement spectra obtained with both calculation methods is reasonably good for the tangential dipole orienta-

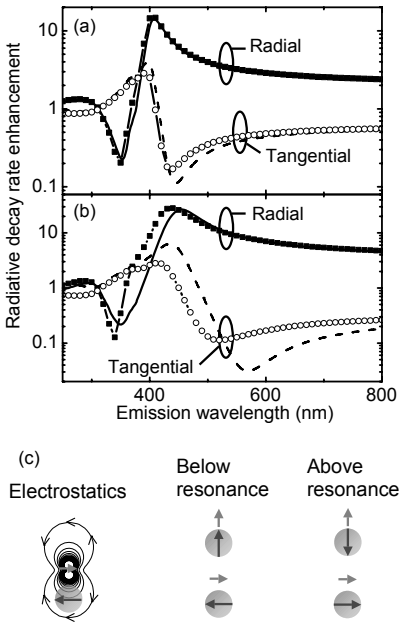

Figure 10.10: (a) and (b) Radiative decay rate enhancement, on a logarithmic scale, versus emission wavelength for a dipole emitter at a distance of 10 nm from the surface of a Ag sphere embedded in a medium with a refractive index of 1.3, for two dipole orientations: radial and tangential. The sphere diameter is 30 nm in (a) and 60 nm in (b). Results obtained with both the exact electrodynamical theory (symbols) and with the GN model (lines) are plotted. (c) Illustration of a source dipole (red) that induces a dipole (blue) in the sphere in the electrostatic limit, together with the configurations of source and induced dipoles for source dipole frequencies far below and far above the dipole resonance of the sphere.

tion, and very good for the radial orientation. The agreement between both methods again confirms the applicability of the improved GN model to particles of this size. Figure 10.10(b) illustrates that when the sphere diameter is increased, the agreement between the improved GN model and the exact electrodynamical theory diminishes.

10.5.3 Spectral trends in emission enhancement

Apart from the comparison between the two methods, Fig. 10.10(a) also provides a spectral comparison between the two dipole orientations. The enhancement spectra for both orientations are found to exhibit dispersive lineshapes

characteristic for electromagnetic resonances. We relate the dispersive lineshape to the fact that the driving field in the sphere has an orientation relative to the source dipole that depends on the source dipole orientation relative to the sphere: either the driving field is mainly parallel to the source dipole (for the radial dipole orientation) or mainly anti-parallel (for the tangential dipole orientation). Since the phase of the induced dipole in the sphere exhibits a 180 ° phase shift with respect to the driving field at the resonance frequency [41], the source dipole and the induced dipole interfere destructively below the resonance frequency (for the tangential dipole orientation) or above the resonance frequency (for the radial dipole orientation). These configurations of source dipole and induced dipole are schematically depicted in Fig. 10.10(c). Since destructive interference is associated with a reduction of the radiative decay rate, the dip in the radiative decay rate enhancement (see Fig. 10.10(a)) is either visible at emission wavelengths smaller than the dipole resonance wavelength (for the radial dipole orientation) or at wavelengths larger than the dipole resonance wavelength (for the tangential dipole orientation). Note that the reduced radiative decay rate does not necessarily lead to an increased excited state lifetime, as coupling to the dipole mode leads to an increase of the nonradiative decay as well.

The fact that the peak enhancement in Fig. 10.10(a) is different for the radiative decay rate enhancement for the two dipole orientations can be partly attributed to the fact that the near-field of a dipole is twice as strong along the dipole direction as in the perpendicular direction (for the same distance). As a consequence, a dipole that is oriented radially induces a stronger dipole in the sphere than a dipole that is oriented tangentially to the sphere surface.

10.5.4 Higher-order mode contributions to the emission enhancement

A specific aspect of the decreasing agreement between the GN model and the exact electrodynamical theory for larger spheres is illustrated in Fig. 10.11, which shows the radiative decay rate enhancement versus emission wavelength for two refractive indices of the embedding medium: 1.3 and 3.5. The calculations were done with the exact electrodynamical theory (symbols) and with the improved GN model (lines). The figure shows that the spectral features associated with coupling to the dipole mode are very similar for both calculation methods. The peaks obtained by the improved GN model have slightly higher maximum values and are centered at slightly larger wavelengths, which corresponds to the trend shown in Fig. 10.9. In addition to the features that are associated with coupling to the dipole mode, the exact electrodynamical theory shows a peak at 740 nm, for the refractive index of 3.5, which is due to coupling to the quadrupole mode. This contribution is absent in the spectrum that is obtained with the improved GN model due to the fact that this model is based on the assumption that higher-order modes are dark modes, which is

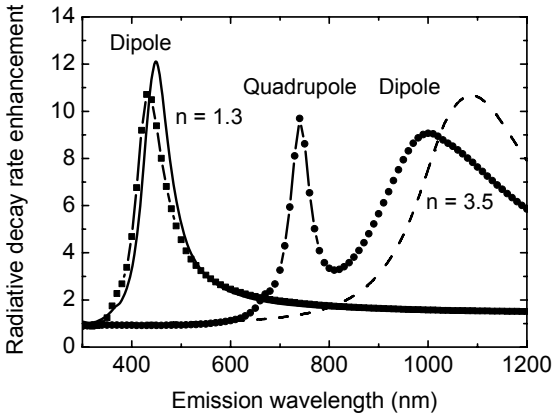

Figure 10.11: Radiative decay rate enhancement versus emission wavelength for a dipole emitter, the orientation of which is averaged over all solid angles, at a distance of 10 nm from the surface of a 60-nm-diameter Ag sphere embedded in a medium with either a refractive index of 1.3 (square symbols and solid line) or a refractive index of 3.5 (round symbols and dashed line), both calculated from the exact electrodynamical (symbols) and from the GN model (lines).

only correct for particles that are much smaller than the wavelength of light. With the high refractive index, and hence short wavelength in the embedding medium, this condition is not fulfilled. Indeed, it appears that quadrupole modes are interesting alternatives to dipole modes for emission enhancement. They provide additional wavelength tunability and narrower spectra.

10.6 Conclusions

We have used an exact electrodynamical theory to investigate modifications of the radiative and nonradiative decay rates of a dipole emitter by resonant coupling to the plasmon modes of a metal sphere at short distance. The study focused on enhancing the quantum efficiency of a low-quantum-efficiency emitter, in order to elucidate some important aspects of plasmon-enhanced luminescence.

It has been shown that characteristic features, such as the subsequent enhancement and reduction of the quantum efficiency upon decreasing the emitter-sphere separation can be described based on a local electromagnetic response, which involves coupling to both radiative and dark plasmon modes (see Fig. 10.1). The magnitude of the quantum efficiency enhancement is found to strongly depend on sphere diameter. This effect can be described based on

the electromagnetic properties of the radiative dipole mode only, without invoking coupling to dark multipole modes (see Fig. 10.2). In particular, the optimal diameter is found to originate from the trade-off between (1) the coupling strength of an emitter with a plasmon mode, which is highest for small spheres (see Fig 10.5(a)), and (2) the efficiency with which that plasmon mode couples to the far-field, which is maximal for large spheres (see Fig 10.5(b)).

The optimal sphere diameter for luminescence quantum efficiency enhancement depends both on the metal and on the embedding medium (see Figs. 10.3 and 10.6). Very small spheres (< 10 nm) are found to be ineffective for plasmon-enhanced luminescence for all metals, including the ideal Drude metal. For an embedding medium with a refractive index of 1.3, the optimal sphere diameter is 55 nm for Ag, 110 nm for Au, and 30 nm for the ideal Drude metal (see Fig. 10.3). The large spread in optimal diameters is related to the different contributions of interband transitions for Ag and Au at wavelengths below 600 nm (see Fig. 10.4). For an embedding medium with a refractive index of 3.5, which results in dipole resonances away from the interband transitions, the optimal diameter is around 30 nm for all three metals (see Fig. 10.6). At this diameter, the quantum efficiency of the emitter is increased from 1% to over 30% for the Ag sphere. Resonant coupling to higher-order modes may increase the quantum efficiency of an emitter as well, but only for larger diameters (see Fig. 10.6). The maximum quantum efficiency enhancement due to coupling with higher-order modes does however not reach the value obtained for coupling to the dipole mode.

In order to correlate the sphere-size dependence of plasmon-enhanced luminescence with the properties of individual plasmon modes, the presented analysis has been performed for a variable, optimized emission wavelength (see Figs. 10.3 and 10.6). If the emission of an atom or quantum dot with a fixed emission wavelength needs to be optimized, this approach is of limited value. Besides particle size, it is however also possible to tune particle shape, which would enable the optimization of the particle geometry for a given dipole resonance wavelength. Since the coupling of an emitter with an anisotropic particle cannot be calculated analytically from the exact electrodynamical theory, the Gersten and Nitzan model (GN) could be an appropriate alternative. Within that context, we have verified the applicability of the GN model to finite-sized particles, by comparing this model to the exact electrodynamical theory for the sphere geometry. It has been shown that the GN model, modified to include corrections for radiative damping and dynamic depolarization, provides reasonably accurate results for the decay rate modifications that are due to coupling to the dipole plasmon mode, both spatially (Fig. 10.8) and spectrally (Fig. 10.10), if the particles are small. The improved GN model is applicable over a larger size range than the original GN model, and does describe the existence of a finite optimal diameter for plasmon-enhanced luminescence (see Fig. 10.9). For the dipole orientation averaged over all solid angles, the maximum quantum efficiency enhancement, as calculated from the improved GN model,

deviates 5% from the exact result for a diameter of 30 nm, 15% for a diameter of 60 nm, and 35% for a diameter of 100 nm (see Fig. 10.9), all for an embedding medium with a refractive index of 1.3. For the radial dipole orientation, the agreement is found to be substantially better than for the tangential dipole orientation, which can be partly attributed to the rotational symmetry for the radial dipole orientation, which is absent for the tangential orientation.

Two features that are not well described by the improved GN model are the angular redistribution of emission by coupling to plasmon modes (Fig. 10.7), and the enhancement of the radiative decay rate due to coupling to higher-order plasmon modes (Figs. 10.6 and 10.11). These limitations leave unaffected that the improved GN model is a powerful tool for describing trends associated with plasmon-enhanced luminescence, not only for spheres, but also for spheroids. The applicability to spheroids enables the investigation of the influence of particle anisotropy on plasmon-enhanced luminescence in an analytical way, as will be described in Chapter 12.

10.7 Appendix: Expressions for the decay rates of an atom in the presence of a sphere according to the exact electrodynamical theory

This appendix lists the expressions for the total decay rate and the radiative decay rate of an excited atom in close proximity to a dielectric sphere, as obtained from the exact electrodynamical theory. The expressions were taken from Ref. [120].

The atom, which is modeled as a classical dipole with dipole moment μ, is positioned at a distance d from the surface of a sphere with radius a and dielectric constant $\epsilon = \epsilon' + i\epsilon''$. We consider two dipole orientations: radial and tangential. For the radial dipole orientation, i.e., perpendicular ($\perp$) to the sphere surface, we obtain:

$$\frac{\Gamma_{TOT}^{\perp}}{\Gamma_R^{REF}} = 1 + \frac{3}{2}\mathrm{Re}\sum_{l=1}^{\infty}(2l+1)l(l+1)b_l\left[\frac{h_l^{(1)}(kr)}{kr}\right]^2, \tag{10.1}$$

$$\frac{\Gamma_{RAD}^{\perp}}{\Gamma_R^{REF}} = \frac{3}{2}\sum_{l=1}^{\infty}(2l+1)l(l+1)\left|\frac{j_l(kr)+b_l h_l^{(1)}(kr)}{kr}\right|^2, \tag{10.2}$$

and for the tangential dipole orientation, i.e., parallel ($//$) to the sphere surface:

$$\frac{\Gamma_{TOT}^{//}}{\Gamma_R^{REF}} = 1 + \frac{3}{2}\mathrm{Re}\sum_{l=1}^{\infty}(l+\frac{1}{2})\left\{b_l\left[\frac{\zeta_l'(kr)}{kr}\right]^2 + a_l\left[h_l^{(1)}(kr)\right]^2\right\}, \tag{10.3}$$

$$\frac{\Gamma_{RAD}^{//}}{\Gamma_R^{REF}} = \frac{3}{4}\sum_{l=1}^{\infty}(2l+1)\times \left\{\left|j_l(kr) + a_l h_l^{(1)}(kr)\right|^2 + \left|\frac{\psi_l^{'}(kr) + b_l \zeta_l^{'}(kr)}{kr}\right|^2\right\}, \quad (10.4)$$

where Γ_R^{REF} refers to the radiative decay rate in the absence of the sphere, j_l and $h_l^{(1)}$ are the ordinary spherical Bessel and Hankel functions, $\psi_l(x) \equiv xj_l(x)$, $\zeta_l(x) \equiv xh_l^{(1)}(x)$, a_l and b_l are the Mie scattering coefficients of the sphere, $r = a + d$, $k = \sqrt{\epsilon_m}\omega/c$, ϵ_m is the dielectric constant of the embedding medium, ω the optical frequency (in radians per second), c the speed of light in vacuum, and l is the angular mode number. The derivatives of ψ_l and ζ_l are derivatives to kr. Both $\Gamma_{TOT}^{\perp}$ and $\Gamma_{TOT}^{//}$ refer to the total decay rate of an emitter with a luminescence quantum efficiency of 100% in the absence of the sphere.

In this chapter, we have considered Γ_{TOT} and Γ_R not only for the radial and tangential orientations, but also for the orientation that is averaged over all solid angles. The decay rates for the latter configuration are calculated by averaging the results for the radial and tangential orientations (with a weight factor for the tangential orientation that is twice the weight factor for the radial orientation). We have numerically verified, based on Ref. [121], that this approach is correct despite the fact that the radiative decay rate for a specific dipole orientation does not depend linearly on the Mie scattering coefficients (see Eqs. 10.2 and 10.4), in contrast to the total decay rate (see Eqs. 10.1 and 10.3).

In addition, we have decomposed the radiative and nonradiative decay rates in contributions associated with different plasmon modes. Each contribution is calculated from Eqs. 10.1 to 10.3, by first taking all Mie scattering coefficients, except the ones associated with the mode under investigation, to be zero. Second, the free-space contribution, which is equal to 1, is subtracted. Note that for the radiative decay rate, the summation does still need to be carried out over a large range of angular mode numbers l in order to describe the free-space contribution correctly.

The decomposition of the decay rates into contributions associated with the coupling to different plasmon modes is somewhat artificial as individual contributions to the radiative decay rate can yield negative values. However, this approach does facilitate the visualization of the distinct influence of different plasmon modes on phenomena such as quenching at short emitter-metal distances and the determination of the maximum quantum efficiency (see Figs. 10.1 and 10.2). Also the calculation of the wavelength of maximum radiative decay rate enhancement that is associated with a particular mode, as shown in Figs. 10.3(a), 10.6(a), and 10.8(a), relies on the decomposition of the radiative decay rate into mode-specific contributions. Note that the calculations of the

maximum quantum efficiency, as shown in Figs. 10.3(b), 10.6(b), and 10.8(b), do not rely on this procedure.

Chapter 11

Radiative decay rate enhancements in the vicinity of two-dimensional arrays of anisotropic metal nanoparticles

We present a theoretical study on the extent to which the intensity emitted by an active layer of a light-emitting device can be enhanced by an array of Ag nanoparticles. For this analysis, the radiative decay rate enhancement associated with emitter-plasmon coupling was calculated for emitters positioned in a plane below a two-dimensional array of Ag nanoparticles, using an improved version of the Gersten and Nitzan model. The in-plane-averaged radiative decay rate enhancement, which is an upper limit of the enhancement of the intensity emitted by the active layer, is found to be a factor $\sim$10 at a distance of 10 nm from the array for the optimal nanoparticle size of $\sim$100 nm. The distance at which the nanoparticles induce a substantial effect on the radiative decay rate ranges to a few tens of nanometers. Besides, the Gersten and Nitzan model predicts radiative decay rate enhancements of up to three orders of magnitude close to a sharp tip of a metal nanostructure. This results indicates that metal nanostructures can provide even larger improvements to nanoscopic light sources than for devices based on active layers.

11.1 Introduction

Near-field coupling of optical emitters to plasmon modes in metal nanostructures can greatly enhance the emitters' radiative and nonradiative decay rates. This phenomenon was first investigated in the 1970s and 1980s using rough metal films [18], and considerable progress has been achieved since then. Recently, plasmon-induced modifications of radiative and nonradiative decay rates have been measured on single molecules in systems in which the molecule-metal distance was varied *in-situ* at nanometer resolution [24]. Following these fundamental studies, the optimization of electrically driven light sources by metal nanostructures is an interesting next step. Within the context of such applications, an important question is how practical metal nanostructures should be designed to obtain the largest luminescence enhancement possible.

In this chapter, we analyze the radiative decay rate of emitters positioned in a plane below a two-dimensional array of Ag nanoparticles. The plane represents the active layer of a typical light-emitting device. In particular, we study how the magnitude of the in-plane-averaged radiative decay rate enhancement varies with nanoparticle size and with distance from the array. The in-plane-averaged radiative decay rate enhancement is an upper limit for the enhancement of the intensity emitted by the active layer of the device, under the assumption that the excitation rate is not affected by the nanoparticles. This upper limit in emitted intensity enhancement is reached either when the emitters are pumped in inversion or when the initial quantum efficiency is very low, as readily follows from a rate-equation model of an effective two-level system.

The calculations, which are performed with an improved Gersten and Nitzan model, are linked to the experimental results of the study of plasmon-enhanced photoluminescence (PL) of silicon quantum dots (Si QDs) presented in Chapter 5.

11.2 Method

The modification of the radiative decay rate of a dipole emitter in the presence of an anisotropic Ag nanoparticle can be calculated analytically using the Gersten and Nitzan (GN) model [19, 134]. This model, including the corrections associated with radiation damping and dynamic depolarization, is described in detail in Chapter 10. The used modification to include dynamic depolarization is approximately correct for anisotropic particles, i.e., the resulting expression for the induced dipole moment is, expect from a multiplicative factor, equal to the expansion of the exact solution until the third order in size parameter [135]. We focused our analysis on emitters that are positioned in a plane below a two-dimensional array of nanoparticles, as in the experiments of Chapter 5, in which cylindrical Ag disks were positioned on an SiO_2 substrate doped with

Si QDs at a well-defined depth. Several approximations were made in order to establish a link between experiment and theory.

First of all, the geometry to which the Gersten and Nitzan model can be applied is limited to spheroids. We therefore approximated the cylindrical disks as oblates. We estimated that the geometric difference between cylindrical disks and oblates has no strong effect on the radiative decay rate enhancement (at resonance) averaged over a plane below the nanoparticles. Sharp tips do have a large effect on the enhancement close to these tips, but this effect is limited to very small volumes, as is discussed in section 11.4.3.

Second, the influence of interparticle coupling on the radiative decay rate enhancement was neglected. Every emitter was thus approximated to interact with a single Ag nanoparticle. Taking interparticle coupling into account would be a refinement of the description, which primarily gives rise to angular redistribution of the emission due to interference effects, if the coupling is sufficiently strong. We estimated that interparticle coupling does not affect the in-plane-averaged radiative decay rate enhancement much, although the radiative decay rate enhancement could be very large in between nanoparticles that are spaced by a few nanometers [136]. The latter was not the case in the experiments.

Finally, the nanoparticles were assumed to be embedded in a homogeneous dielectric rather than positioned on a dielectric substrate as in the experiment. The dielectric constant of the embedding medium ϵ_m was taken to be 1.3, which is in between the dielectric constants of SiO_2 and air at optical frequencies. It is expected that this approximation changes the results slightly, but that it leaves the main features unaffected. As a consequence of all three approximations, our conclusions only relate to the major trends found in the experiment.

11.3 Results

Figure 11.1 illustrates the geometry for which the radiative decay rate enhancement is calculated. Figure 11.1(a) shows the radiative decay rate enhancement as a function of emitter position in a plane perpendicular to the minor axis of an oblate-shaped Ag nanoparticle. The distance along the minor axis between this plane and the outer surface of the oblate is 10 nm. The two major axes of the oblate measure 165 nm, the minor axis length is 20 nm. The radiative decay rate enhancement is plotted for a dipole-emitter orientation averaged over all solid angles, analogous to what has been done in Chapter 10. The same radiative decay rate enhancement data are more clearly shown in Fig. 11.1(b), i.e., without the schematic of the Ag nanoparticle. Figure 11.1(c) shows crosscuts of the radiative decay rate enhancement along the line that is indicated in Fig. 11.1(b), for two different major axis lengths: 165 nm and 260 nm. The minor axis length is fixed at 20 nm. The wavelengths for which these calculations were done are 750 nm and 1020 nm, respectively. These wavelengths, which

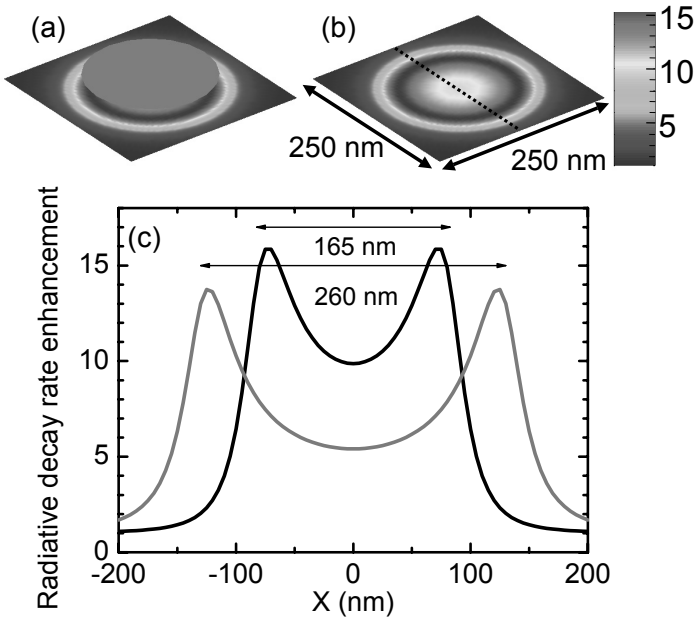

Figure 11.1: (a) Calculated radiative decay rate enhancement as a function of emitter position in a plane below an oblate-shaped Ag nanoparticle. The major (minor) axis length of the oblate is 165 nm (20 nm), the emission wavelength is 750 nm, and the dipole orientation is averaged over all solid angles. The distance along the minor axis between the plane in which the radiative decay rate enhancement is evaluated and the surface of the oblate is 10 nm. (b) Same plot as (a), but without the Ag oblate schematic. (c) Crosscut of the radiative decay rate enhancement through the plane shown in (b) along the dashed line, for two different disk diameters: 165 nm and 260 nm. The calculations were performed using the improved Gersten and Nitzan model.

are discussed in more detail later on, are the wavelengths of maximum radiative decay rate enhancement for the two geometries. Figure 11.1(c) shows that in the plane under consideration the radiative decay rate is enhanced everywhere beneath the oblate, with a maximum enhancement of a factor $\sim$15 close to the edges. The largest enhancements are found for the smallest nanoparticle. This trend is further analyzed in the next two figures.

The radiative decay rate enhancement was analyzed for 8 major axis lengths equal to the first 8 disk diameters studied experimentally, as shown in Fig. 5.1, keeping the minor axis length constant at 20 nm. The cylindrical disks of the experiment described in Chapter 5 were thus approximated as oblates with identical aspect ratios. First, the wavelengths of maximum radiative decay rate

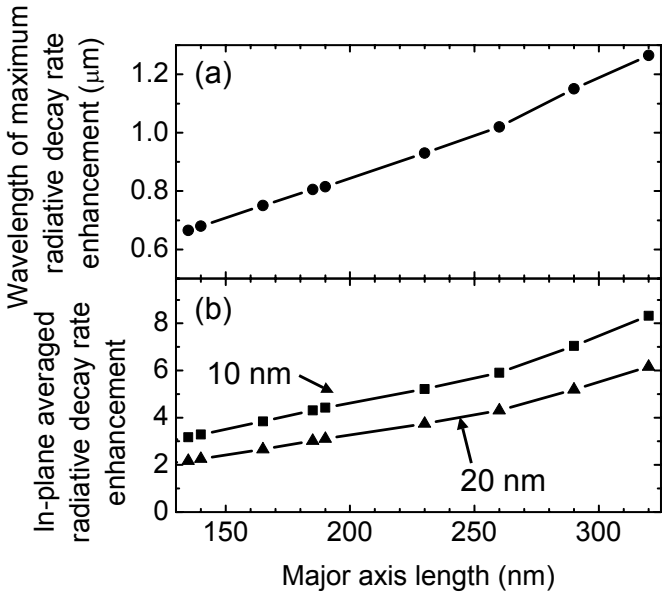

Figure 11.2: (a) Wavelength of maximum radiative decay rate enhancement versus major axis length of a Ag oblate for a dipole emitter, the orientation of which is averaged over all solid angles, positioned in close proximity to the oblate. The minor axis length of the oblate is fixed at 20 nm. (b) Radiative decay rate enhancement at the wavelength shown in (a), averaged over an area of 400×400 nm^2, versus major axis length, for two planes perpendicular to the minor axis at different distances from the surface of the oblate: 10 nm and 20 nm (along the minor axis). The calculations were performed using the improved Gersten and Nitzan model.

enhancement were calculated for all 8 configurations, and plotted versus major axis length in Fig. 11.2(a). For increasing major axis length, the wavelength of maximum radiative decay rate exhibits a redshift. This redshift is attributed to retardation effects associated with the increase in nanoparticle size and to the considerable influence of nanoparticle shape on the surface polarization, which largely determines the resonance frequency [4].

The radiative decay rate enhancement was calculated at the wavelength of maximum radiative decay rate enhancement in two planes below the oblate, for a geometry analogous to that in Fig. 11.1. These enhancements were averaged over an area of 400×400 nm^2, which is the unit cell size per metal nanoparticle of the arrays in the experiment. The procedure results in an in-plane-averaged radiative decay rate enhancement, which is plotted versus major axis length for two characteristic depths in Fig. 11.2(b). Figure 11.2(b) shows that the

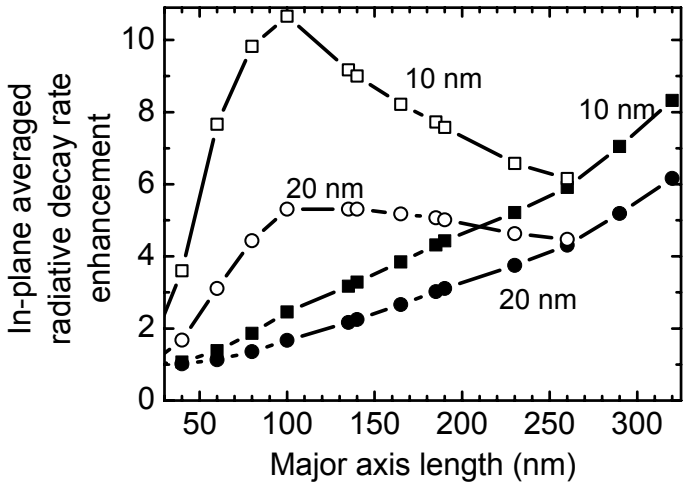

Figure 11.3: Radiative decay rate enhancement at the optimum wavelength averaged either over an area of 400×400 nm^2 (closed symbols) or over a area equal to 1.5 times the major axis length squared, for two planes perpendicular to the minor axis at different distances from the surface of the oblate: 10 nm and 20 nm (along the minor axis). The calculations were performed using the improved Gersten and Nitzan model.

calculated in-plane-averaged radiative decay rate enhancement is between a factor 2 and a factor 8, depending on size and depth. By increasing the major axis length from 130 nm to 320 nm at a constant unit cell size of 400×400 nm^2, the Ag coverage increases by more than a factor 6 from 8% to 50%. At the same time, the in-plane-averaged radiative decay rate enhancement increases with only a factor 3, for both depths. When taking into account that emitter-plasmon coupling is only effective at distances up to a few tens of nanometers, the calculations thus indicate that the radiative decay rate enhancement could be optimized by using denser arrays of smaller Ag nanoparticles, as was already suggested by the crosscuts shown in Fig. 11.1(c).

In order to estimate how much the ensemble-averaged PL intensity could be enhanced further, the calculations were extended. Instead of fixing the unit cell size at 400×400 nm^2, we fixed the Ag coverage at 35%, i.e., a unit cell width equal to 1.5 times the disk diameter. For this configuration the in-plane-averaged radiative decay rate enhancement was calculated for multiple major axis lengths, again for a constant minor axis length of 20 nm at the corresponding optimum wavelengths, and for the same two characteristic depths that were used in Fig. 11.2(b). The results are plotted in Figure 11.3 (open symbols) together with the data for a fixed unit cell size (closed symbols, partly from

Fig. 11.2(b) extended with data for smaller major axes). The open circles in Fig. 11.3 show that the in-plane-averaged radiative decay rate at the optimum wavelength can be as high as a factor 10 for a major axis length of 100 nm (for the plane at a distance along the minor axis of 10 nm from the surface of the oblate). The wavelength of maximum radiative decay rate enhancement is 570 nm for this particular geometry. For particles with a major axis length smaller than 100 nm, the radiative decay rate enhancement drops again. This trend has also been observed for the quantum efficiency enhancement of a low-quantum-efficiency emitter as a function of the size of a closely spaced metal sphere, as is described in Chapter 10. This behavior is attributed to the fact that energy coupled to plasmon modes is not reradiated as efficiently for small particles as for large particles (see Fig. 10.5). An additional contribution to the decrease in radiative decay rate enhancement for major axis lengths smaller than 100 nm is that the optimum wavelength shifts into the spectral range in which interband transitions increase the Ohmic losses of Ag (for a major axis length of 40 nm, the optimum wavelength is 425 nm). This effect does not change the qualitative behavior of the size dependence, but it changes the optimum values somewhat (see Chapter 10).

Figure 11.3 also shows that by increasing the depth from 10 nm to 20 nm, the enhancement drops from a factor 10 to a factor 5, for a major axis length of 100 nm. This effect demonstrates that the distance range in which the coupling between emitters and plasmon modes leads to substantial radiative decay rate enhancements is limited to a few tens of nanometers.

11.4 Discussion

11.4.1 Optimal array geometry

The results presented here provide important guidelines for the application of plasmonic nanostructures in light-emitting devices. First of all, the maximum in-plane-averaged radiative decay rate is about a factor 10. This maximum enhancement applies to Ag nanoparticles of which the size is optimized, for a given minor axis length of 20 nm, and it is restricted to a spectral range close to the plasmon resonance. The plasmon resonance wavelength can however be tuned across the visible and near-infrared by varying the nanoparticle shape. The second guideline is that the Ag nanoparticles should be integrated at a separation <20 nm from the active layer in order to have a substantial effect on the in-plane-averaged radiative decay rate enhancement.

Since the in-plane-averaged radiative decay rate enhancement is an upper limit for the enhancement of the emitted intensity, parameters such as the internal quantum efficiency and the excitation conditions should be taken into account in order to evaluate the intensity enhancement that can be achieved in a particular device.

An additional aspect of emitter-plasmon coupling, which we have not considered here, is that arrays of closely-spaced metal nanoparticles could also be used to direct the emission. This beaming effect, which is based on interference from light scattered by different nanoparticles, could be of additional benefit in light-emitting devices.

11.4.2 Comparison to experimental results

Next, we compare the calculated radiative decay rate enhancement to the measured PL enhancement as presented in Chapter 5. Since the calculated radiative decay rate enhancement does not describe angular redistribution of emission, which could be of influence on the detected PL intensity, this comparison is somewhat artificial. Also, the radiative decay rate enhancement is not necessarily a direct measure for the PL enhancement integrated over all solid angles, as the Si QDs were not pumped in complete saturation (see Chapter 5), and because the internal quantum efficiency of Si QDs is not well known for the applied pump intensity of 10^4 W/cm^2 [137]. Only if the Si QDs were pumped in inversion or if the initial quantum efficiency is very low, then the radiative decay rate enhancement is a direct measure for the PL enhancement, i.e., for the contribution that is not associated with an enhanced excitation rate. These conditions readily follow from a rate-equation model of an effective two-level system. The comparison with the experiment is nevertheless of interest, as it indicates if the major trends found in the calculations are supported by experimental findings.

The calculated redshift of the optimum wavelength for radiative decay rate enhancement (from 650 nm to 1250 nm, see Fig. 11.2(a)) is substantially larger than what has been observed experimentally for the PL enhancement (from 600 nm to 900 nm, see Fig. 5.5(a)). A possible explanation for this difference is the fact that the experimentally used cylindrical disks are approximated as oblates. Numerical methods, such as finite-difference time-domain (FDTD) simulations, could be used to study the difference between cylindrical and oblate shapes.

The in-plane-averaged radiative decay rate enhancement of a factor $2-8$ (Fig. 11.2(b)) corresponds quite well to the PL enhancement in the experiment of a factor $2-6$ (Fig. 5.5(b)). The calculated radiative decay rate enhancement however increases with increasing major axis length, whereas the measured PL enhancement slightly decreases. Still, both calculations and measurements show that the enhancement does not increase as fast for increasing disk diameter as the Ag coverage does, considering a fixed pitch of 400 nm. The measurements thus confirm that the luminescence enhancement can be optimized by using dense arrays of smaller Ag nanoparticles.

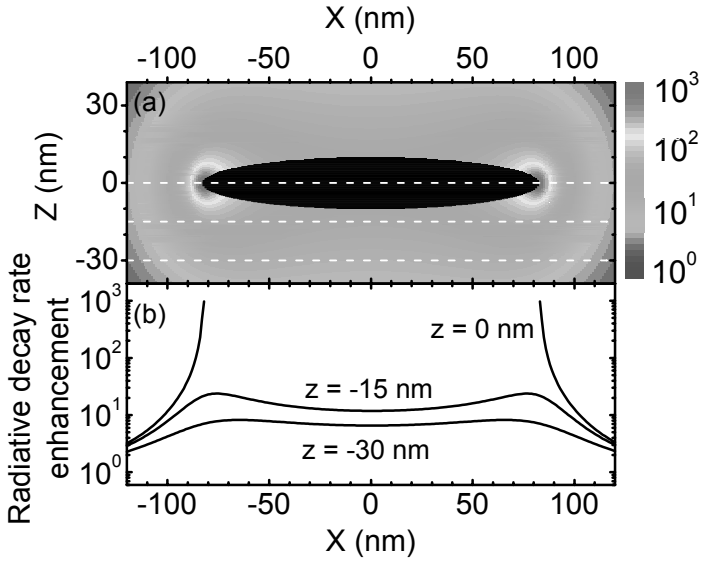

Figure 11.4: (a) Radiative decay rate enhancement in a plane through the center of the oblate parallel to the minor axis. (b) Line traces of the radiative decay rate enhancement along the dotted lines that are indicated in (a). Close to the sharp tips, the enhancement is up to three orders of magnitude. The calculations were performed using the improved Gersten and Nitzan model.

11.4.3 Radiative decay rate enhancement near a tip

The calculations presented so far have been focused on the radiative decay rate enhancement in a plane below an Ag nanoparticle array. This restriction was made in order to analyze the potential of such arrays for the optimization of light-emitting devices based on planar active layers, such as typical for LEDs. However, The GN model provides information on other configurations as well.

As an example, Figure 11.4 illustrates the effect of sharp tips on the radiative decay rate of an optical emitter. Figure 11.4(a) shows the radiative decay rate enhancement as function of emitter position in the vicinity of the same Ag oblate as considered in Fig. 11.1. The major axes measure 165 nm, and the minor axis length is 20 nm. The emission wavelength is taken to be 750 nm, and the dipole orientation is averaged over all solid angles. The map shown in Fig. 11.4(a) is for the plane through the center of the oblate, parallel to the minor axis. Figure 11.4(b) shows three line traces of the radiative decay rate enhancement. Below the nanoparticle, enhancements are similar to those in Fig. 11.1. For emitter positions close to the outer perimeter (at $z = 0$),

the radiative decay rate is enhanced by almost three orders of magnitude. Luminescence quenching due to charge transfer to the metal, which occurs at emitter-metal separations of a few nanometers, has not been taken into account in this calculation. However, also outside that distance range, the radiative decay rate enhancement is still very large. The strong influence of sharp corners on the radiative decay rate enhancement, often referred to as lightning rod effect [138], follows directly from the calculations. This is an appealing feature of the GN model. The data illustrate that plasmonic nanostructures can have a larger influence on the performance of accurately positioned nanoscopic light sources (e.g. single quantum dot nanowires [139]) than of devices based on two-dimensional active layers.

Apart from the lightning rod effect, there are other aspects of anisotropic nanoparticles that are advantageous for applications. For example, the spectral separation of radiative and dark plasmon modes. This phenomenon is discussed in Chapter 12.

11.5 Conclusions

Based on the improved Gersten and Nitzan model, we analyzed the upper limit of the enhancement of the intensity emitted by a planar active layer in the vicinity of an array of anisotropic Ag nanoparticles. The optimum enhancement for an active layer 10 nm below the array is about a factor 10, for nanoparticles with a size of ∼100 nm. The distance range at which the enhancement drops off is a few tens of nanometers. The calculated radiative decay rate enhancement is roughly similar to the PL enhancement measured in the experiment described in Chapter 5. Besides, the calculated trend that dense arrays of nanoparticles with a size of ∼100 nm give the largest enhancements is consistent with the experimental results. The radiative decay rate enhancement close to the outer perimeter of the oblate can be up to three orders of magnitude, which provides interesting opportunities for nanoscopic light sources.

Chapter 12

Spectral separation of radiative and dark plasmon modes in anisotropic metal nanoparticles

We present a theoretical study, based on an improved Gersten and Nitzan model, of the influence of particle anisotropy on the resonance wavelengths of the plasmon modes of a Ag nanoparticle. We show that particle anisotropy leads to a larger spectral separation between the radiative dipole mode and the dark higher-order modes. Partly as a consequence of this spectral separation, the quantum efficiency of a low-quantum-efficiency emitter (0.1%) can be enhanced nearly 200-fold by an anisotropic Ag nanoparticle, substantially more than the 60-fold enhancement for a spherical Ag nanoparticle.

12.1 Introduction

The excited-state lifetime of an optical emitter is reduced in the vicinity of a metal nanoparticle due to the excitation of plasmons. Since part of the energy transferred to plasmons is subsequently coupled to free-space radiation, the radiative decay rate of the emitter is effectively enhanced by this process. However, because metals exhibit Ohmic losses at optical frequencies, the excitation of plasmons enhances the nonradiative decay rate of the emitter as well. Geometrical parameters such as nanoparticle size and emitter-metal separation determine how radiative and nonradiative decay rate enhancements are balanced.

Apart from nanoparticle size and emitter-metal separation, which were discussed in detail in Chapter 10, nanoparticle shape provides an additional degree of freedom to emitter-plasmon coupling. In this chapter, we apply the improved Gersten and Nitzan model to investigate this aspect. We focus on a specific feature of anisotropic metal nanoparticles: the spectral separation of radiative and dark plasmon modes.

12.2 Method

The modifications of the radiative and nonradiative decay rates of a dipole emitter in the presence of an anisotropic Ag nanoparticle can be calculated analytically using the Gersten and Nitzan (GN) model [19, 134]. This model, including the corrections associated with radiation damping and dynamic depolarization, is described in detail in Chapter 10. The used modification to include dynamic depolarization is approximately correct for anisotropic particles, i.e., the resulting expression for the induced dipole moment is, except from a multiplicative factor, equal to a power-series expansion of the exact solution until the third order in size parameter [135]. We applied the improved GN model to an emitter that is positioned close to either a spherical or an oblate-shaped Ag nanoparticle, and we investigated the modifications of the decay rates as a function of emission wavelength.

12.3 Results

Figure 12.1 shows the influence of a 60-nm-diameter Ag sphere on the decay rates of an optical emitter as a function of emission wavelength. The emitter is positioned at a relatively small distance of 3 nm from the sphere surface, in order to illustrate the effect of dark modes on the decay rates of the emitter. The orientation of the source dipole was taken to be radial relative to the sphere, and the refractive index of the embedding medium was set to 1.5. The optical data for Ag were obtained from Ref. [42]. Figure 12.1(a) shows the radiative and nonradiative decay rates (Γ_R and Γ_{NR}, respectively) as a function

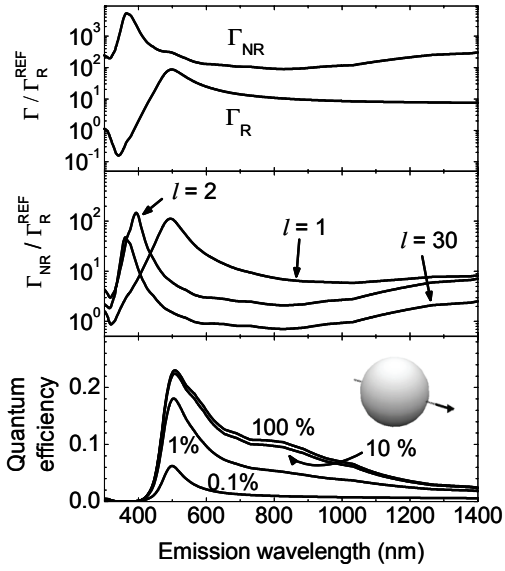

Figure 12.1: Calculations for a dipole emitter positioned at 3 nm distance from the surface of a 60-nm-diameter Ag sphere, embedded in a medium with a refractive index of 1.5. The dipole is oriented radially relative to the sphere. (a) Radiative and nonradiative decay rates as a function of emission wavelength. (b) Contributions to the nonradiative decay rate shown in (a) that are associated with coupling to plasmon modes with different angular mode numbers l. (c) Luminescence quantum efficiency of the emitter, for four different quantum efficiencies in the absence of the sphere: 0.1%, 1%, 10%, and 100%. Inset: schematic representation of the Ag nanoparticle and the source dipole. Calculation method: improved Gersten and Nitzan model.

of emission wavelength. Both Γ_R and Γ_{NR} are normalized to the radiative decay rate of the emitter in the absence of the sphere Γ_R^{REF}. The nonradiative decay rate was obtained by considering coupling to all plasmon modes up to angular mode number $l = 30$ in order to achieve convergence. Figure 12.1(a) shows that the radiative decay rate exhibits a variation by nearly three orders of magnitude; the radiative decay rate is largest around 500 nm. The nonradiative decay rate exceeds the radiative decay rate over the full spectral range, and peaks around 400 nm. Figure 12.1(b) shows contributions to the nonradiative decay rate of three plasmon modes with different angular mode number l: $l = 1$ (dipole mode), $l = 2$ (quadrupole mode), and $l = 30$ (highest order evaluated). The dipole-mode contribution peaks at the same wavelength as the radiative decay rate enhancement in Fig. 12.1(a), whereas the higher-order modes peak

at shorter wavelengths. The integrated effect of all higher-order modes on the nonradiative decay rate explains the different wavelengths of maximum decay rate enhancement shown in Fig. 12.1(a).

Figure 12.1(c) shows the quantum efficiency $\eta = \Gamma_R/(\Gamma_R + \Gamma_{NR})$ of the emitter as a function of emission wavelength for four different reference quantum efficiencies η^{REF} (i.e., quantum efficiency in the absence of the sphere): 0.1%, 1%, 10%, and 100%. The curves were obtained from the data shown in Fig. 12.1(a) by adding appropriate offsets to the nonradiative decay rate. The quantum efficiencies are practically zero at wavelengths below 400 nm, which is attributed to the efficient excitation of dark higher-order plasmon modes and the low radiative decay rate at these wavelengths. For $\eta^{REF} = 0.1\%$, the quantum efficiency is enhanced to about 6% at a wavelength of 500 nm. The quantum efficiency enhancement is thus as high as a factor 60. For $\eta^{REF} = 1\%$ and $\eta^{REF} = 10\%$, the maximum quantum efficiencies are about 18% and 22%, corresponding to enhancements of a factor 18 and a factor 2.2, respectively. For $\eta^{REF} = 100\%$, the quantum efficiency spectrum hardly deviates from the spectrum for $\eta^{REF} = 10\%$. This is attributed to the fact that in both cases the excited-state decay is dominated by the excitation of plasmons. The quantum efficiency of the emitter then corresponds to the outcoupling efficiency of plasmons to free-space radiation, which is independent of η^{REF}. Figure 12.1(c) indicates that plasmon-enhanced luminescence is particularly effective for low-quantum-efficiency emitters. Since higher-order modes contribute to the nonradiative decay rate even at the optimum wavelength of 500 nm, as shown in Fig. 12.1(b), the quantum efficiency could be further enhanced if coupling to dark higher-order modes could be suppressed. As an indication how much could be gained by this approach, the quantum efficiency for $\eta^{REF} = 1\%$ would be enhanced to 29% instead of 18%, at the wavelength of 500 nm, if coupling to higher-order modes could be neglected. This result follows from the calculations by ignoring contributions to the nonradiative decay rate that are associated with higher-order modes.

Figure 12.2 shows similar spectra as Fig. 12.1, but for an oblate-shaped particle with an aspect ratio (major axis length divided by minor axis length) of 5. The oblate volume is identical to the volume of the 60-nm-diameter sphere considered in Fig. 12.1. The emitter is positioned along a major axis at a distance of 3 nm from the oblate surface, with the dipole orientation parallel to the axis. Figure 12.2(a) shows the radiative and nonradiative decay spectra. A clear difference with the data for the spherical particle in Fig. 12.1 is that the maximum of the radiative decay rate enhancement is shifted from 500 nm to 720 nm. At the same time, the main nonradiative decay rate peak is hardly shifted. The nonradiative decay rate spectrum shows more structure than that for the spherical particle. The origin of this effect becomes clear from the plots of nonradiative decay rate contributions associated with different plasmon modes shown in Fig. 12(b). The dipole-mode contribution to the nonradiative decay rate peaks at 720 nm, corresponding to the radiative

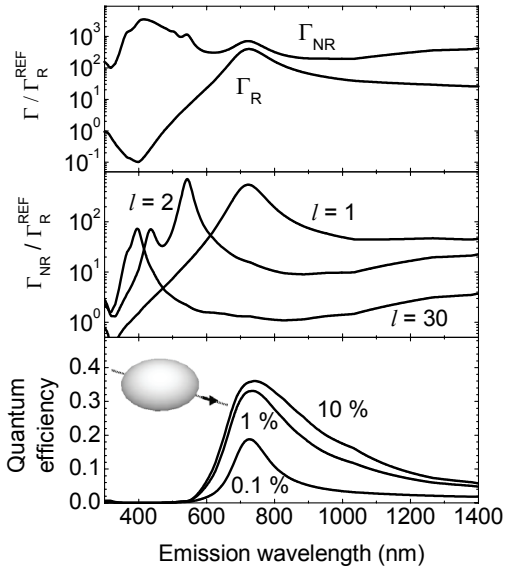

Figure 12.2: Calculations for a dipole emitter positioned at 3 nm distance from the outer perimeter of an Ag oblate with an aspect ratio of 5 and a volume equal to the volume of a 60-nm-diameter sphere, embedded in a medium with a refractive index of 1.5 (see text for exact emitter position and dipole orientation). (a) Radiative and nonradiative decay rates as a function of emission wavelength. (b) Contributions to the nonradiative decay rate shown in (a) that are associated with coupling to plasmon modes with different angular mode numbers l. (c) Luminescence quantum efficiency of the emitter, for three different quantum efficiencies in the absence of the sphere: 0.1%, 1%, and 10%. Inset: schematic representation of the Ag nanoparticle and the source dipole. Calculation method: improved Gersten and Nitzan model.

decay rate maximum. The higher-order mode contributions, which have not redshifted as much as the dipole-mode contribution, show a double-peak structure caused by the lifted degeneracy for modes with different azimuthal mode numbers m in anisotropic particles. The difference in spectral shifts between the dipole mode and higher-order modes is attributed to the fact that higher-order modes, with large numbers of closely-spaced poles in the electric field, are less dependent on the surface curvature of the nanoparticle.

Figure 12.2(c) shows quantum efficiency spectra for $\eta^{REF} = 0.1\%$, 1%, and 10%. The spectrum for $\eta^{REF} = 100\%$ is not plotted, and coincides almost exactly with the spectrum for $\eta^{REF} = 10\%$. The maximum quantum efficiencies for $\eta^{REF} = 0.1\%$, 1%, and 10% are: 19%, 33%, and 36%, respectively. These quantum efficiencies are all substantially higher than the values obtained for

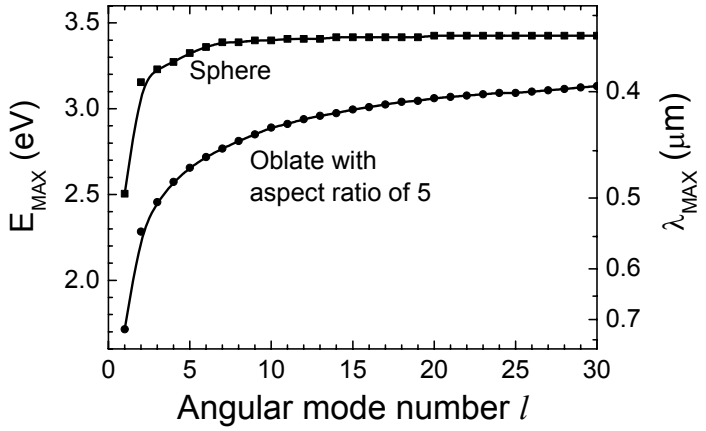

Figure 12.3: Photon energy E_{max} at which the contribution to the nonradiative decay rate associated with coupling to a particular plasmon mode peaks versus angular mode number l of the plasmon mode. The two emitter-particle configurations that are considered are the same as in Figs. 12.1 and 12.2. λ_{max} is the free-space wavelength that corresponds to E_{max}. The lines are guides to the eye. Calculation method: improved Gersten and Nitzan model.

the spherical particle. For $\eta^{REF} = 0.1\%$ for example, the quantum efficiency enhancement increases from a factor 60 for spherical nanoparticles to a factor 190 for oblates. In order to quantify the effect of the spectral separation of plasmon modes on the improved quantum efficiency enhancement, we have also calculated the quantum efficiency by neglecting coupling to higher-order modes. In that case the quantum efficiency for $\eta^{REF} = 1\%$ is 38% instead of 33%. Since the difference between these values is significantly less than the difference between the same benchmarks for spherical nanoparticles (i.e., 29% and 18%, respectively), we conclude that the influence of the dark higher-order modes is substantially reduced for anisotropic nanoparticles.

The increased spectral separation of radiative and dark plasmon modes with increasing anisotropy is represented in a different way in Fig. 12.3. This graph shows the photon energy E_{max} at which the nonradiative decay rate associated with coupling to a particular plasmon mode is highest, plotted versus angular mode number l of the plasmon mode. These photon energies correspond to the maxima of the spectra shown in Figs. 12.1(b) and 12.2(b). For clarity, the associated free-space wavelength λ_{max} is indicated on the righthand scale. For high angular mode numbers, both curves converge to a constant level that corresponds to the surface plasmon resonance energy of a flat interface between

Ag and a dielectric with a refractive index of 1.5. This behavior, which readily follows from the expression for the resonance condition for higher-order plasmon modes [122], confirms that higher-order modes with closely-spaced charge nodes depend less on the surface curvature than the lowest-order modes. The redshift for lower angular mode numbers is found to be stronger for the anisotropic than for the spherical nanoparticle. Since the radiative decay rate enhancement is associated with coupling to the dipole mode ($l = 1$), the larger spectral separation between the dipole mode and higher-order plasmon modes is an advantage: emitters with the appropriate emission wavelength can be coupled preferentially to the plasmon mode that couples most efficiently to free-space radiation.

12.4 Conclusions

We have shown that the longitudinal dipole plasmon mode of an anisotropic metal nanoparticle is better spectrally separated from higher-order plasmon modes than the dipole plasmon mode of a spherical metal nanoparticle. This conclusion has been drawn from calculations performed with an improved Gersten and Nitzan model. The larger spectral separation of radiative and dark plasmon modes in anisotropic metal nanoparticles has the advantage that emitters, the emission of which is resonant with the dipole plasmon mode, can transfer a larger fraction of their energy to the plasmon mode that couples most efficiently to free-space radiation. Partly as a consequence of this spectral separation, the quantum efficiency of a low-quantum-efficiency emitter (0.1%) can be enhanced nearly 200-fold by an anisotropic Ag nanoparticle, substantially more than the 60-fold enhancement for a spherical Ag nanoparticle.

References

[1] W. L. Barness, A. Dereux, and T. W. Ebbesen, *Surface plasmon subwavelength optics*, Nature **424**, 824 (2003).

[2] S. A. Maier and H. A. Atwater, *Plasmonics: Localization and guiding of electromagnetic energy in metal/dielectric structures*, J. Appl. Phys. **98**, 011101 (2005).

[3] E. Ozbay, *Plasmonics: Merging photonics and electronics at nanoscale dimensions*, Science **311**, 189 (2006).

[4] U. Kreibig and M. Vollmer, *Optical properties of metal clusters*, Springer, Berlin, 1995.

[5] K. Sokolov, M. Follen, J. Aaron, I. Pavlova, A. Malpica, R. Lotan, and R. Richards-Kortum, *Real-time vital optical imaging of precancer using anti-epidermal growth factor receptor antibodies conjugated to gold nanoparticles*, Cancer Res. **63**, 1999 (2003).

[6] S. Pillai, K. R. Catchpole, T. Trupke, G. Zhang, J. Zhao, and M. A. Green, *Enhanced emission from Si-based light-emitting diodes using surface plasmons*, Appl. Phys. Lett. **88**, 161102 (2006).

[7] L. R. Hirsch, A. M. Gobin, A. R. Lowery, F. Tam, R. A. Drezek1, N. J. Halas, and J. L. West, *Metal nanoshells*, Ann. of Biochem. Eng. **34**, 15 (2006).

[8] D. Boyer, P. Tamarat, A. Maali, B. Lounis, and M. Orrit, *Photothermal imaging of nanometer-sized metal particles among scatterers*, Science **297**, 1160 (2002).

[9] M. Quinten, A. Leitner, J. R. Krenn, and F. R. Aussenegg, *Electromagnetic energy transport via linear chains of silver nanoparticles*, Opt. Lett. **23**, 1331 (1998).

[10] S. A. Maier, P. G. Kik, H. A. Atwater, S. Meltzer, E. Harel, B. E. Koel, and A. A. G. Requicha, *Local detection of electromagnetic energy transport below the diffraction limit in metal nanoparticle plasmon waveguides*, Nat. Mater. **2**, 229 (2003).

[11] K. Kneipp, Y. Wang, H. Kneipp, L. T. Perelman, I. Itzkan, R. R. Dasari, and M. S. Feld, *Single molecule detection using surface-enhanced Raman scattering (SERS)*, Phys. Rev. Lett. **78**, 1667 (1997).

[12] S. M. Nie and S. R. Emery, *Probing single molecules and single nanoparticles by surface-enhanced Raman scattering*, Science **275**, 1102 (1997).

[13] M. Moskovits, *Surface-enhanced spectroscopy*, Rev. Mod. Phys. **57**, 783 (1985).

[14] C. D. Geddes and J. R. Lakowicz, *Metal-enhanced fluorescence*, J. Fluoresc. **12**, 121 (2002).

[15] E. Purcell, *Spontaneous emission probabilities at radio frequencies*, Phys. Rev. **69**, 681 (1946).

[16] G. W. Ford and W. H. Weber, *Electromagnetic interactions of molecules with metal surfaces*, Phys. Rep. **113**, 195 (1984).

[17] R. R. Chance, A. Prock, and R. Silbey, *Molecular fluorescence and energy transfer*

near interfaces, Adv. Chem. Phys. **37**, 1 (1978).

[18] A. Wokaun, H.-P. Lutz, A. King, U. Wild, and R. Ernst, *Energy transfer in surface enhanced luminescence*, J. Chem. Phys. **79**, 509 (1983).

[19] J. Gersten and A. Nitzan, *Spectroscopic properties of molecules interacting with small dielectric particles*, J. Chem. Phys. **75**, 1139 (1981).

[20] A. Wokaun, J. P. Gordon, and P. F. Liao, *Radiation damping in surface-enhanced Raman scattering*, Phys. Rev. Lett. **48**, 957 (1982).

[21] R. Ruppin, *Decay of an excited molecule near a small sphere*, J. Chem. Phys. **76**, 1681 (1982).

[22] P. Anger, P. Bharadwaj, and L. Novotny, *Enhancement and quenching of single-molecule fluorescence*, Phys. Rev. Lett. **96**, 113002 (2006).

[23] J. N. Farahani, D. W. Pohl, H.-J. Eisler, and B. Hecht, *Single quantum dot coupled to a scanning optical antenna: a tunable superemitter*, Phys. Rev. Lett. **95**, 017402 (2005).

[24] S. Kühn, U. Håkanson, L. Rogobete, and V. Sandoghdar, *Enhancement of single-molecule fluorescence using a gold nanoparticle as an optical nanoantenna*, Phys. Rev. Lett. **97**, 017402 (2006).

[25] R. M. Amos and W. L. Barnes, *Modification of the spontaneous emission rate of Eu^{3+} ions close to a thin metal mirror*, Phys. Rev. B **55**, 7249 (1997).

[26] E. Dulkeith, A. C. Morteani, T. Niedereichholz, T. A. Klar, J. Feldmann, S. A. Levi, F. J. C. M. van Veggel, D. N. Reinhoudt, M. Möller, and D. I. Gittins, *Fluorescence quenching of dye molecules near gold nanoparticles: radiative and nonradiative effects*, Phys. Rev. Lett. **89**, 203002 (2002).

[27] O. G. Tovmachenko, C. Graf, D. J. van den Heuvel, A. van Blaaderen, and H. C. Gerritsen, *Fluorescence enhancement by metal-core/silica-shell nanoparticles*, Adv. Mater. **18**, 91 (2006).

[28] V. A. Podolskiy, A. K. Sarychev, E. E. Narimanov, and V. M. Shalaev, *Light manipulation with plasmonic nanoantennas*, Proceedings of the annual APS/URSI meeting **2**, 1915 (2004).

[29] P. Mühlschlegel, H.-J. Eisler, O. J. F. Martin, B. Hecht, and D. W. Pohl, *Resonant optical antennas*, Science **308**, 1607 (2005).

[30] W. Chen and H. Ahmed, *Fabrication of $5-7$ nm wide etched lines in silicon using 100 keV electron-beam lithography and polymethylmethacrylate resist*, Appl. Phys. Lett. **62**, 1499 (1993).

[31] S. Yasin, D. G. Hasko, and H. Ahmed, *Fabrication of <5 nm width lines in poly(methylmethacrylate) resist using a water:isopropyl alcohol developer and ultrasonically-assisted development*, Appl. Phys. Lett. **78**, 2760 (2001).

[32] W. Kern and D. A. Puotinen, *Cleaning solutions based on hydrogen peroxide for use in silicon semiconductor technology*, RCA Rev. **31**, 187 (1970).

[33] D. Küpper, D. Küpper, T. Wahlbrink, J. Bolton, M. C. Lemme, Y. M. Georgiev, and H. Kurz, *Megasonic-assisted development of nanostructures*, J. Vac. Sci. Technol. B **24**, 1827 (2006).

[34] D. D. Nolte, *Optical scattering and absorption by metal nanoclusters in GaAs*, J. Appl. Phys. **76**, 3740 (1994).

[35] G. Xu, M. Tazawa, P. Jin, S. Nakao, and K. Yoshimura, *Wavelength tuning of surface plasmon resonance using dielectric layers on silver island films*, Appl. Phys. Lett. **82**, 3811 (2003).

[36] T. R. Jensen, M. D. Malinsky, C. L. Haynes, and R. P. V. Duyne, *Nanosphere lithography: tunable localized surface plasmon resonance of silver nanoparticles*, J. Phys.

Chem. B **104**, 10549 (2000).

[37] W. Rechberger, A. Hohenau, A. Leitner, J. R. Krenn, B. Lamprecht, and F. R. Aussenegg, *Optical properties of two interacting gold nanoparticles*, Opt. Commun. **220**, 137 (2003).

[38] J. J. Penninkhof, A. Polman, L. A. Sweatlock, S. A. Maier, H. A. Atwater, A. M. Vredenberg, and B. J. Kooi, *Mega-electron-volt ion beam induced anisotropic plasmon resonance of silver nanocrystals in glass*, Appl. Phys. Lett. **83**, 4137 (2003).

[39] R. Schlatmann, C. Lu, J. Verhoeven, F. J. Puik, and M. J. van der Wiel, *Modification by argon and krypton ion bombardement of Mo/Si x-ray multilayers*, Appl. Surf. Sci. **78**, 147 (1994).

[40] E. Spiller, A. Segmüller, J. Rife, and R.-P. Haelbich, *Controlled fabrication of multilayer soft-x-ray mirrors*, Appl. Phys. Lett. **37**, 1048 (1980).

[41] C. Bohren and D. Huffman, *Absorption and scattering of light by small particles*, Wiley, New York, 1983.

[42] E. D. Palik, *Handbook of optical constants of solids*, Academic Press, Orlando, FL, 1985.

[43] O. Stenzel, A. Stendal, M. Röder, and C. von Borczyskowski, *Tuning of the plasmon absorption frequency of silver and indium nanoclusters via thin amorphous silcion films*, Pure Appl. Opt. **6**, 577 (1997).

[44] M. L. Brongersma, J. W. Hartman, and H. A. Atwater, *Electromagnetic energy transfer and switching in nanoparticle chain arrays below the diffraction limit*, Phys. Rev. B **62**, 16356 (2000).

[45] F. Hache, D. Ricard, and C. Flytzanis, *Optical nonlinearities of small metal particles: surface-mediated resonance and quantum size effects*, J. Opt. Soc. Am. B **3**, 1647 (1986).

[46] A. Dakka, J. Lafait, C. Sella, S. Berthier, M. Abd-Lefdil, J.-C. Martin, and M. Maaza, *Optical propeties of Ag-TiO_2 nanocermet films prepared by cosputtering and multilayer deposition techniques*, Appl. Opt. **39**, 2745 (2000).

[47] J. Haus, N. Kalyaniwalla, R. Inguva, and C. Bowden, *Optical bistability in small metallic particle composites*, J. Appl. Phys. **65**, 1420 (1989).

[48] G. Nikklasson and C. Granqvist, *Optical properties and solar selectivity of coevaporated Cu-Al_2O_3 composite films*, J. Appl. Phys. **55**, 3382 (1984).

[49] M. Bloemer and J. Haus, *Broadband waveguide polarizers based on the anisotropic optical constants of nanocomposite films*, J. Lightwave Technol. **14**, 1534 (1996).

[50] G. Arnold and J. Borders, *Aggregation and migration of ion-implanted silver in lithia-alumina-silica glass*, J. Appl. Phys. **48**, 1488 (1977).

[51] G. De, A. Licciulli, C. Massaro, L. Tapfer, M. Catalano, G. Battaglin, C.Meneghini, and P. Mazzoldi, *Silver nanocrystals in silica by sol-gel processing*, J. Non-Cryst. Sol. **194**, 225 (1996).

[52] H. B. Liao, R. F. Xiao, J. S. Fu, P. Yu, G. K. L. Wong, and P. Sheng, *Large third-order optical nonlinearity in Au:SiO_2 composite films near the percolation threshold*, Appl. Phys. Lett. **70**, 1 (1997).

[53] F. Caccavale, G. D. Marchi, F. Gonella, P. Mazzoldi, G. Meneghini, A. Quaranta, G. Arnold, G. Battaglin, and G. Mattei, *Irradiation-induced Ag-colloid formation in ion-exchanged soda-lime glass*, Nucl. Instr. Meth. B **96**, 382 (1995).

[54] C. Strohhöfer, J. Hoogenboom, A. van Blaaderen, and A. Polman, *Highly dispersive micropatterns in ion-exchanged glass formed by ion irradiation through a mask of colloidal particles*, Adv. Mater. **14**, 1815 (2002).

[55] D. Peters, C. Strohhöfer, M. Brongersma, J. van der Elsken, and A. Polman, *For-*

mation mechanism of silver nanocrystals made by ion irradiation of $Na^+ \leftrightarrow Ag^+$ ion-exchanged sodalime silicate glass, Nucl. Instr. Meth. B **168**, 237 (2000).

[56] C. Wagner, W. Riggs, L. Davis, J. Moulder, and G. Muilenberg, *Handbook of x-ray photoelectron spectroscopy*, Perkin-Elmer, Eden Prairie, MN, 1979.

[57] E. Borsella, E. Cattaruzza, G. D. Marchi, F. Gonella, G. Mattei, P. Mazzoldi, A. Quaranta, G. Battaglin, and R. Polloni, *Synthesis of silver clusters in silica-based glasses for optoelectronics applications*, J. Non-Cryst. Sol. **245**, 122 (1999).

[58] G. D. Marchi, F. Caccavale, F. Gonella, G. Mattei, P. Mazzoldi, G. Battaglin, and A. Quaranta, *Silver nanoclusters formation in ion-exchanged waveguides by annealing in hydrogen atmosphere*, Appl. Phys. A **63**, 403 (1996).

[59] A. Miotello, G. D. Marchi, G. Mattei, and P. Mazzoldi, *Ionic transport model for hydrogen permeation including silver nanocluster formation in silver-sodium exchanged glasses*, Appl. Phys. A **67**, 527 (1998).

[60] C. Strohhöfer, *Optical properties of ion beam modified waveguide materials doped with erbium and silver*, Ph.D. Thesis, Utrecht University, FOM Institute for Atomic and Molecular Physics, Amsterdam, The Netherlands, 2001.

[61] E. Valentin, H. Bernas, C. Ricolleau, and F. Creuzet, *Ion beam photography: decoupling nucleation and growth of metal clusters in glass*, Phys. Rev. Lett. **86**, 99 (2001).

[62] C. Strohhöfer and A. Polman, *Silver as a sensitizer for erbium*, Appl. Phys. Lett. **81**, 1414 (2002).

[63] L. T. Canham, *Silicon quantum wire array fabrication by electrochemical and chemical dissolution of wafers*, Appl. Phys. Lett. **57**, 1046 (1990).

[64] A. G. Cullis and L. T. Canham, *Visible light emission due to quantum size effects in highly porous crystalline silicon*, Nature **353**, 335 (1991).

[65] T. Fischer, V. Petrova-Koch, K. Shcheglov, M. S. Brandt, and F. Koch, *Continuously tunable photoluminescence from Si^+-implanted and thermally annealed SiO_2 films*, Thin Solid Films **276**, 100 (1996).

[66] M. V. Wolkin, J. Jorne, P. M. Fauchet, G. Allan, and C. Delerue, *Electronic states and luminescence in porous silicon quantum dots: the role of oxygen*, Phys. Rev. Lett. **82**, 197 (1999).

[67] R. J. Walters, J. Kalkman, A. Polman, H. A. Atwater, and M. J. A. de Dood, *Photoluminescence quantum efficiency of dense silicon nanocrystal ensembles in SiO_2*, Phys. Rev. B **73**, 132302 (2006).

[68] J. F. Ziegler, J. P. Biersack, and U. Littmark, *The stopping and range of ions in solids*, Pergamon Press, New York, 1985.

[69] K. S. Min, K. V. Shcheglov, C. M. Yang, H. A. Atwater, M. L. Brongersma, and A. Polman, *Defect-related versus excitonic visible light emission from ion beam synthesized Si nanocrystals in SiO_2*, Appl. Phys. Lett. **69**, 2033 (1996).

[70] L. A. Blanco and F. J. García de Abajo, *Spontaneous light emission in complex nanostructures*, Phys. Rev. B **69**, 205414 (2004).

[71] K. T. Shimizu, W. K. Woo, B. R. Fisher, H. J. Eisler, and M. G. Bawendi, *Surface-enhanced emission from single semiconductor nanocrystals*, Phys. Rev. Lett. **89**, 117401 (2002).

[72] H. Ditlbacher, N. Félidj, J. R. Krenn, B. Lamprecht, A. Leitner, and F. R. Aussenegg, *Electromagnetic interaction of fluorophores with designed two-dimensional silver nanoparticle arrays*, Appl. Phys. B **73**, 373 (2001).

[73] J. S. Biteen, N. S. Lewis, H. A. Atwater, H. Mertens, and A. Polman, *Spectral tuning of plasmon-enhanced silicon quantum dot luminescence*, Appl. Phys. Lett. **88**, 131109 (2006).

[74] M. L. Brongersma, A. Polman, K. S. Min, E. Boer, T. Tambo, and H. A. Atwater, *Tuning the emission wavelength of Si nanocrystals in SiO_2 by oxidation*, Appl. Phys. Lett. **72**, 2577 (1998).

[75] S. Zou and G. C. Schatz, *Narrow plasmonic/photonic extinction and scattering line shapes for one and two dimensional silver nanoparticle arrays*, J. Chem. Phys. **121**, 12606 (2004).

[76] E. M. Hicks, S. S. Zou, G. Schatz, K. Spears, R. V. Duyne, L. Gunnarsson, T. Rindzevicius, B. Kasemo, and M. Käll, *Controlling plasmon line shapes through diffractive coupling in linear arrays of cylindrical nanoparticles fabricated by electron beam lithography*, Nano Lett. **5**, 1065 (2005).

[77] N. Félidj, G. Laurent, J. Aubard, G. Lévi, A. Hohenau, J. R. Krenn, and F. R. Aussenegg, *Grating-induced plasmon mode in gold nanoparticle arrays*, J. Chem. Phys. **123**, 221103 (2005).

[78] J. Valenta, R. Juhasz, and J. Linnros, *Photoluminescence spectroscopy of single silicon quantum dots*, Appl. Phys. Lett. **80**, 1070 (2002).

[79] R. J. Walters, G. I. Bourianoff, and H. A. Atwater, *Field-effect electroluminescence in silicon nanocrystals*, Nat. Mater. **4**, 143 (2005).

[80] R. J. Walters, P. G. Kik, J. D. Casperson, H. A. Atwater, R. Lindstedt, M. Giorgi, and G. Bourianoff, *Silicon optical nanocrystal memory*, Appl. Phys. Lett. **85**, 2622 (2004).

[81] K. R. Williams, K. Gupta, and M. Wasilik, *Etch rates for micromachining processing - Part III*, Journal of Microelectromechanical Systems **12**, 761 (2003).

[82] J. Kalkman, H. Gersen, L. Kuipers, and A. Polman, *Excitation of surface plasmons at a SiO_2-Ag interface by silicon quantum dots: Experiment and theory*, Phys. Rev. B **73**, 075317 (2006).

[83] J. S. Biteen, *Plasmon-enhanced silicon nanocrystal luminescence for optoelectronic applications*, Ph.D. Thesis, California Institute of Technology, Pasadena, CA, 2006.

[84] G. N. van den Hoven, A. Polman, C. van Dam, J. W. M. van Uffelen, and M. K. Smit, *Net optical gain at 1.53 μm in Er-doped Al_2O_3 waveguides on silicon*, Appl. Phys. Lett. **68**, 1886 (1996).

[85] A. Polman, B. Min, J. Kalkman, T. Kippenberg, and K. Vahala, *Ultra-low threshold erbium-implanted toroidal microlaser on silicon*, Appl. Phys. Lett. **84**, 1037 (2004).

[86] M. E. Castagna, S. Coffa, M. Monaco, A. Muscara, L. Caristia, S. Lorenti, and A. Messina, *High efficiency light emitting devices in silicon*, Mater. Sci. Eng. B **83**, 105 (2003).

[87] G. S. Pomrenke, P. B. Klein, and D. W. Langer, editors, *Rare earth doped semiconductors*, MRS Symp. Proc. No. 301 (Materials Research Society), Pittsburgh, 1993.

[88] S. Coffa, A. Polman, and R. N. Schwartz, editors, *Rare earth doped semiconductors II*, MRS Symp. Proc. No. 422 (Materials Research Society), Pittsburgh, 1996.

[89] P. G. Kik, M. J. A. de Dood, K. Kikoin, and A. Polman, *Excitation and deexcitation of Er^{3+} in crystalline silicon*, Appl. Phys. Lett. **70**, 1721 (1997).

[90] S. Coffa, G. Franzò, F. Priolo, A. Polman, and R. Serna, *Temperature dependence and quenching processes of the intra-4f luminescence of Er in crystalline Si*, Phys. Rev. B **49**, 16313 (1994).

[91] F. Priolo, G. Franzò, S. Coffa, and A. Carnera, *Excitation and nonradiative deexcitation processes of Er^{3+} in crystalline Si*, Phys. Rev. B **57**, 4443 (1998).

[92] F. Priolo, G. Franzò, S. Coffa, A. Polman, S. Libertino, R. Barklie, and D. Carey, *The erbium-impurity interaction and its effect on the 1.54 μm luminescence of Er^{3+} in silicon*, J. Appl. Phys. **78**, 3874 (1995).

[93] S. Coffa, G. Franzò, and F. Priolo, *High efficiency and fast modulation of Er-doped*

light emitting Si diodes, Appl. Phys. Lett. **69**, 2077 (1996).

[94] A. M. Vredenberg, N. E. J. Hunt, E. F. Schubert, D. C. Jacobson, J. M. Poate, and G. J. Zydzik, *Controlled atomic spontaneous emission from Er^{3+} in a transparent Si/SiO_2 microcavity*, Phys. Rev. Lett. **71**, 517 (1993).

[95] E. Snoeks, A. Lagendijk, and A. Polman, *Measuring and modifying the spontaneous emission rate of erbium near an interface*, Phys. Rev. Lett. **74**, 2459 (1995).

[96] H. Mertens, J. S. Biteen, H. A. Atwater, and A. Polman, *Polarization-selective plasmon-enhanced silicon quantum dot luminescence*, Nano Lett. **6**, 2622 (2006).

[97] M. J. A. de Dood, L. H. Slooff, A. Moroz, A. van Blaaderen, and A. Polman, *Local optical density of states in SiO_2 spherical microcavities: Theory and experiment*, Phys. Rev. A **64**, 033807 (2001).

[98] S. Lombardo, S. U. Campisano, G. N. van den Hoven, A. Cacciato, and A. Polman, *Room-temperature luminescence from Er-implanted semi-insulating polycrystalline silicon*, Appl. Phys. Lett. **63**, 1942 (1993).

[99] M. Fujii, M. Yoshida, Y. Kanzawa, S. Hayashi, and K. Yamamoto, *1.54 μm photoluminescence of Er^{3+} doped into SiO_2 films containing Si nanocrystals: Evidence for energy transfer from Si nanocrystals to Er^{3+}*, Appl. Phys. Lett. **71**, 1198 (1997).

[100] G. Franzò, D. Pacifici, V. Vinciguerra, F. Priolo, and F. Iacona, *Er^{3+} ions-Si nanocrystals interactions and their effects on the luminescence properties*, Appl. Phys. Lett. **76**, 2167 (2000).

[101] P. G. Kik and A. Polman, *Gain limiting processes in Er-doped Si nanocrystal waveguides in SiO_2*, J. Appl. Phys. **91**, 534 (2002).

[102] H.-S. Han, S.-Y. Seo, J. H. Shin, and N. Park, *Coefficient determination related to optical gain in erbium-doped silicon-rich oxide waveguide amplifier*, Appl. Phys. Lett. **81**, 3720 (2002).

[103] D. Pacifici, G. Franzò, F. Priolo, F. Iacona, and L. D. Negro, *Modeling and perspectives of Si nanocrystals-Er interaction for optical amplification*, Phys. Rev. B **67**, 245301 (2003).

[104] G. Berden, R. Peeters, and G. Meijer, *Cavity ring-down spectroscopy: Experimental schemes and applications*, Int. Rev. Phys. Chem. **19**, 565 (2000).

[105] I. M. P. Aarts, B. Hoex, A. H. M. Smets, R. Engeln, W. M. M. Kessels, and M. C. M. van de Sanden, *Direct and highly sensitive measurement of defect-related absorption in amorphous silicon thin films by cavity ringdown spectroscopy*, Appl. Phys. Lett. **84**, 3079 (2004).

[106] G. Franzò, S. Boninelli, D. Pacifici, F. Priolo, F. Iacona, and C. Bongiorno, *Sensitizing properties of amorphous Si clusters on the 1.54-μm luminescence of Er in Si-rich SiO_2*, Appl. Phys. Lett. **82**, 3871 (2003).

[107] D. E. McCumber, *Einstein relations connecting broadband emission and absorption spectra*, Phys. Rev. **136**, A954 (1964).

[108] W. J. Miniscalco and R. S. Quimby, *General procedure for the analysis of Er^{3+} cross sections*, Opt. Lett. **16**, 258 (1991).

[109] J. Röhler, in *Handbook on the physics and chemistry of rare earths*, edited by K. A. Gschneider Jr., L. Eyring, and S. Hüfner (North-Holland, Amsterdam, 1987), Vol. **10**, Chapter 71.

[110] J. B. Goedkoop and A. Polman, unpublished.

[111] W. J. Miniscalco, *Erbium-doped glasses for fiber amplifiers at 1500 nm*, J. Lightwave Technol. **9**, 234 (1991).

[112] H. Mertens and A. Polman, *Plasmon-enhanced erbium luminescence*, Appl. Phys. Lett. **89**, 211107 (2006).

[113] J. P. Lakowicz, *Plasmonics in biology and plasmon-controlled fluorescence*, Plasmonics **1**, 5 (2006).

[114] M. Westphalen, U. Kreibig, J. Rostalski, H. Lüth, and D. Meissner, *Metal cluster enhanced organic solar cells*, Sol. Energy Mat. Sol. Cells **61**, 97 (2000).

[115] L. Novotny, *Single molecule fluorescence in inhomogeneous environments*, Appl. Phys. Lett. **69**, 3806 (1996).

[116] V. V. Klimov, M. Ducloy, and V. S. Letokhov, *Spontaneous emission of an atom placed near a prolate nanospheroid*, Eur. Phys. J. D **20**, 133 (2002).

[117] H. T. Dung, L. Knöll, and D. G. Welsch, *Spontaneous decay in the presence of dispersing and absorbing bodies: General theory and application to a spherical nanocavity*, Phys. Rev. A **62**, 053804 (2000).

[118] L. Rogobete and C. Henkel, *Spontaneous emission in a subwavelength environment characterized by boundary integral equations*, Phys. Rev. A **70**, 063815 (2004).

[119] R. Carminati, J.-J. Greffet, C. Henkel, and J. M. Vigoureux, *Radiative and non-radiative decay of a single molecule close to a metallic nanoparticle*, Opt. Commun. **261**, 368 (2006).

[120] Y. S. Kim, P. T. Leung, and T. F. George, *Classical decay rates of molecules in the presence of a spherical surface: a complete treatment*, Surf. Sci **195**, 1 (1988).

[121] C.-T. Tai, *Dyadic Green functions in electromagnetic theory,* 2^{nd} edition, IEEE Press, New York, 1993.

[122] J. Gersten and A. Nitzan, Detailed mathematical appendix of Ref. [19], AIP document no. PAPS JCP SA-75-1139-32, Section B (1981).

[123] L.-W. Li, M.-S. Leong, P.-S. Kooi, and T.-S. Yeo, *Spheroidal vector wave eigenfunction expansion of dyadic Green's functions for a dielectric spheroid*, IEEE Trans. Antennas Propagat. **49**, 645 (2001).

[124] M. Meier and A. Wokaun, *Enhanced fields on large metal particles: dynamic depolarization*, Opt. Lett. **8**, 581 (1983).

[125] P. T. Leung, Y. S. Kim, and T. F. George, *Radiative decay rates for molecules near a dielectric sphere*, J. Phys. Chem. **92**, 6206 (1988).

[126] Y. Xu, R. K. Lee, and A. Yariv, *Quantum analysis and the classical analysis of spontaneous emission in a microcavity*, Phys. Rev. A **61**, 033807 (2000).

[127] D. J. Griffiths, *Introduction to electrodynamics*, Prentice Hall, Upper Saddle River, NJ, 1999.

[128] K. L. Kelly, E. Coronado, L. L. Zhao, and G. C. Schatz, *The optical properties of metal nanoparticles: the influence of size, shape, and dielectric environment*, J. Phys. Chem. B **107**, 668 (2003).

[129] M. I. Stockman, S. V. Faleev, and D. J. Bergman, *Localization versus delocalization of surface plasmons in nanosystems: can one state have both characteristics?*, Phys. Rev. Lett. **87**, 167401 (2001).

[130] K. J. Vahala, *Optical microcavities*, Nature **424**, 839 (2003).

[131] S. A. Maier, *Effective mode volume of nanoscale plasmon cavities*, Opt. quantum electron **38**, 257 (2006).

[132] M. Quinten and U. Kreibig, *Absorption and elastic scattering of light by particle aggregates*, Appl. Opt. **32**, 6173 (1993).

[133] H. T. Dung, L. Knöll, and D. G. Welsch, *Decay of an excited atom near an absorbing microsphere*, Phys. Rev. A **64**, 013804 (2001).

[134] X. M. Hua, J. I. Gersten, and A. Nitzan, *Theory of energy transfer between molecules near solid state particles*, J. Chem. Phys. **83**, 3650 (1985).

[135] E. J. Zeman and G. C. Schatz, in *Dynamics on surfaces: The Jerusalem symposia on quantum chemistry and biochemistry*, edited by B. Pullman, J. Jortner, B. Gerber, and A. Nitzan (Reidel Publishing Co.: Dordrecht, Holland, 1984), Vol. **17**, 413.

[136] L. A. Sweatlock, S. A. Maier, H. A. Atwater, J. J. Penninkhof, and A. Polman, *Highly confined electromagnetic fields in arrays of strongly coupled Ag nanoparticles*, Phys. Rev. B **71**, 235408 (2005).

[137] D. Kovalev, H. Heckler, G. Polisski, and F. Koch, *Optical properties of Si nanocrystals*, Phys. Stat. Sol. B **215**, 871 (1999).

[138] P. F. Liao and A. Wokaun, *Lightning rod effect in surface enhanced Raman scattering*, J. Chem. Phys. **76**, 751 (1981).

[139] E. D. Minot, F. Kelkensberg, M. van Kouwen, J. A. van Dam, L. P. Kouwenhoven, V. Zwiller, M. T. Borgström, O. Wunnicke, M. A. Verheijen, and E. P. A. M. Bakkers, *Single quantum dot nanowire LEDs*, Nano Lett. **7**, 367 (2007).

Summary

Plasmons are collective oscillations of the free electrons in a metal or an ionized gas. Plasmons dominate the optical properties of noble-metal nanoparticles, which enables a variety of applications including electromagnetic energy transport at nanoscale dimensions, single-molecule Raman spectroscopy, and photothermal cancer therapy. Plasmons also affect the spontaneous emission dynamics of optical emitters positioned in the vicinity of metal nanoparticles. The luminescence intensity can either be enhanced or quenched, depending on the geometry. Since the associated enhancements can potentially be several orders of magnitude, plasmon-enhanced luminescence is the subject of intense research.

This thesis focuses on plasmon-enhanced luminescence of silicon quantum dots (Si QDs) and optically active erbium ions. Both these emitters are compatible with silicon processing technology, and are therefore of great technological interest.

In part I we describe three fabrication methods of Ag nanoparticles. First, electron beam lithography is used to fabricate Ag nanoparticles with well-defined sizes and shapes on insulating substrates. This technique is later applied in the experiments on plasmon-enhanced luminescence. Subsequently, we present a method, based on a sequential Si/Ag/Si electron-beam evaporation process, to fabricate metal nanoparticles that exhibit plasmon resonances in the infrared. Furthermore, we discuss the fabrication of small Ag nanoparticles by a sequence of $Na^+ \leftrightarrow Ag^+$ ion exchange and ion irradiation of Na^+-containing glass. In particular, we consistently derive the Ag-nanocrystal depth profile and the corresponding refractive index depth profile by combining multiple characterization techniques.

In part II we show that the photoluminescence intensity of Si QDs can be enhanced in a spectrally selective way by coupling to Ag nanoparticles. The observed luminescence enhancements range between a factor 2 and a factor 6. In addition, we demonstrate that the luminescence enhancement is polarized for elongated Ag nanoparticles. Based on both the spectral selectivity and the polarization selectivity, we conclude that the observed luminescence enhancement is due to coupling of the Si QD emission dipoles to plasmon modes, rather than due to an enhanced excitation rate. As a consequence, the con-

cept of plasmon-enhanced luminescence could also be applied to enhance the luminescence intensity of electrically driven light sources. This possibility is explored by integrating Ag nanoparticles in prototype Si QD light-emitting devices fabricated using processing facilities at Intel Inc. The Si QD electroluminescence intensity of these devices has been enhanced by up to a factor 2.5. Mechanisms that could explain this enhancement are discussed.

By engineering extremely anisotropic Ag nanoparticles, we demonstrate in part III that the photoluminescence intensity of optically active Er^{3+} ions positioned in close proximity to these nanoparticles is significantly enhanced if the nanoparticles support plasmon modes that are resonant with the erbium emission at 1.5 μm. Also for these systems, the enhancement is polarized corresponding to the plasmon resonances of the nanoparticles. These results indicate the opportunities of Ag nanostructures for the reduction of quench processes of erbium in a wide range of materials. Plasmon-enhanced luminescence of erbium may for example enable the realization of efficient light sources based on erbium-doped silicon. In addition, we describe an experiment in which we study the interaction of Er^{3+} ions with Si nanoparticles by cavity ring-down spectroscopy. We demonstrate that the silicon nanoparticles incorporated in Si-rich oxide do not enhance the peak absorption cross section of the Er^{3+} ${}^4I_{15/2} \rightarrow {}^4I_{13/2}$ transition by $1-2$ orders of magnitude, contrary to what has been reported in earlier work. This conclusion has implications for optical amplifier design.

The theoretical investigation of plasmon-enhanced luminescence described in part IV focuses on the modifications of the radiative and nonradiative decay rates of an optical emitter positioned in close proximity to a noble-metal nanoparticle. First we analyze the influence of a spherical nanoparticle by exact electrodynamical theory. We show that the optimal sphere diameter for luminescence quantum efficiency enhancement associated with resonant coupling to plasmon modes is in the range $30-110$ nm, depending on the material properties. The optimal diameter is found to be a trade-off between (1) emitter-plasmon coupling, which is most effective for small spheres, and (2) the outcoupling of plasmons into radiation, which is most efficient for large spheres. In addition, we show that the well-known Gersten and Nitzan model does not describe the existence of a finite optimal diameter unless the model is extended with the correction factor for radiation damping. With this correction and a correction for dynamic depolarization, the Gersten and Nitzan model, which can be generalized to spheroids much more easily than exact electrodynamical theory, is found to provide a reasonably accurate approximation of the decay rate modifications associated with coupling to the dipole plasmon mode.

Based on the improved Gersten and Nitzan model, we subsequently analyze how much the intensity emitted by an active layer of a light-emitting device can be enhanced by an array of anisotropic Ag nanoparticles. For this analysis, the radiative decay rate enhancement associated with emitter-plasmon coupling was calculated for emitters positioned in a plane below a two-dimensional array

of Ag nanoparticles. The in-plane-averaged radiative decay rate enhancement, which is an upper limit of the enhancement of the intensity emitted by the active layer, is found to be a factor ∼10 at a distance of 10 nm from the array for the optimal nanoparticle size of ∼100 nm. The distance at which the nanoparticles induce a substantial effect on the radiative decay rate ranges to a few tens of nanometers. We also show that the radiative decay rate enhancement can be up to three orders of magnitude close to a sharp tip of a metal nanostructure. This results indicates that metal nanostructures can provide even larger improvements to nanoscopic light sources, e.g. based on single nanowires or single quantum dots.

Finally, we study the radiative and nonradiative decay processes for emitters close to anisotropic nanoparticles. We find a larger spectral separation between the radiative dipole plasmon mode and the dark higher-order plasmon modes of a Ag nanoparticle for larger anisotropy. In the vicinity of such an anisotropic Ag nanoparticle, the quantum efficiency of a low-quantum-efficiency emitter (0.1%) can be enhanced by almost a factor 200, instead of a factor 60 for a spherical nanoparticle. These results show that nanoparticle anisotropy does not only influence the plasmon resonance wavelength, but also the ratio at which different plasmon modes are excited by an emitter at short distance.

Altogether, the thesis provides insight in the fundamental aspects of plasmon-enhanced luminescence, and correlates these to experiments on light emitters in practical geometries. Specific insights in possible applications are discussed in the corresponding chapters.

Samenvatting

Plasmonen zijn collectieve oscillaties van de vrije elektronen in een metaal of een geïoniseerd gas. In metalen nanodeeltjes zijn deze excitaties resonant in het zichtbare en infrarode deel van het elektromagnetisch spectrum. Het opwekken van een plasmon in een metalen nanodeeltje door een inkomende lichtgolf heeft tot gevolg dat de elektromagnetische energie in een zeer klein volume wordt geconcentreerd; het nanodeeltje zuigt het licht als het ware naar zich toe. Deze concentratie van licht biedt perspectieven voor een groot aantal toepassingen waaronder het transporteren van elektromagnetische energie in ultrakleine circuits en het vergroten van de gevoeligheid van optische meettechnieken zoals bijvoorbeeld Raman spectroscopie. Daarnaast kan de spontane emissie van elementaire lichtbronnen (zoals atomen en moleculen, maar ook nanodeeltjes die bestaan uit halfgeleidermateriaal) sterk beïnvloed worden door metalen nanodeeltjes. Afhankelijk van de geometrie kan de luminescentie-intensiteit worden verhoogd of verlaagd. De manipulatie van spontane emissie met behulp van metalen nanodeeltjes staat de laatste jaren in grote belangstelling omdat de luminescentie-intensiteit van lichtbronnen in bepaalde gevallen met factoren 100 tot 1000 kan worden vergroot.

Dit proefschrift richt zich op het vergroten van de luminescentie-intensiteit van silicium nanodeeltjes en erbium ionen door deze lichtbronnen te koppelen met plasmonen in zilveren nanodeeltjes. Zowel silicium nanodeeltjes als erbium ionen zijn technologisch relevant omdat ze beide verenigbaar zijn met de fabricagemethodes uit de elektronica-industrie.

In deel I van het proefschrift beschrijven we drie methodes om zilveren nanodeeltjes te fabriceren. We gebruiken elektronenbundel-lithografie om zilveren nanodeeltjes met welbepaalde groottes en vormen te maken. Deze fabricagemethode wordt later toegepast in de experimenten die betrekking hebben op het verhogen van de luminescentie-intensiteit van elementaire lichtbronnen. Vervolgens wordt een methode behandeld waarin achtereenvolgens silicium, zilver en silicium worden opgedampt om zilveren nanodeeltjes te fabriceren die plasmonresonanties vertonen in het infrarode deel van het elektromagnetisch spectrum. Verder beschrijven we de fabricage van zilveren nanodeeltjes met behulp van een proces bestaande uit $Na^+ \leftrightarrow Ag^+$ ionenuitwisseling en Xe ionenbestraling van Na^+-houdend glas. We richten ons hierbij op de bepaling

van het diepteprofiel van de laag waarin zilveren nanodeeltjes worden gevormd en van het diepteprofiel van de effectieve brekingsindex.

In deel II laten we zien dat de intensiteit waarmee silicium nanodeeltjes luminesceren kan worden verhoogd door deze lichtbronnen in de nabijheid van zilveren nanodeeltjes te plaatsen. De gemeten verhogingen, die een spectrale signatuur hebben die afhangt van de geometrie van de zilveren nanodeeltjes, variëren tussen een factor 2 en een factor 6. Daarnaast is deze intensiteitsverhoging gepolariseerd voor uitgerekte zilveren nanodeeltjes. Op basis van deze spectrale en polarisatie-afhankelijke kenmerken concluderen we dat de waargenomen intensiteitsverhoging het gevolg is van koppeling van de *emissie-dipolen* van de silicium nanodeeltjes met plasmon-excitaties, en dat de verhoging niet een gevolg is van een toegenomen optische excitatie-snelheid. Dit betekent dat het concept van het verhogen van de luminescentie-intensiteit door middel van plasmonen ook kan worden toegepast in lichtbronnen die elektrisch worden aangedreven. Deze mogelijkheid onderzoeken we door zilveren nanodeeltjes te integreren in een lichtgevend apparaat waarin de actieve laag gevormd wordt door silicium nanodeeltjes. De luminescentie-intensiteit onder elektrische excitatie is verhoogd met een factor 2.5. De mechanismen die deze verhoging kunnen verklaren worden besproken.

Door zeer uitgerekte zilveren nanodeeltjes toe te passen tonen we in deel III van het proefschrift aan dat de luminescentie-intensiteit van erbium ionen significant kan worden verhoogd als de plasmon-excitaties van die nanodeeltjes resonant zijn met de erbium-emissie met een golflengte van 1.5 μm. Ook voor dit systeem is de luminescentie gepolariseerd overeenkomstig met de polarisatie van de plasmonresonanties van de nanodeeltjes. Deze metingen wijzen erop dat zilveren nanodeeltjes de mogelijkheid bieden om de invloed van verliesprocessen op de luminescentie van erbium te reduceren. Dit concept kan bijvoorbeeld leiden tot efficiënte lichtbronnen op basis van erbium-gedoteerd silicium. Naast de resultaten omtrent erbium in de nabijheid van zilveren nanodeeltjes, beschrijven we in deel III van het proefschrift ook een experiment waarin we de interactie tussen erbium ionen en silicium nanodeeltjes onderzoeken. We tonen aan dat silicium nanodeeltjes in silicium-rijk siliciumoxide de piek absorptie cross sectie van de Er^{3+} $^4I_{15/2} \rightarrow {}^4I_{13/2}$ transitie niet met 1 tot 2 ordes van grootte verhogen, in tegenstelling tot wat in de literatuur wordt beweerd. Dit resultaat is relevant voor het ontwerp van optische versterkers op basis van erbium.

De theoretische bestudering van de veranderingen van luminescentie-intensiteit als gevolg van koppeling van lichtbronnen met plasmonen wordt behandeld in deel IV van het proefschrift. Eerst analyseren we de veranderingen van de snelheden van stralend en niet-stralend verval van een elementaire lichtbron die in de nabijheid van een bolvormig nanodeeltje is geplaatst. Deze analyse wordt uitgevoerd met behulp van een exacte elektrodynamische theorie. We tonen aan dat de optimale boldiameter voor het verhogen van het quantumrendement in het bereik $30 - 110$ nm ligt. Deze optimale diameter

wordt bepaald door een evenwicht tussen (1) de koppeling tussen lichtbron en plasmon-excitatie, die het meest effectief is voor kleine bollen, en (2) de uitkoppeling van plasmonen naar straling, die het meest efficiënt is voor grote bollen. In aanvulling hierop tonen we aan dat het welbekende model van Gersten en Nitzan het bestaan van een eindige optimale diameter niet beschrijft, tenzij het model wordt uitgebreid met een correctie voor stralingsdemping. Met deze correctie en een correctie die retardatie van het depolarisatieveld beschrijft, geeft het Gersten en Nitzan model, dat eenvoudiger kan worden gegeneraliseerd naar anisotrope deeltjes dan de exacte theorie, een adequate beschrijving van de veranderingen van de vervalsnelheden voor de relevante deeltjesgroottes.

Op basis van het verbeterde Gersten en Nitzan model analyseren we vervolgens hoe sterk de intensiteit die uitgestraald wordt door een 2-dimensionale actieve laag kan worden versterkt met behulp van een raster van anisotrope deeltjes. Voor deze analyse is de vergroting van de snelheid van stralend verval berekend in een vlak onder dit raster. Het gemiddelde over het hele vlak is een factor $\sim$10 op een afstand van 10 nm van de nanodeeltjes voor een optimale deeltjesgrootte van $\sim$100 nm. Deze factor $\sim$10 is een bovenlimiet voor de verhoging van de uitgestraalde intensiteit. De afstand tot waar de nanodeeltjes een substantieel effect op de vervalsnelheid hebben is enkele tientallen nanometers. Dichtbij een scherpe rand van een metalen nanostructuur kan de vergroting van de snelheid van stralend verval drie ordes van grootte bedragen. Dit betekent dat metalen nanostructuren veelbelovend zijn voor lichtbronnen met zeer kleine afmetingen, bijvoorbeeld lichtbronnen die gebaseerd zijn op enkele nanodraden.

Tenslotte bestuderen we het stralende en niet-stralende verval van lichtbronnen die in de nabijheid van anisotrope nanodeeltjes zijn gepositioneerd. We laten zien dat de spectrale separatie tussen de stralende dipool plasmon-excitatie en de niet-stralende hogere-orde plasmon-excitaties van een zilver nanodeeltje toeneemt voor grotere anisotropie. In de nabijheid van een anisotroop zilveren nanodeeltje kan het quantumrendement van een lichtbron die in de afwezigheid van het metaal een laag quantumrendement heeft (0.1 %), met een factor 200 worden vergroot, in plaats van met een factor 60 voor een bolvormig deeltje. Dit resultaat toont aan dat de deeltjesvorm niet alleen de frequentie van de plasmonresonantie beïnvloedt, maar ook de verhouding waarmee verschillende plasmon-excitaties aangeslagen worden door een lichtbron op korte afstand.

Samenvattend geeft dit proefschrift inzicht in fundamentele aspecten van het manipuleren van de emissie-eigenschappen van elementaire lichtbronnen die gekoppeld zijn aan plasmonen in metalen nanodeeltjes. Specifieke inzichten met betrekking tot mogelijke toepassingen worden besproken in de overeenkomstige hoofdstukken.

Dankwoord

Voor u ligt een proefschrift dat tot stand is gekomen met de steun en hulp van een groot aantal mensen. In de eerste plaats wil ik mijn promotor Albert Polman bedanken voor de enthousiaste begeleiding, de snelle reacties op mijn manuscripten en de vele mogelijkheden die ik kreeg om mijn werk op internationale conferenties te presenteren. Deze aspecten hebben stimulerend gewerkt bij de totstandkoming van dit proefschrift. In aanvulling hierop wil ik Kobus Kuipers bedanken voor de vele adviezen die hij me gegeven heeft, met name in het jaar dat Albert als gastonderzoeker werkzaam was op Caltech.

Jeroen Kalkman ben ik erkentelijk voor de leerzame introducties in de meetopstellingen die in onze onderzoeksgroep beschikbaar waren. Deze hulp bood mij de mogelijkheid om in korte tijd meerdere experimenten van de grond te krijgen. Daarnaast waren er de vele discussies die we in onze werkkamer hadden, vaak samen met Jan van der Elsken die gelukkig nooit te beroerd was om zijn kritische licht te laten schijnen. Later werden Ewold Verhagen, Martin Kuttge en Ernst Jan Vesseur aangename kamergenoten met wie ik altijd prettig heb samengewerkt en veel heb kunnen discussiëren. Bedankt daarvoor. Teun van Dillen wil ik bedanken voor de hulp bij de ionenimplantaties (Hoofdstuk 4) die ik in mijn eerste maand op AMOLF snel moest uitvoeren omdat de ionenversneller kort daarna werd ontmanteld. De technische ondersteuning van Johan Derks was ook erg belangrijk voor dit experiment. Femius Koenderink bedank ik voor de essentiële rol die hij gespeeld heeft bij het opzetten van de berekeningen die beschreven zijn in Hoofdstuk 10. Verder wil ik alle overige groepsleden, te weten Joan Penninkhof, Anna Tchebotareva, Max Siem, René de Waele, Timon van Wijngaarden, Martien den Hartog, Rob van Loon en Sébastien Bidault, bedanken voor de dagelijkse discussies en de bijdrages aan de wekelijkse werkbesprekingen. Ook de mensen uit de andere onderzoeksgroepen van de afdeling Nanofotonica ben ik erkentelijk voor de goede contacten en de leerzame gemeenschappelijke colloquia.

Een groot deel van mijn onderzoek (Hoofdstukken 2, $5-8$) heb ik kunnen verrichten dankzij de fabricagefaciliteiten in het nanoCenter. De brede kennis en de behulpzaamheid van nanofabricage-specialist Chris Rétif waren in dit opzicht essentieel. Jan Verhoeven dank ik voor de hulp bij het gebruik van de opdampers in zijn lab (Hoofdstuk 3). Jan's onorthodoxe manier van experi-

menteren was vaak een aangename belevenis. Frans Tichelaar wil ik bedanken voor de metingen met de transmissie elektronen microscoop, en Marc Kessels voor de hulp bij de samplepreparatie voor deze metingen. Ook de technische ondersteuning van Hans Zeijlemaker bij de opdampers mag niet onvermeld blijven. Voorts ben ik Jord Prangsma erkentelijk voor de ondersteuning bij het gebruik van de meetapparatuur in de Nano-optica groep.

I'm grateful to Julie Biteen and Harry Atwater for their contribution to the experiments on plasmon-enhanced luminescence of silicon quantum dots. Our intense collaboration has resulted in a successful project (Chapter $5-7$). Also I would like to acknowledge Robb Walters and Dominico Pacifici for their help in setting up the electroluminescence measurements on the FELED devices during my stay at Caltech (Chapter 7).

Igor Aarts, Erwin Kessels en Richard van de Sanden wil ik bedanken voor de samenwerking bij het meten van de absorptie cross-sectie van erbium (Hoofdstuk 9). Dit uitdagende experiment is uiteindelijk gelukt, grotendeels dankzij de uitgebreide expertise op het gebied van cavity ring down spectroscopie aan de TU Eindhoven. Verder wil ik Denise Krol bedanken voor de aangename samenwerking tijdens haar bezoek aan AMOLF, en Arjen Vredenberg en Wim Arnold Bik voor hun hulp bij het gebruik van de ionenversneller aan de Universiteit Utrecht.

Tenslotte hebben de goede sfeer binnen AMOLF en de korte lijnen met de ondersteunende afdelingen sterk bijgedragen aan het vlotte verloop van mijn onderzoek. In dit opzicht wil ik Roudy van der Wijk in het bijzonder bedanken voor de ondersteuning op het gebied van de Amsterdamse woningmarkt. Voor de broodnodige ontspanning is het AMOLF/NIKHEF zaalvoetbalteam erg belangrijk geweest. Ik wil alle spelers, en in het bijzonder drijvende kracht Fred Bulten, bedanken voor de sportieve sfeer. Als laatste wil ik mijn familie, kennissen en vrienden bedanken voor de interesse die ze getoond hebben. Jullie medeleven was een grote steun bij het tot stand komen van dit proefschrift.

Curriculum vitae

Hans Mertens was born in Weert, The Netherlands, on January 25, 1978. He received a VWO degree (pre-university education) at the Philips van Horne scholengemeenschap in Weert in 1996. From 1996 he studied Applied Physics at the Eindhoven University of Technology. In 2001 he performed an internship at the Danish site of the telecom company ADC, where he worked on plasma-enhanced chemical vapor deposition of silicon oxynitride. The study Applied Physics was completed with an experimental research project at the Research Center COM at the Technical University of Denmark (DTU) in Kopenhagen. This work, which was carried out under supervision of Prof. Dr. W. E. Svendsen and Prof. Dr. H. W. M. Salemink, was focused on the development of optical waveguide structures based on silicon rich nitride. In 2002 he received his 'doctoraal' degree in Applied Physics. During his study, Hans was a member of the interdisciplanary team of the TUE that developed an autonomous robot system for the international competition Eurobot, held in La Ferté-Bernard, France, in 2000.

In 2002 Hans started as a Ph.D. student in the Photonic Materials group at the FOM Institute for Atomic and Molecular Physics (AMOLF), under supervision of Prof. Dr. A. Polman. The research performed within the context of this Ph.D. project is the subject of this thesis. Part of the work was done in close collaboration with the group of Prof. H. A. Atwater at the California Institute of Technology in Pasadena, CA.

List of publications

This thesis is based on the following publications:

- *Infrared surface plasmons in two-dimensional silver nanoparticle arrays in silicon*, H. Mertens, J. Verhoeven, A. Polman, and F.D. Tichelaar, Appl. Phys. Lett. **85**, 1317 (2004). (Chapter 3)
- *Depth-resolved nanostructure and refractive index of borosilicate glass doped with Ag nanocrystals*, H. Mertens and A. Polman, Opt. Mat. **29**, 326 (2006). (Chapter 4)
- *Spectral tuning of plasmon-enhanced silicon quantum dot luminescence*, J. S. Biteen, N. S. Lewis, H. A. Atwater, H. Mertens, and A. Polman, Appl. Phys. Lett. **88**, 131109 (2006). (Chapter 5)
- *Polarization-selective plasmon-enhanced silicon quantum dot luminescence*, H. Mertens, J. S. Biteen, H. A. Atwater, and A. Polman, Nano Lett. **6**, 2622 (2006). (Chapter 6)
- *Plasmon-enhanced erbium luminescence*, H. Mertens and A. Polman, Appl. Phys. Lett. **89**, 211107 (2006). (Chapter 8)
- *Absence of the enhanced intra-4f transition cross section at 1.5 μm of Er^{3+} in Si-rich SiO_2*, H. Mertens, A. Polman, I. M. P. Aarts, W. M. M. Kessels, and M. C. M van de Sanden, Appl. Phys. Lett. **86**, 241109 (2005). (Chapter 9)
- *Plasmon-enhanced luminescence near noble-metal nanospheres: comparison of exact theory and an improved Gersten and Nitzan model*, H. Mertens, A. F. Koenderink, and A. Polman, submitted. (Chapter 10)
- *Radiative decay rate enhancements in the vicinity of two-dimensional arrays of anisotropic metal nanoparticles*, H. Mertens, J. S. Biteen, H. A. Atwater, and A. Polman, to be submitted. (Chapter 11)
- *Spectral separation of radiative and dark plasmon modes in anisotropic metal nanoparticles*, H. Mertens and A. Polman, to be submitted. (Chapter 12)

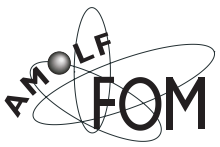

The work described in this thesis was performed at the FOM-Institute for Atomic and Molecular Physics, Kruislaan 407, 1098 SJ Amsterdam, in collaboration with Utrecht University and Eindhoven University of Technology, all in the Netherlands, and in collaboration with California Institute of Technology, Pasadena, CA.

Affiliation:

Prof. Dr. A. Polman
Center for Nanophotonics
FOM-institute AMOLF, Amsterdam, The Netherlands